Luminophores and CarbonNanostructures: Towards New Functional Materials

John Mohanraj

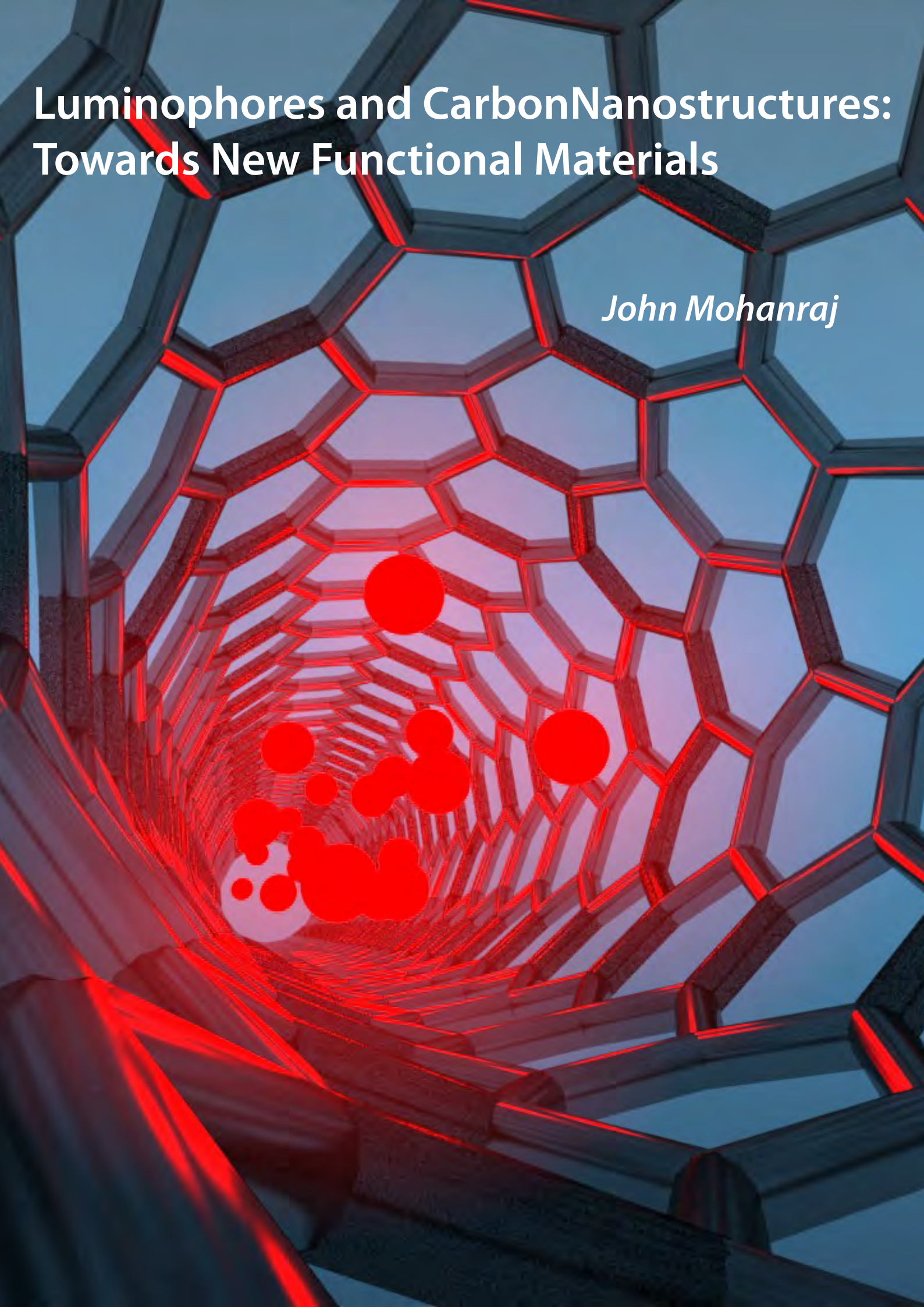

Alma Mater Studiorum – Università di Bologna

DOTTORATO DI RICERCA IN

Scienze Chimiche

Ciclo XXIV

Settore Concorsuale di afferenza: Fondementi Delle Scienze Chimiche E Sistemi Inorganici

Settore Scientifico disciplinare: Chimica Generale Ed Inorganica

Luminophores and Carbon nanostructures: towards new functional materials

Presentata da: John Mohanraj John Kannan

Coordinatore Dottorato

Prof. Adriana Bigi

Relatore

Dr. Paola Ceroni

Correlatore

Dr. Nicola Armaroli

Esame finale anno 2012

Acknowledgements

I would like to thank Dr. *Nicola Armaroli* for his guidance and support during the course of my doctoral work. Undoubtedly, the whole credit for making me as a *Photochemist* goes to him and I will remain grateful for the opportunity he offered me to join his research group. I would like to thank Dr. *Gianluca Accorsi*, who trained me to work with many instruments and most of the reported measurements would have not possible without him. I also thank *Dr. Yoosaf Karuvath* for his short and rapid courses on fundamental photochemistry. Also I thank my past and present colleagues Dr. *Abdul Halim Belbakra*, *Filippo Monti*, *Joanna Malicka* and *Dr. Praveen*, who have been helping me in many ways.

This work could have not been possible without the materials from group of Dr. *Davide Bonifazi*. Especially I would like to thank Dr. *Anna Llanes-Palas*, Dr. *Claudia Aurisicchio*, *Laura Maggini*, *Hassan Traboulsi*, *Tomas Marangoni* and *Riccardo Marega* for their constant support.

I would also like to thank Dr. *Jean-Francois Nierengarten* and his group members Dr. *Michel Holler*, Dr. *Juan-jo Cid*, Dr. *Maida Vartanian* and *Meera Mohankumar*, who prepared and provided some interesting compounds.

Thanks as well to Dr. *Marek Pietraszkiewicz* and Dr. *Oksana Pietraszkiewicz* and their group members for their materials contribution for my work.

I thank all the people from *Nanocyl* for providing carbon nanotubes without hesitation.

Special thanks to *Roberto Lazzaroni, Andrea Minoia, Jacques Dumont, Thomas Seldrum, Valentina Corvaglia, Romain Delamare, Dana Alina Serban-Vlad, Cristian Kusko, Constantin Augustin Dutu, Gaëlle Deshayes, Olivier Coulembier, Sorin Melinte*, and *Béatrice Delavaux-Nicot and her group members,* who have contributed significantly to improve our results.

My many thanks due to *Pier Luigi* for his efforts to make the cover page.

I would like to thank all the members of ISOF family, especially, Dr. *Lucia Flamigni*, Dr. *Sandra Monti*, Dr. *Andrea Barbieri*, Dr. *Barbara Ventura*, Dr. *Francesco Manoli* for answering my questions all the time with a smile. Also I thank Dr. *Raffaella Amodio*, *Roberta Chiodini*, *Illaria Giuliodori* for their great assistance in managing official things.

I thank all my teachers, who have transferred their valuable knowledge to enlighten my mind.

I would like to specially thank *Resmi* and *Anand Kumar*, who have been helping me a lot in enormous amounts of day-to-day matters. Also I thank my friends at back-home, whose words made me strong, and provided confidence to pursue my research work.

Finally, without my beloved Mom and sister, my research would have not gone smoothly. I always owe to their love, prayers and sacrifices, which have brought me up to this level.

John Mohanraj

To my beloved dad

TABLE OF CONTENTS

6. EXPERIMENTAL SECTION

Abstract

"My father rode a camel. I drive a car. My son flies a jet-plane. His son will ride a camel"

This famous Saudi Arabian saying not only reminds us how fossil fuels have powered human civilization, but also alarms about the depleting energy resources in the current scenario. For many reasons the present world is facing a deep energy crisis and hence it urges to look for alternative sources to retain its momentum. Although the invention of nuclear energy brought hopes in the early stage, its huge investment cost, hazardous radiation, environmental contamination and exhaustive use of natural resources impel to find cleaner and cheaper power sources. While the use of renewable energies (primarily solar energy) has started to spread around the world, considerable interest has been turned also to reduce energy consumption. However, conventional devices in day-to-day practice are often not yet optimized for this purpose. In line with this, an intense research is pursued around the globe to develop next-generation devices with new functional materials, which can perform better than conventional ones, while consuming much less energy.

Nanostructures, due to their exceptional physical, chemical and mechanical properties, play a pivotal role in preparing next-generation materials. In particular, carbon nanomaterials (fullerenes, carbon nanotubes, graphene etc.), which show high thermal and electrical conductivity, aspect ratio, shear strength and chemical/mechanical resistance, are quite promising for a wide range of applications. Accordingly, gaining ability to control and tune their intrinsic properties would considerably expand their applicative perspectives in many technological fields.

My doctoral work is mainly focused on (i) the preparation of luminescent functional materials based on carbon nanostructures, by combining strongly emissive luminophores with carbon scaffolds through covalent and non-covalent functionalization and (ii) their extensive structural and optical characterization. Essentially, our goal has been to understand the nature of interaction between carbon nanotubes and luminophores and to produce strongly emissive hybrids entailing the peculiar physical properties of carbon materials.

In Chapter 1, the properties of carbon nanotubes (CNTs), which are the materials of our highest interest, are briefly overviewed. Following this, a few recent examples illustrating the different strategies of preparation and characterization of CNT-luminophore hybrid materials are reported, also discussing their optical properties.

The first part of the present doctoral work is presented in Chapter 2, where the photophysical properties of a library of lanthanide(III) complexes in solution and solid media are presented. In the second part, emission features of a set of transition metal complexes, in

particular copper(I) complexes, are described. This library of luminophores has allowed sorting out the most suitable compounds to combine with carbon nanostructures.

In the first part of Chapter 3, the problem of limited solubility of CNTs that hampers their industrial utilization is addressed through a supramolecular approach. Taking advantage on H-bond assisted polymeric structures forming π-conjugated organic scaffolds, peripherally equipped with 2,6-(diacetoamino) pyridine and uracil units, a new strategy was developed to reversibly solubilize CNTs, especially MWNTs. Further modifications of the same methodology with chiral binaphthols containing uracil terminal units allowed to prepare chiral helical fibers, which are suitable candidates to separate and selectively solubilze chiral CNTs from the bulk mixture. The synthesis of monomeric units and the experimental proofs to confirm the chirality and supramolecular structure of the prepared fibers in solution and on a metal surface are illustrated in the second part.

The ultimate goal of this doctoral work, i.e. the preparation and characterization of novel luminescent CNT hybrids, is reported in Chapter 4. The first part of this section is dedicated to a host-guest complex prepared with a europium(III) complex and multiwalled CNTs, where the challenging procedure of encapsulation and the characterization of the produced material by means of optical microscopy and photophysics are described in detail. Alternatively, exohedral functionalization of CNTs surface also provided a simple route to prepare a highly emissive composite material. The anionic europium(III) complexes are anchored non-covalently on CNTs surface, mediated by a cationic layer of ionic liquid. In this way, the direct interaction of CNTs with luminophore was avoided and thus, it showed significantly high photoluminescence quantum yield as similar to the pristine Eu(III) complex. The preparation and characterization of this material is presented in the second part of this chapter.

Finally, in Chapter 5, photoactive materials based on porphyrin electron donors and CNTs or fullerene electron acceptors, synthesized with the aim of improving the efficiency of organic photovoltaic devices, are reported. The first part of this chapter is about a set of hybrids with porphyrins and double-walled CNTs, prepared through covalent and non covalent synthetic methods. Further, morphological, theoretical and photophysical studies carried out on these hybrids show the advantage of having strong π-conjugated porphyrin units on top of CNTs, which eventually assist CNTs to arrange in an optimized way inside a prototype PV cell. The PV measurements showed high conductivity properties compared to devices where only pristine CNTs are incorporated. The second part focuses on the synthesis and characterization of a porphyrin-C_{60} triad, which showed charge transfer character upon photoexcitation in polar solvents. In toluene medium, an efficient energy transfer from porphyrin to C_{60} was evidenced

while exciting the porphyrin selectively. All the photoinduced processes observed in this hybrid are reported in detail.

All the materials based on carbon nanostructures described in this thesis are innovative examples of photoactive and luminescent hybrids, and their morphological and photophysical properties help understanding the nature of interactions between the active units. This may prompt the design and fabrication of new functional materials for applications in the fields of optoelectronics and photovoltaics.

Chapter 1

Introduction

Since conventional fossil fuel reserves are progressively depleted, the growing global demand of energy calls for alternative renewable energy sources and technologies.[1] At the same time, consuming less energy and conserving existing resources has become essential, particularly in non-affluent countries. Throughout the world, a considerable effort has been undertaken in this direction, for instance in the development of devices requiring smaller energy inputs and producing more efficient outputs. In this context, it has become imperative to look for novel materials to be exploited in a variety of energy related applications such as solar energy conversion, hydrogen production and storage, batteries, fuel cells, thermal insulation, etc.[2-4] In the last decades, nanomaterials, i.e. materials whose one or more dimensions are within the range of 1-100 nanometer (nm)[5], have been gaining momentum since they can exhibit much better features compared to "classic" macromolecules. Among them, carbon nanotubes (CNTs), due to their peculiar physical and chemical properties such as high aspect ratio, thermal and electrical conductivity, physical robustness, chemical inertness, cell permeability etc., have attracted much attention from researchers around the world.[4,6] These extraordinary properties combined in the same platform can make CNTs key materials for the technologies of the 21st century[7] and their increased demand in different fields may trigger mass scale production, while research are thriving to solve some of their problems such as solubilization[8-11] and separation,[4,12-15] to take advantage of their electronic properties. Preparation of CNTs composites by functionalization with organic and inorganic molecules can finely tune the intrinsic properties of both units, affording functional materials with distinct characteristics. This can extend the horizon of CNTs applications in many fields. For instance, CNT functional materials showing high conductivity, low work function and amphoteric electronic nature can play pivotal roles in the field of optoelectronics.[3,16] On the other hand, luminescent hybrids have been prepared by attaching luminophores to CNTs either through covalent or by non-covalent bonds, and both methods show advantages as well as disadvantages. Functionalizing CNTs by covalently attaching organic/inorganic moieties ensures stable and permanent bonding; however, the severe and irreversible damages to the CNTs outer walls are inevitable, and strongly alter their electronic

properties.[6,7] Non-covalent decoration of CNTs leads to weaker bonding between external moieties and the tubes, but it does not affect the intrinsic properties of the carbon scaffold. Hence, many hybrids have been developed based on intermolecular π-π interactions and other van der Waals forces.

1.1 Carbon nanotubes and their electronic energy levels

CNTs are cylindrically rolled up graphene sheets characterized by chiral indices (n,m), which uniquely define their physical and chemical properties.[17] Based on the number of walls, the CNTs are divided into single- (SWCNTs) and multi- (MWCNTs) walled carbon nanotubes. Further classification of SWCNTs is due to their metallic or semiconductive nature, dictated by (n,m) values; for a CNT, if the resulting number is a multiple of 3, then it is a metallic tube, else it is semiconductive.[3,4,18] Therefore, one third of SWCNTs are naturally metallic and the remainders are semiconducting. It should be emphasized that, as prepared, SWCNTs always exist as a blend of metallic and semiconducting tubes and their separation is a difficult but crucially important issue. Mechanical separation processes are strongly limited by the spontaneous bundling of SWCNTs, which results from smooth surface and intertube van der Waals interactions.[7] Both goals, debundling and separation of semiconductive from metallic tubes, have been achieved at the laboratory scale, but still an intense research is dedicated to implement protocols for industrial upscaling.[4,12,15] MWCNTs are constructed with many single concentric walls, arranged in a co-axial fashion. However, the properties are not simply the sum of component single walled tubes. The closely arranged electronic levels of every single tube make MWCNTs metallic.[3,4,18] MWCNTs exhibit lower bundling affinity, lower production cost and easier processing compared to SWCNTs, and this can make them more advantageous for bulk production and material fabrication. Adequate knowledge on electronic energy levels is essential for both types of nanotubes in any sort of envisaged applications. The one dimensional nature of CNTs leads to discontinuity in the density of electronic states (Van Hove singularities) and the electronic absorption spectrum of as prepared SWCNTs shows 2 major sharp peaks at 1800 nm (0.68 eV) and 1000 nm (1.2 eV) corresponding to transitions $\upsilon^1_s \rightarrow c^1_s$ and $\upsilon^2_s \rightarrow c^2_s$, where υ_s and c_s denote valence and conduction bands of semiconducting tubes; metallic SWCNTs absorb strongly at 700 nm (1.8 eV) due to $\upsilon^1_m \rightarrow c^1_m$ transition.[19,20] Interestingly, the CNTs band gap is inversely proportional to the diameter; this allows controlling the electronic properties of the nanotubes, especially SWCNTs, to fit into specific requirements for optoelectronic devices. The photoexcitation of semiconducting SWCNTs leads to extremely weak near infrared emission,

related to the small bandgap between conduction and valence electronic levels;[21,22] this faint luminescence is further quenched by the presence of metallic tubes in the bulk or by the inter-tube energy transfer within the bundles.[23] The metallic MWCNTs have measureable density of states at the Fermi level, like graphite, with small band gap; hence, the optical transitions yield a broad, featureless band spreading from the infrared to the UV spectral region. Notably, due to the low-lying conduction bands of SWCNTs and MWCNTs, electro- or photoexcitation of organic/inorganic units in functionalized CNT hybrids typically leads to efficient energy and electron transfer processes.[24-27] Thus, choosing the appropriate molecules to append to CNTs and avoid such processes is extremely challenging. Some examples on photoinduced processes in CNT hybrids are discussed herein.

1.2 Exohedrally functionalized CNTs

A huge variety of organic molecules and inorganic phosphors/complexes have been non-covalently attached to CNTs by means of π-π stacking or other weak forces.[4,6,7,18] The non-covalent method allows to preserve the unique features of CNTs and, in addition, the surface covering of nanotubes with organic moieties helps dispersing the CNT bundles in conventional organic solvents. This opens the way to purify, separate and process the pristine black material.[7,11] Organic molecules with highly π-conjugated aromatic backbones and large active surface area, efficiently self-assemble on CNTs.[11] For example, porphyrin and pyrene chromophores have been exploited by Guldi and Prato et al.,[24,28-30] and others[31,32] to supramolecularly functionalize the graphitic walls of CNTs. The preparation strategy consists of sheer stirring of CNTs and the chosen adhering molecule in an organic solvent, followed by sonication and centrifugation. The filtered, dried and re-dispersed CNT-porphyrin/polymer hybrid solutions display interesting photophysical features, such as red-shifted porphyrin absorption features, reduced fluorescence intensity and short-lived excited states, compared to the reference porphyrins (**Figure 1.2.1**). The rationalization of luminescence quenching was obtained by time resolved absorption and emission measurements. The observed results suggest that photoexcitation of a **SWCNT-porphyrin/polymer** mixture in deoxygenated DMF solution results in the formation of a charge separated state, in which the porphyrin radical cation and the SWCNTs anion live for 2.1 microseconds (μs). The **MWCNT-Zn porphyrin^{8-}** analogue with pyrene shows a similar process with a longer-lived charge separated state (5.8 μs).[24] A **Rhodamine B-SWCNT** analogue was also prepared, in which the emission intensity of the dye decreases by addition of increasing amounts of SWCNT.[33] A detailed photophysical analysis

evidences static quenching attributed to photoinduced electron transfer between SWCNT and surface immobilized dye. Another supramolecular complex, A **Riboflavin-MWCNT** adduct was prepared by grinding the two subunits with a few drops of water, followed by thorough washing and centrifugation.[27] The filtered, dried black material is dispersed in water. It's worth mentioning that this composite shows excellent dispersion in water, due to the appended hydrophilic riboflavin moieties, and stays dispersed for a long time. The photoirradiation of Riboflavin-MWCNT induces excited state electronic processes and ultrafast measurements show signals corresponding to riboflavin cation and MWCNTs anion, with decay time of 3 μs. However, though long-lived charge separated states are excellent features for the development of artificial photosynthetic devices, the combination of organic luminophores and CNTs mostly leads to luminescence quenching. Therefore these composite are often not suitable for device applications requiring light emission.

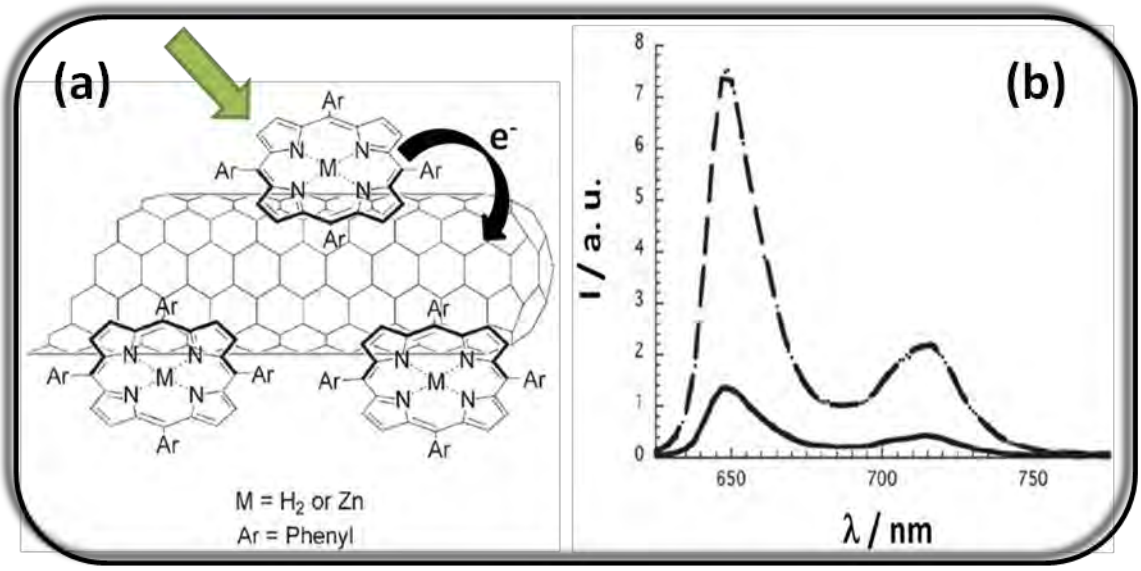

Figure 1.2.1 *(a) Schematic representation of charge transfer interaction between porphyrin and SWCNTs. (b) Fluorescence emission spectra of porphyrin (dashed line) and SWCNT-porphyrin (solid line) in DMF, upon exciting at 418 nm. (Adapted from ref. 28)*

Quantum dots (QDs) decorated CNTs also exhibit the same behaviour as above. However, unlike organic chromophores, the controllable interchromophoric distance allows to control the undesired excited state processes. For instance, a **CdSe QDs-SWCNTs** composite has been prepared by non-covalently attaching pyridine capped QDs on the surface of CNT.[34] The analyses performed using atomic force microscopy (AFM) and transmission electron microscopy (TEM) show the dense, uniform packing of QDs on the graphitic surface as a result of strong π-π interactions between pyridine and CNT units. Upon irradiation, electron transfer is observed from

the excited QDs to SWCNT's, and this is probably facilitated by shorter interchromophoric distance. This hypothesis is supported by the similar **CdSe-ZnS QDs-SWCNTs** hybrid, cross-linked (ca. 10 nm) by biotin-streptavidin, in which Förster resonance energy transfer (FRET) is observed from QDs to CNTs, upon irradiation.[35] Thus, electron transfer is switched to energy transfer in similar systems by changing the interchromophoric distance.

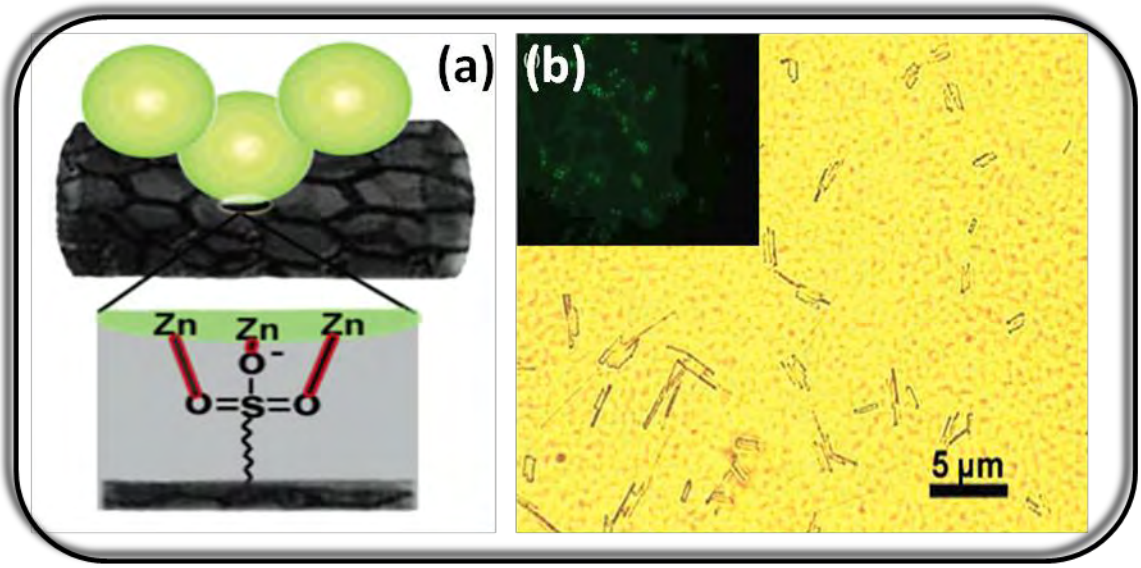

Figure 1.2.2 *Schematic illustration of the coordination between CdSe-Zn QDs and SDS units adsorbed on SWCNTs. (b) Fluorescence (inset) and transmitted brightfield images of individual SWCNTs and their ropes. (Adapted from ref. 35)*

Notably, the QDs luminescence properties of biotin-streptavidin cross linked **CdSe-ZnS QDs-SWCNTs** are little affected (ca. 30% quenching); this is attributed to the weak dipole coupling between the active units, resulting from the long interchromophoric distance (≤ 10 nm). Surprisingly, the same combination prepared with a different method shows a bright green emission corresponding to the QDs, and helps to visualize the individual small bundles of SWCNTs with fluorescence microscopy techniques.[36] To prepare the hybrid, first the SWCNTs are dispersed in aqueous solution using sodium dodecylsulphate (SDS) surfactant. Due to the strong affinity of alkyl chains to CNTs, the SDS arranges in a peculiar way; while long alkyl chains anchor them to the SWCNT's surface, the polar tail sulphate (SO_4^-) groups points to the opposite direction and form a negatively charged layer around the CNT. Addition of CdSe-ZnS QDs to the latter dispersion forms the hybrid, by immobilizing the nanocrystals on SWCNTs through polarized Zn and O interactions (**Figure 1.2.2a**). Scanning electron microscopy (SEM) and TEM images evidence the individual nanotubes on which the QDs are orderly arranged. In **Figure 1.2.2b** are reported the fluorescence and transmitted bright-field images of **QDs-SWCNTs**, showing the presence of individual and bundled SWCNTs.

The strong emission of QDs from **CdSe-ZnS QD-SWCNT** proves the absence of excited state quenching processes, probably due to the absence of effective electronic communication between the chromophores as a result of the SDS separating layer. The unquenched luminescence from **QDs-CNT** hybrids is interesting; however, to obtain significantly strong luminescence, further combinations need to be explored.

Trivalent ions of RE elements such as Eu, Tb, Yb, Nd, Er exhibit line-like and often intense emission bands from *f–f* electronic transitions that impart an unparalleled color purity.[37] Importantly, the 6s and 5d orbitals shield inner *f-f* transitions and make Ln(III) emitters virtually insensitive to the local environment. Taking advantage of these unique features, many CNT hybrid materials have been developed with Ln(III) luminophores, mainly aiming at strongly emissive smart materials.[37,38] The first attempt to produce a **Ln(III)-CNT** composite was made by Shi et al, who coated Eu-doped Y_2O_3 on MWCNTs.[39] The coating was done by an *in situ* method. First, the oxidized nanotubes were treated with YCl_3 and $EuCl_3$ in the presence of aqueous ammonia solution. Further incubation and high temperature heating of this solution up to 950 °C resulted in well ordered, strongly bound Eu-doped Y_2O_3 crystals on the CNT surface. The high resolution bright field TEM images show the deposition of some dark particles on the CNT surface. Complementary electron diffraction spectroscopy (EDS) measurements carried out on the dark spots display the characteristic signals corresponding to Eu and Y elements. These compelling evidence confirms the Eu-doped Y_2O_3 coating on SWCNTs. Interestingly, under a 355 nm pulsed laser excitation, these hybrid material displays emission signals characteristic of the Eu(III) ion. Despite the tedious preparation strategy compared to those with organic luminophores, the uncompromised emission output from **Eu-doped Y_2O_3-MWCNTs** prompted the development of similar systems. Eventually, Wei et al. reported another hybrid based on Eu(III) and Tb(III) fluorides and MWCNTs.[40] Initially, Eu(III) and Tb(III) nitrates, separately, were added to the SDS dispersed nanotube solution. As observed previously (see above), the SDS molecules covered the MWCNT's surface and their anionic sulphate (SO_4^-) part interacted with Ln(III) ions. Consequently, these interactions stabilize the Ln(III) nitrates on the MWCNTs surface. Later, the nitrate counterions were exchanged with fluoride anions and subsequent heating up to 100 °C resulted in green and red emissive Tb(III)- and Eu(III)-MWCNTs hybrid systems, respectively. The attachment of TbF_3 and EuF_3 on MWCNTs is confirmed by TEM images, showing some particles on the surface of MWCNTs. The powder XRD analysis performed on these hybrids display orthorhombic and hexagonal phases corresponding to the appended TbF_3 and EuF_3, respectively. The photoexcitation of **TbF_3-** and **EuF_3-MWCNTs** results in characteristic green and red emission, respectively, and the excitation spectra collected at the

emission maxima match with that of the pure TbF_3 and EuF_3 samples, confirming the Ln(III) ions as emission origins. The first quantitative proof for the unquenched emission from a Eu(III)-SWCNTs composite was reported from Armaroli, Bonifazi et al.[41] The hybrid was prepared using the strongly emissive, commercially available tris-dibenzoylmethane mono-1,10phenanthroline europium(III) ([Eu(DBM)$_3$(Phen)]) complex and mildly oxidized SWCNTs (see **Figure 1.2.3a**).

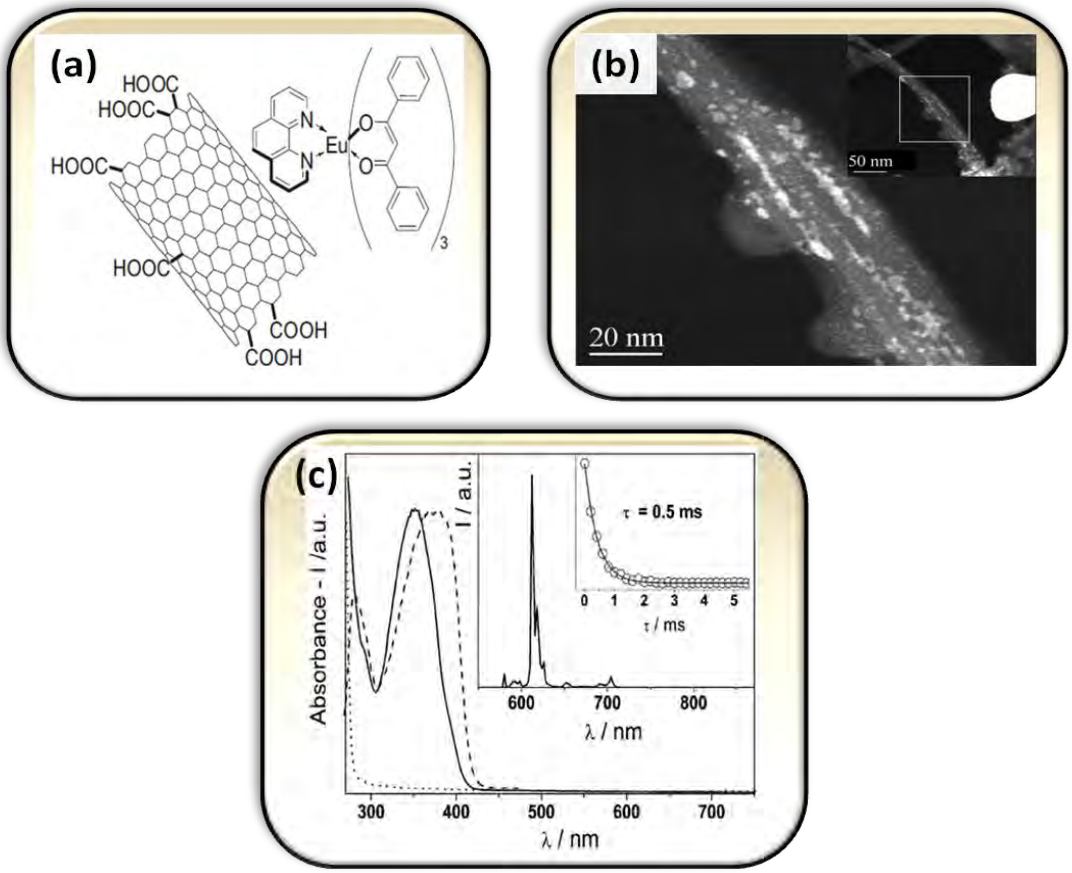

Figure 1.2.3 *(a) Chemical structure of the [Eu(DBM)$_3$(Phen)] complex and of a ox-SWCNT. (b) Z-contrast STEM images of Eu(III)-SWCNTs, taken at different magnifications using Annular Dark Field Detector. (c) Main window: Electronic absorption spectra of Eu(III)-SWCNTs (solid line) and oxidized SWCNTs (dotted line), and excitation profile of Eu(III)-SWCNTs (dashed line, λ_{em} = 614 nm) in polystyrene matrix. Inset: emission spectra (λ_{ex} = 350 nm) and decay profiles of Eu(III)-SWCNTs in polystyrene matrix at room temperature. (Adapted from ref. 40)*

The simple mixing of both units in methanol (MeOH), was followed by sonication, stirring and filtration. The filtrate was washed until the washings showed no traces of Eu(III) emission, and then dried under high vacuum. The structural characterization of **Eu(III)-SWCNTs** composite was accomplished using TGA, Raman, AFM and HR-TEM analytical techniques. The combined results from all these measurements confirm the presence of Eu(III) based material on SWCNTs surface, unequivocally. In particular, the Z-contrast STEM images taken on **Eu(III)-**

SWCNTs composite, depicted in **Figure 1.2.3b,** show high contrast spherical particles located on the walls of CNTs, with average width of 3 nm.

The above studies are complemented by localized EDS measurements, which show the signals corresponding to the Eu element. Further, the photoexcitation of the composite material suspended in MeOH and in polystyrene matrix show Eu(III) ion centered emission with maximum at ca. 612 nm. Importantly, the emission decay profiles of the hybrid systems dispersed in different media match with those of the [Eu(DBM)$_3$(Phen)] complex under the same experimental conditions, thanks to the environment insensitive luminescence properties of Ln(III) complexes (**Figure 1.2.3c**). This demonstrates the absence of quenching interactions between SWCNTs and Eu(III) complexes, despite the fact that the complex is attached directly on the carbon scaffold. Later, Wu et al. reported **Tb(III)/Eu(III)acac-Phen-MWCNTs** hybrid systems, where acac stands for acetylacetonate and Phen denotes phenanthroline ligands.[42] These composites are fabricated by a slightly modified earlier procedure.[40] The TEM images, X-ray and XPS analyses show the presence of Ln(III) complexes, and their proximity to the MWCNT's surface. Moreover, as similar to **[Eu(DBM)$_3$(Phen)]-MWCNTs** system, upon UV irradiation, both **Tb(III)/Eu(III)acac-Phen-MWCNT** hybrids show characteristic Ln(III) centered green and red emission, respectively. The lifetime of **Eu(III)acac-Phen-MWCNT** is unaltered relative to the pure complex, whereas **Tb(III)acac-Phen-MWCNT** shows prolonged metal centered emission lifetime compared to the reference system. It is assumed that the enhanced rigidity bestowed by the carbon framework to the Tb(III) complex would restrict the vibrational/rotational relaxations of the excited complex. Notably, both hybrid systems show enhanced stability against UV irradiation compared to the respective pure complexes alone under the same conditions. This interesting observation is attributed to the partial absorption, scattering or dissipation of the excitation energy by the MWCNTs; thus, only a little amount of photons are absorbed by the Ln(III) complexes, which is not sufficient to degrade the latter.

Despite the promising luminescent properties of the above mentioned CNTs materials, poor loading and undesirable desorption of the luminophores from CNTs surface limit the practical applications and scaling of these composites.

1.3 Endohedrally functionalized CNTs

Besides exohedral functionalization, driving the desired organic/inorganic material inside CNTs hallow space has been an alternative and challenging way to non-destructively functionalize nanotubes.[4,43] The encapsulation strategy provides many advantages over the CNT's outer surface

functionalization. For instance, the confinement of nanosized molecular units into CNTs may yield brand new hybrid materials with unprecedented electronic and conductivity properties. Moreover, the walls of CNTs behave as sheaths to the encapsulated chromophores and may preserve them for an unlimited period of time, which can be of great interest for many applications. Smith et al. reported the first ever C_{60} encapsulated SWCNT peapod, a decade ago. The peapod production was observed while CNTs and C_{60} molecules were produced together from a graphite source, in the presence of particles of metallic catalyst. This serendipitous encapsulation opened new avenues to confine molecules into CNT materials.[44] Afterwards, it was realized that the driving force for the spontaneous production of peapod structures is the strong hydrophobic interaction between C_{60} and the inner surface of CNTs. The HR-TEM images clearly evidence the presence of spherical balls, orderly arranged *inside* the SWCNTs, thanks to the rigid structural features of fullerenes. Following this, Iijima et al. confined gadolinium endohedral fullerenes ($Gd@C_{82}$) into SWCNTs, by heating $Gd@C_{82}$ to vapor in the presence of tip opened SWCNTs in a sealed tube (thermal vaporization method).[45] TEM images evidenced the successful encapsulation of $Gd@C_{82}$, and the EDS spectrum on a small localized area confirms the regular one-dimensional crystal array of fullerene inside CNTs. Importantly, the chemical analysis of encapsulated Gd, and the large temperature dependant electrical resistance suggests a possible electron hopping from Gd to fullerene and then to the CNTs scaffolds. Later on, the same group demonstrated the enhanced stability of C_{60} moieties inside SWCNTs using detailed TGA studies.[46] The TGA spectrum of **C_{60}@SWCNT** displays the degradation curves of reference C_{60} and CNT; in addition, a new peak was observed in between the former two, which was attributed to the weight loss from the encapsulated fullerenes, protected by the SWCNTs walls. This proves that the CNT cavities are safe storage sites for encapsulated molecules.

Apart from carbon spheres, many other small organic molecules have been driven into SWCNTs, to obtain stable and amphoterically doped CNTs.[16] By allowing the vapor of selected organic molecules to interact with tip opened, purified SWCNTs, molecules are injected inside the hollow space; weak van der Waals forces such as hydrophobic interactions and π-π stacking stabilize the guest moieties inside the hallow space, even after copious washings. Following a similar strategy tetracyanoquinodimethane (TCNQ) and tetrakis(dimethylamino)ethylene (TDAE) were encapsulated into SWCNTs and thorough washing of the resulting materials afforded **TCNQ@SWCNT** and **TDAE@SWCNT** respectively. Probing the electronic properties of **TCNQ@SWCNT** and **TDAE@SWCNT** with XRD, Raman and optical absorption measurements, substantially weaker signals were detected from SWCNT, due to strong perturbation of electronic levels by interaction with the encapsulated organic molecules. This

hypothesis is confirmed by analyzing potassium (K) doped SWCNT samples, where results match with those of **TCNQ@SWCNT** and **TDAE@SWCNT**. The recorded XRD, Raman and optical spectra of pristine SWCNTs, **TCNQ@SWCNT** and K doped SWCNTs are shown in **Figure 1.3.1**. In addition, the reduced electrical resistance exerted by the SWCNTs hybrids compared to the pristine nanotubes at room temperature under the same conditions, corroborates the existence of strong electronic interactions between confined organic molecules and SWCNTs. Eventually, **TCNQ@SWCNT** and **TDAE@SWCNT** incorporated in field effect transistor (FET) devices unambiguously proved the p- and n-type doping of SWCNTs, respectively. This demonstrates the amphoteric electronic nature of CNTs that, notably, can be controlled and finely tuned by changing the guest molecules, with different relative ionization energy and electron affinity values.

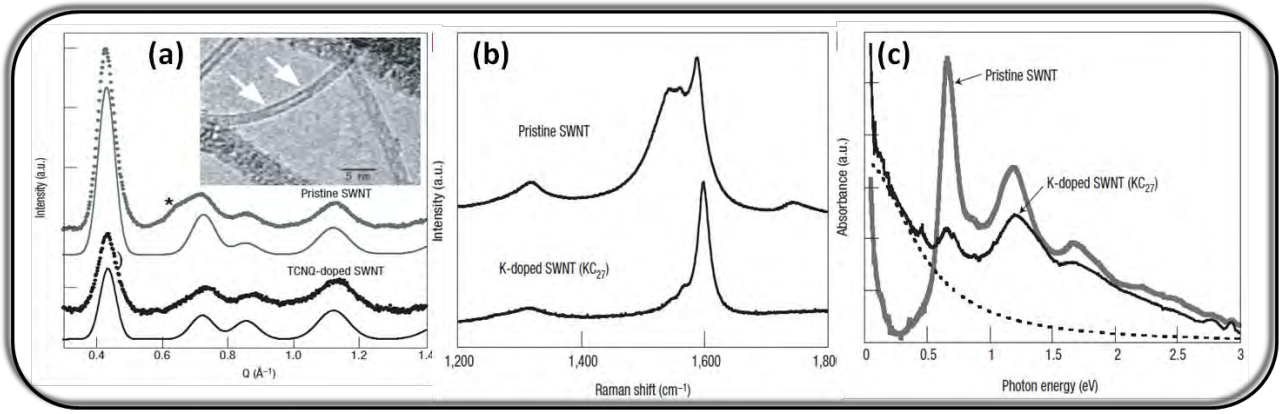

Figure 1.3.1 *(a) Observed (dotted lines) and simulated (solid lines) XRD patterns of pristine and TCNQ@SWCNT.The inset shows a TEM image of tetracene/SWCNTs. The arrows indicate the boundary between an empty region and those filled with tetracene molecules. (b)Raman spectra and (c) optical spectra of pristine SWCNTs and K doped SWCNTs.(Adapted from ref.15)*

A similar method has been employed by many groups to drive other organic molecules into CNTs, and the obtained hybrids show interesting electronic and optical properties. For example, β-carotene (**Figure 1.3.2a**) and squarilium dye, when confined into SWCNT display excited state energy transfer interactions with the host unit under illumination. Despite the fact that TCNQ, TDAE, β-carotene and squarilium guests are organic chromophores, the difference in band gap energy, position of frontier orbitals and binding affinity with the walls of CNTs, determine the nature of the electronic interaction with the carbon scaffolds. In these cases, the excited state processes have been closely monitored by non destructive XRD, Raman and photophysical techniques.[47-49] The XRD profiles of both **β-carotene@SWCNT** and **squarilium@SWCNT** hybrids show reduction in (10) peak intensity, as similar to TCNQ@SWCNT, compared to that of pristine SWCNTs. The numerical simulation on **β-**

carotene@SWCNT's XRD pattern suggests that the confinement of molecules inside CNTs would be the major reason for SWCNT's reduced (10) peak intensity. The Raman features of CNTs are highly sensitive to any perturbations of electronic levels and, hence, Raman spectroscopy is considered as an optimal tool to discriminate the nature of electronic interaction between different guests and nanotubes. Raman spectra of **β-carotene@SWCNT** and **squarilium@SWCNT** show characteristic tangential resonance frequency with unchanged spectral position compared to the pristine SWCNTs under the same conditions. It's worth mentioning that n-type, K doped SWCNTs show reasonable shift in the G-band frequency (**see Figure 1.3.1b**). Hence, the lack of shift in the G-band frequencies of **β-carotene@SWCNT** and **squarilium@SWCNT** confirms the absence of electron transfer (ET) processes. The low energy radial breathing mode (RBM) peaks corresponding to SWCNTs in the hybrids show slight changes in shape, and this can be attributed to the interaction of functionalized molecules with CNTs.

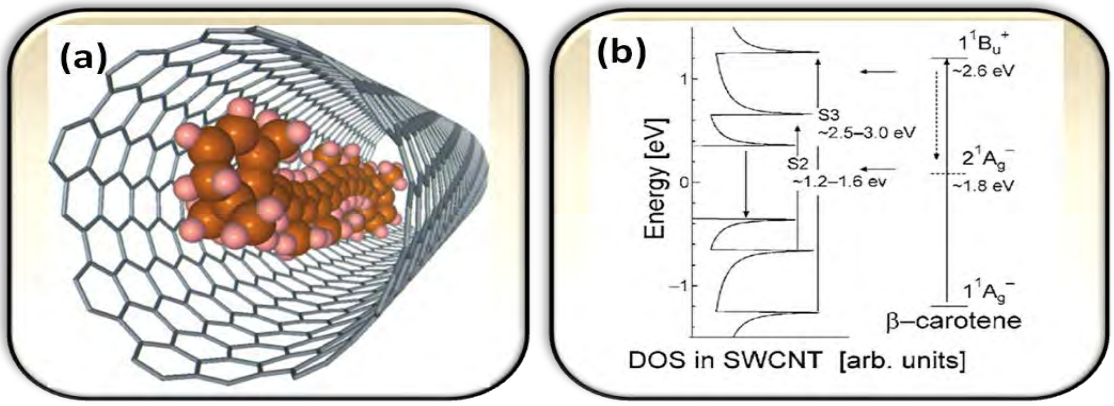

Figure 1.3.2 *Representation of β-carotene encapsulated (12,8) SWCNT (a); energy transfer processes between the electronic energy levels of the two components upon exciting the β-carotene (b). (Adapted from ref. 46)*

Photoexcitation of the hybrids shows no emission signal corresponding to the encapsulated organic units. On the other hand, the photoluminescence (PL) mapping of excitation wavelength and emission intensities observed from **β-carotene@SWCNT** and **squarilium@SWCNT** shows signals corresponding to the emission from certain SWCNTs, which are absent in the PL map of pristine SWCNTs. Light excitation of the encapsulated non-emitting organic molecules, lead to activation of luminescence of CNTs to some extent. Owing to CNT's low molar extinction coefficient values, the direct excitation of the tubes would hardly result in any emission. Thus, photosensitization of CNTs by the excited organic molecules through energy transfer is the plausible explanation of the observed emission signals from CNTs. The suggested energy transfer mechanism is shown in **Figure 1.3.2b**.

All the above described examples illustrate the electron/energy donating and accepting ability of CNT scaffolds, when suitable guest molecules are encapsulated within. It is important to note that both excited state processes can effectively quench the emission properties of the confined luminophores. Unlike other luminophore@CNT composites, where the guest is completely quenched, Loi et al. have reported a luminescent, sexithiophene (6T) encapsulated SWCNT (**6T@SWCNT-1**) hybrid.[50] The encapsulation procedure consists of the addition of 6T to a dispersion of SWCNT in toluene and, after evaporating the solvent, the dried material was sealed inside a quartz tube at a reduced pressure. The tube was then heated for 3 days and the obtained black material was sonicated, centrifuged, filtered and washed repeatedly in toluene, to remove the surface adsorbed 6Ts. The resultant **6T@SWCNT-1** was used for the structural and photophysical analyses. The HR-TEM images of **6T@SWCNT-1** display some disoriented material with CNTs, but deep structural insight is hampered by the destructive electron beam used during the measurements. The Raman spectrum of **6T@SWCNT-1** shows a small red shift in the RBM peak position of SWCNT, showing the functionalization with 6T. Further, the characteristic G-band peak positions are unaffected compared to the pristine SWCNTs. Therefore, luminescence quenching by electron transfer between 6T and SWCNTs do not occur. The optical absorption spectrum of **6T@SWCNT-1** displays red shifted 6T features, characteristic of organic molecules-CNT composites. Notably, the photoexcitation of encapsulated material dispersed in dimethylformamide (DMF) solution shows a broad and, compared to that of the reference 6T, poorly resolved emission band (**Figure 1.3.2a)**. The corresponding excitation spectra collected at 550 nm from the hybrid and the reference compound largely superimpose each other, substantiating 6T as the origin of the luminescence band in **6T@SWCNT-1**. However, the excited state lifetime is shorter (563 ps) than that of 6T (813 ps), which is rationalized by the strong guest-host interactions, those would develop new non-radiative decay channels. In parallel to this, Kalbac et al. performed detailed *in situ* Raman spectroelectrochemical studies on a similar system (**6T@SWCNT-2**).[26] The sample 6T@SWCNT-2 was prepared by heating 6T and SWCNTs under vacuum in a sealed tube. The Raman spectrum of **6T@SWCNT-2** shows red shift in the RBM features of SWCNT, with no significant change in the tangential peak positions, as similar to the above. Surprisingly, upon laser excitation (1.83 eV) no luminescence signal was observed from **6T@SWCNT-2** whereas, under the same conditions, pure 6T shows strong photoluminescence. This contradicts the observation of Loi et al. of a strong emission from **6T@SWCNT-1**.

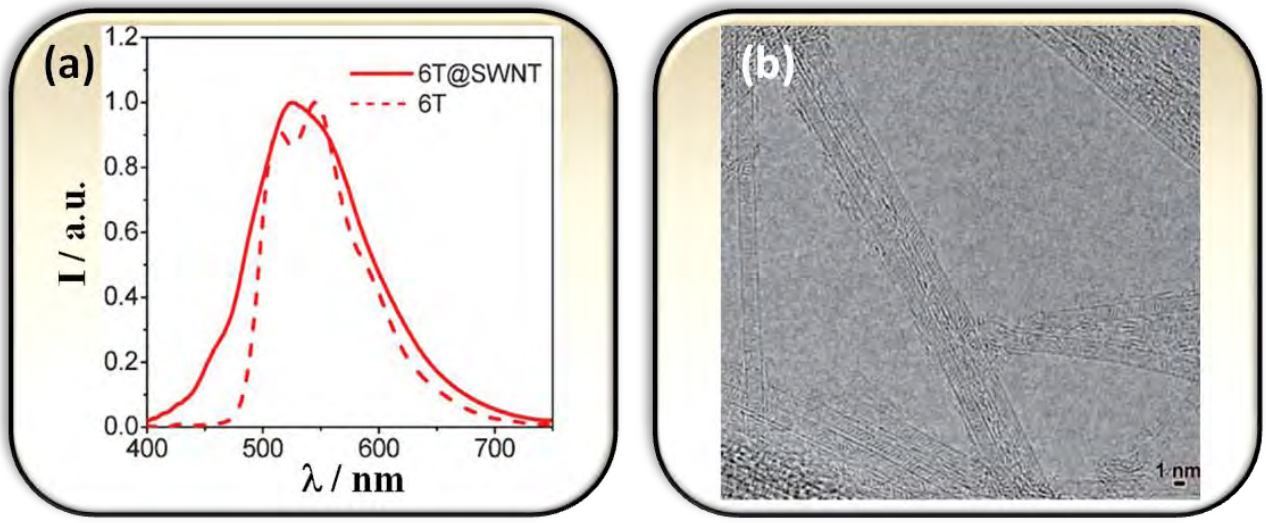

Figure 1.3.2 *(a) Emission spectra of 6T@SWCNT (solid line) and 6T (dashed line) in DMF, collected upon excitation at 550 nm. (b) HR-TEM images of coronenes encapsulated SWCNTs. (Adapted from ref. 49 and 50 respectively)*

Since electron transfer between host and guest units cannot occur, the exciton energy transfer from 6T to SWCNTs is suggested as the reason for luminescence quenching. The *in situ* Raman spectroelectrochemical studies on **6T@SWCNT-2** corroborate the absence of electron transfer interactions between 6T and SWCNT by changing the electrode potentials in both directions. At relatively high potential, the doping effect was observed for confined 6T molecules and, importantly, such effect was reversible. On the other hand, the pure films of 6T deposited on the electrode show limited stability. This confirms the extraordinary protection offered by the SWCNT to the encapsulated 6T.

Another structurally interesting SWCNTs hybrid was prepared with coronene. The vapor phase interactions between coronene and SWCNTs yielded coronene confined SWCNTs (**coronene@SWCNTs**), where the coronene units are uniformly stacked inside the nanotubes.[51] The intermolecular π-π stacking and hydrophobic interactions with CNTs help coronene to arrange in a columnar fashion inside SWCNTs. These 1-D arrays of conductive organic molecules inside CNTs are highly appealing for electronic devices and it should be noted that, without the CNT template, such molecular packing cannot occur. **Figure 1.3.2b** shows the HR-TEM image of the **coronene@SWCNT** sample, which evidences the 1-D array inside SWCNTs. The interactions between host-guest moieties are reflected by the red shifted SWCNT's RBM peak position, whilst no shift was observed in the tangential mode frequency. The photoexcitation of **coronene@SWCNT** at 356 nm leads to broad, less resolved and significantly red-shifted emission features, compared to coronene alone in hexane. These emission changes are rationalized by the strong intermolecular π-π interactions of coronene units. However, the

excitation spectrum collected at 550 nm shows the exact mirror image of the emission bands, suggesting coronene as the emission origin in the hybrid. The photoluminescence quantum yield of **coronene@SWCNT** hybrid is calculated as 15%, after correction for CNT absorption. This value is remarkably high among organic chromophores encapsulated in CNTs, but it is slightly lower than that of coronene in ethanol solution (23%); this suggests the occurrence of energy transfer to some extent. The PL mapping shows some bright emission from SWCNTs containing coronene units, differently from the pristine SWCNTs, and this corroborates the above statement.

In contrast to the often documented energy transfer quenching processes, quaterthiophene (4T) confined SWCNTs (**4T@SWCNT**) evidences charge transfer from organic motifs to CNT scaffolds.[25] The encapsulation procedure was the same as that of **6T@SWCNT**. Unlike other confined materials, the Raman features RBM and tangential modes show some significant changes. The downshift of the G-band along with low intense RBM peak suggests electron doping in SWCNTs and, notably, laser excitation at 514.5 nm shows bleaching of the emission of encapsulated 4T. These observations points to photoinduced electron transfer from 4T to SWCNTs. Thus, as stated above, confinement of organic guest moieties with different electronic properties enables fine tuning of excited state processes, and consequently alters the emission output from the CNT hybrids.

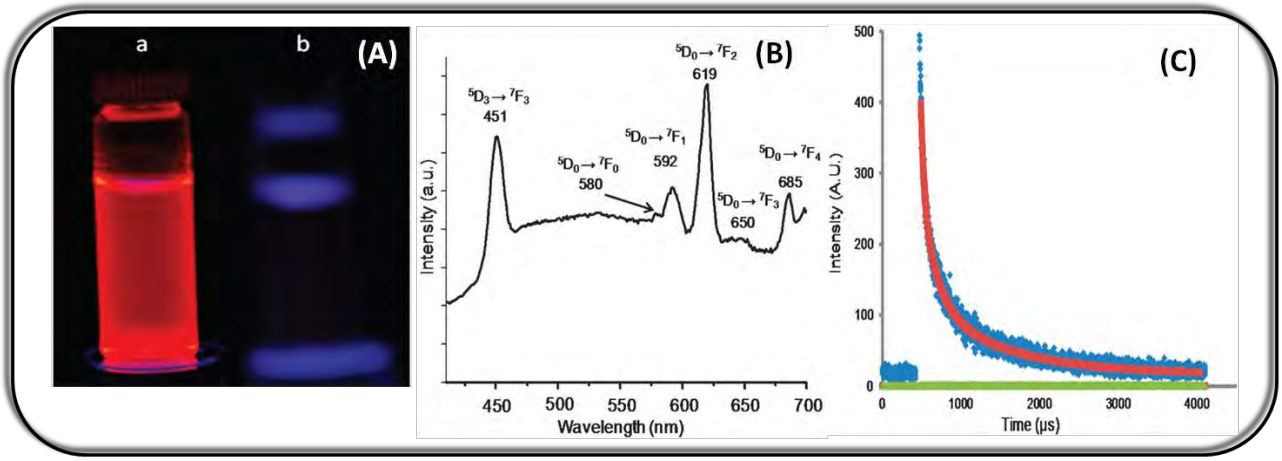

Figure 1.3.3 *(A) Luminescence images (λ_{ex} / λ_{em} = 315–415/619 nm) of (a) Eu-SWCNT in 1% pluronic F127 solution at 4 mM [Eu(III)] concentration; (b) Eu_2O_3 nanoparticles in 1% pluronic F127 at the same concentration. (B) Eu-SWCNT emission spectrum in aqueous media (excitation 390 nm, integration time 0.1 s) at 4 mM [Eu(III)] concentration. (C) Fluorescence decay curve (blue = actual decay, red = fit, green = residual) of Eu-SWCNT in 1% pluronic F127 solution at 4 mM[Eu(III)] concentration (λ_{ex} =390 nm, λ_{em} =619 nm). (Adapted from ref.54)*

As similar to the exohedrally functionalized CNTs, the lack of luminescence from most of the confined organic molecules due to the excited state processes, can be mitigated by inserting

inorganic guest molecules, especially Ln(III) complexes. A wide variety of inorganic materials such as metal oxides, nanoparticles, coordination compounds have been encapsulated effectively inside CNTs using different techniques, aiming at various applications.[4,52-54] The first luminescent, inorganic material confined SWCNT was demonstrated by Sitharaman et al.[55]The **Eu@SWCNT** was prepared by growing SWCNTs on Eu_2O_3 catalyst particles, following chemical vapor deposition (CVD) method. Generally, a considerable amount of metallic impurities can be found inside the CNTs prepared via CVD method, as a consequence of the template assisted growing process. Similarly, in the present case, HR-TEM analysis showed the fully grown SWCNTs containing significant amount of Eu(III) metal ions at the edges and inside the nanotube channels. These Eu(III) confined SWCNTs are dispersed in pluronic F-127 solution and the same is used for photoluminescence studies. Upon 390 nm photoexcitation, the solution containing **Eu@SWCNT** showed characteristic Eu(III) emission with maximum at 619 nm. The low molar extinction coefficient of Eu(III) hampers its direct light excitation, and hence the observed emission from **Eu@SWCNT** should be possible only by the photosensitization of SWCNTs, via energy transfer to the Eu(III) ion. The emission spectrum displays all the characteristic lines of Eu(III) with an overall quantum efficiency of 1.7% and the average lifetime of 161 μs. These values are considered as relatively high if compared to other non emissive analogues; however, the lack of strong emission signals is attributed to the combined effect of low sensitization efficiency (40.5%), Eu(III) ion interaction with –OH vibronic oscillators and the possible back energy transfer from the excited metal to the CNTs.

1.4 Concluding remarks

In this chapter, we have overviewed different strategies to produce CNT hybrids, along with their electronic and luminescence properties. Composites of CNTs and organic chromophores show outstanding electronic properties compared to the currently available materials. In particular, endohedral functionalization allows control and fine tuning of the Fermi levels of CNTs. The CNT composites prepared using inorganic luminophores including quantum dots display reasonable emission efficiency with additional functional properties. Such advanced properties of CNT hybrids are envisaged to have strong impact on the development of future lighting, bio-diagnostic and sensor concepts.

Despite several advantages, both endo- and exohedral functionalization still bestow hard challenges on the way to the preparation of robust CNT hybrids. Most of the surface assembled CNT composites suffer by desorption of the attached chromophores, whilst controlling the

loading of materials on the surface of CNTs is difficult. Similarly, chromophore confined CNTs suffer from the low concentration of encapsulated materials and harsh preparation strategies. Importantly, undesired electron / energy transfer processes quench the luminescence properties of chromophores attached to CNTs. These limitations call for further research on CNT hybrids to impart them the properties needed to be utilized in real-world devices.

1.5 References

1. N. Armaroli and V. Balzani, *Energy for a Sustainable World. From the Oil to a Sun Powered Future*, Wiley-VCH, Weinheim, Germany, 2011.
2. G. F. Wang, X. M. Tao, W. Chen, R. X. Wang and A. Yang, *J. Lumin.*, **2007**, *126*, 602-606.
3. M. Bansal, R. Srivastava, C. Lal, M. N. Kamalasanan and L. S. Tanwar, *Nanoscale*, **2009**, *1*, 317-330.
4. D. Eder, *Chem. Rev.*, **2010**, *110*, 1348-1385.
5. Nanomaterials, http://ec.europa.eu/environment/chemicals/nanotech/.
6. Y. L. Zhao and J. F. Stoddart, *Acc. Chem. Res.*, **2009**, *42*, 1161-1171.
7. D. A. Britz and A. N. Khlobystov, *Chem. Soc. Rev.*, **2006**, *35*, 637-659.
8. M. J. O'Connell, P. Boul, L. M. Ericson, C. Huffman, Y. H. Wang, E. Haroz, C. Kuper, J. Tour, K. D. Ausman and R. E. Smalley, *Chem. Phys. Lett.*, **2001**, *342*, 265-271.
9. K. Nobusawa, A. Ikeda, J. I. Kikuchi, S. I. Kawano, N. Fujita and S. Shinkai, *Angew. Chem. Int. Ed.*, **2008**, *47*, 4577-4580.
10. Z. X. Zhang, Y. K. Che, R. A. Smaldone, M. A. Xu, B. R. Bunes, J. S. Moore and L. Zang, *J. Am. Chem. Soc.*, **2010**, *132*, 14113-14117.
11. A. Llanes-Pallas, K. Yoosaf, H. Traboulsi, J. Mohanraj, T. Seldrum, J. Dumont, A. Minoia, R. Lazzaroni, N. Armaroli and D. Bonifazi, *J. Am. Chem. Soc.*, **2011**, *133*, 15412-15424.
12. M. S. Arnold, A. A. Green, J. F. Hulvat, S. I. Stupp and M. C. Hersam, *Nat. Nanotechnol.*, **2006**, *1*, 60-65.
13. C. Backes, S. Bosch, U. Mundloch, F. Hauke and A. Hirsch, *ChemPhysChem*, **2011**, *12*, 2576-2580.
14. R. Krupke, F. Hennrich, H. von Lohneysen and M. M. Kappes, *Science*, **2003**, *301*, 344-347.
15. Y. Maeda, S. Kimura, M. Kanda, Y. Hirashima, T. Hasegawa, T. Wakahara, Y. F. Lian, T. Nakahodo, T. Tsuchiya, T. Akasaka, J. Lu, X. W. Zhang, Z. X. Gao, Y. P. Yu, S. Nagase, S. Kazaoui, N. Minami, T. Shimizu, H. Tokumoto and R. Saito, *J. Am. Chem. Soc.*, **2005**, *127*, 10287-10290.
16. T. Takenobu, T. Takano, M. Shiraishi, Y. Murakami, M. Ata, H. Kataura, Y. Achiba and Y. Iwasa, *Nat. Mater.*, **2003**, *2*, 683-688.
17. S. Iijima, *Nature*, **1991**, *354*, 56-58.
18. R. A. Hatton, A. J. Miller and S. R. P. Silva, *J. Mater. Chem.*, **2008**, *18*, 1183-1192.
19. S. Kazaoui, N. Minami, R. Jacquemin, H. Kataura and Y. Achiba, *Phys. Rev. B: Condens. Matter Mater. Phys.*, **1999**, *60*, 13339-13342.

20. S. Kazaoui, N. Minami, N. Matsuda, H. Kataura and Y. Achiba, *Appl. Phys. Lett.*, **2001**, *78*, 3433-3435.
21. S. M. Bachilo, M. S. Strano, C. Kittrell, R. H. Hauge, R. E. Smalley and R. B. Weisman, *Science*, **2002**, *298*, 2361-2366.
22. M. J. O'Connell, S. M. Bachilo, C. B. Huffman, V. C. Moore, M. S. Strano, E. H. Haroz, K. L. Rialon, P. J. Boul, W. H. Noon, C. Kittrell, J. P. Ma, R. H. Hauge, R. B. Weisman and R. E. Smalley, *Science*, **2002**, *297*, 593-596.
23. Y. H. Lin, Y. C. Lai, C. T. Hsu, C. J. Hu and W. K. Hsu, *Phys. Chem. Chem. Phys.*, **2011**, *13*, 7118-7122.
24. D. M. Guldi, G. M. A. Rahman, F. Zerbetto and M. Prato, *Acc. Chem. Res.*, **2005**, *38*, 871-878.
25. L. Alvarez, Y. Almadori, R. Arenal, R. Babaa, T. Michel, R. Le Parc, J. L. Bantignies, B. Jousselme, S. Palacin, P. Hermet and J. L. Sauvajol, *J. Phys. Chem. C*, **2011**, *115*, 11898-11905.
26. M. Kalbac, L. Kavan, S. Gorantla, T. Gemming and L. Dunsch, *Chem.-Eur. J.*, **2010**, *16*, 11753-11759.
27. D. W. Long, G. Z. Wu and A. B. Wu, *J. Phys. Chem. C*, **2008**, *112*, 13000-13003.
28. C. Ehli, G. M. A. Rahman, N. Jux, D. Balbinot, D. M. Guldi, F. Paolucci, M. Marcaccio, D. Paolucci, M. Melle-Franco, F. Zerbetto, S. Campidelli and M. Prato, *J. Am. Chem. Soc.*, **2006**, *128*, 11222-11231.
29. G. M. A. Rahman, D. M. Guldi, S. Campidelli and M. Prato, *J. Mater. Chem.*, **2006**, *16*, 62-65.
30. V. Sgobba, G. M. A. Rahman, D. M. Guldi, N. Jux, S. Campidelli and M. Prato, *Adv. Mater.*, **2006**, *18*, 2264-2269.
31. J. Liu, O. Bibari, P. Mailley, J. Dijon, E. Rouviere, F. Sauter-Starace, P. Caillat, F. Vinet and G. Marchand, *New J. Chem.*, **2009**, *33*, 1017-1024.
32. E. W. McQueen and J. I. Goldsmith, *J. Am. Chem. Soc.*, **2009**, *131*, 17554-17556.
33. A. Ahmad, T. Kurkina, K. Kern and K. Balasubramanian, *ChemPhysChem*, **2009**, *10*, 2251-2255.
34. Q. W. Li, B. Q. Sun, I. A. Kinloch, D. Zhi, H. Sirringhaus and A. H. Windle, *Chem. Mater.*, **2006**, *18*, 164-168.
35. V. Biju, T. Itoh, Y. Baba and M. Ishikawa, *J. Phys. Chem. B*, **2006**, *110*, 26068-26074.
36. S. Chaudhary, J. H. Kim, K. V. Singh and M. Ozkan, *Nano Lett.*, **2004**, *4*, 2415-2419.
37. J.-C. G. Bünzli, *Acc. Chem. Res.*, **2006**, *39*, 53-61.
38. D. Parker and J. A. G. Williams, *J. Chem. Soc.-Dalton Trans.*, **1996**, 3613-3628.
39. D. L. Shi, J. Lian, W. Wang, G. K. Liu, P. He, Z. Y. Dong, L. M. Wang and R. C. Ewing, *Adv. Mater.*, **2006**, *18*, 189-193.
40. X. W. Wei, J. Xu, X. H. Song, Y. H. Ni, P. Zhang, C. J. Xia, G. C. Zhao and Z. S. Yang, *Mater. Res. Bull.*, **2006**, *41*, 92-98.
41. G. Accorsi, N. Armaroli, A. Parisini, M. Meneghetti, R. Marega, M. Prato and D. Bonifazi, *Adv. Funct. Mater.*, **2007**, *17*, 2975-2982.
42. H. X. Wu, W. M. Cao, J. Wang, H. Yang and S. P. Yang, *Nanotechnology*, **2008**, *19*, 345701-345709.
43. A. N. Khlobystov, D. A. Britz and G. A. D. Briggs, *Acc. Chem. Res.*, **2005**, *38*, 901-909.
44. B. W. Smith, M. Monthioux and D. E. Luzzi, *Nature*, **1998**, *396*, 323-324.

45. K. Hirahara, K. Suenaga, S. Bandow, H. Kato, T. Okazaki, H. Shinohara and S. Iijima, *Phys. Rev. Lett.*, **2000**, *85*, 5384-5387.
46. M. Zhang, M. Yudasaka, S. Bandow and S. Iijima, *Chem. Phys. Lett.*, **2003**, *369*, 680-683.
47. K. Yanagi, K. Iakoubovskii, S. Kazaoui, N. Minami, Y. Maniwa, Y. Miyata and H. Kataura, *Phys. Rev. B: Condens. Matter Mater. Phys.*, **2006**, *74*, 155420-155424.
48. K. Yanagi, K. Iakoubovskii, H. Matsui, H. Matsuzaki, H. Okamoto, Y. Miyata, Y. Maniwa, S. Kazaoui, N. Minami and H. Kataura, *J. Am. Chem. Soc.*, **2007**, *129*, 4992-4997.
49. K. Yanagi, Y. Miyata and H. Kataura, *Adv. Mater.*, **2006**, *18*, 437-441.
50. M. A. Loi, J. Gao, F. Cordella, P. Blondeau, E. Menna, B. Bartova, C. Hebert, S. Lazar, G. A. Botton, M. Milko and C. Ambrosch-Draxl, *Adv. Mater.*, **2010**, *22*, 1635-1639.
51. T. Okazaki, Y. Iizumi, S. Okubo, H. Kataura, Z. Liu, K. Suenaga, Y. Tahara, M. Yudasaka, S. Okada and S. Iijima, *Angew. Chem. Int. Ed.*, **2011**, *50*, 4853-4857.
52. W. Chen, Z. L. Fan, B. Zhang, G. J. Ma, K. Takanabe, X. X. Zhang and Z. P. Lai, *J. Am. Chem. Soc.*, **2011**, *133*, 14896-14899.
53. G. E. Fernandes, M. B. Tzolov, J. H. Kim, Z. J. Liu and J. Xu, *J. Phys. Chem. C*, **2010**, *114*, 22703-22709.
54. B. K. Pradhan, T. Kyotani and A. Tomita, *Chem. Commun.*, **1999**, 1317-1318.
55. B. Sitharaman, S. Rajamani and P. K. Avti, *Chem. Commun.*, **2011**, *47*, 1607-1609.

Chapter 2

Luminophores

2.1 Introduction

Photoluminescence is the emission of light from any substance and occurs from electronically excited states by absorbing light energy.[1] An atom or molecule that emits light upon photoirradiation is called luminophore. Luminescence can be either fluorescence or phosphorescence, based on parity allowed or forbidden transitions, respectively. Organic luminophores are typically fluorescence emitters at room temperature and their emission quantum yields can be significantly high (up to above 50%) with lifetimes in the nanosecond (ns) time scale. These compounds can further show spin forbidden transitions from the lowest-lying excited triplet state to the ground state, which are long-lived (in the range of microseconds (μs) to seconds (s) time scale) and hence observable only in rigid media and/or at low temperature (e.g. 77 K).[1] A few lanthanide (Ln) ions, such as Eu(III), Tb(III), Sm(III) also show parity forbidden *f-f* transitions, resulting in intense emission output and long decay time.[2] Interestingly, some families of transition metal complexes show remarkable luminescence properties. For example, $[Ru(bpy)_3]^{2+}$ and its analogues, where bpy stands for 2,2'-bipyridine, displays red-orange emission and long lifetime due to a particular type of electronic transition, metal-to-ligand charge transfer (MLCT).[3] Photophysical studies show that photoexcitation promotes an electron from Ru(II) metal ion d orbital to the lowest lying π^* orbital of a bipyridine ligand. The corresponding deexcitation process is accompanied by emission of light.

In general, the emission properties of luminophores are controlled by different factors such as solvent, immediate environment, excited state interactions etc., eventually resulting in varying emission properties. This chapter focuses on inorganic luminophores, especially luminescent Ln(III) and Copper(I) complexes, and their photophysical properties in different media. My work in this field is aimed at creating a library of inorganic emitters suitable for the preparation of carbon nanotube hybrids.

2.2 Lanthanide emitters

The luminescence of either Ln ions or Ln complexes has been studied for many decades and still remains the object of intensive investigation.[2,4] Their unique emission properties have been exploited in many important applications, such as telecommunication,[5] optoelectronics,[6,7] biodiognostics[8,9] and sensors.[10,11] In general, Lanthanides are a group of 14 metals which follow lanthanum (La) in the periodic table, and exhibit the common electronic configuration $\mathbf{[Xe]4f^n5d^16s^2}$, where n = 0-14. Apart from La (n = 0) and lutetium (Lu) (n = 14), all the other lanthanides have partially filled 4f orbitals and show paramagnetic behavior. The Ln metals typically show +3 oxidation state with some exceptions like Ce (+4), and Sm, Eu and Yb (+2), due to comparatively stable, empty ($\mathbf{[Xe]4f^0}$), half ($\mathbf{[Xe]4f^7}$) and completely filled ($\mathbf{[Xe]4f^{14}}$) orbital electronic configurations.[4] Along the series, the shielding effect of the 4f shell decreases and, consequently, the effective nuclear charge increases; this results in a decrease of size (lanthanide contraction) and an increase in ionization energy.[12] Owing to the small size and high nuclear charge, lanthanide ions are considered "hard acids", and any negatively charged organic ligands containing oxygen, nitrogen or sulphur, basically O > N > S in terms of affinity, coordinates to Ln ions, yielding coordination number up to 12, with 8 and 9 as the most common. Water molecules show strong affinity to bind with Ln ions and dissipate the excited state energy of the ions non-radiatively.[13] This explains the reason for low emission efficiency from hydrated Ln(III) ions (*vide infra*); removal of water molecules from the coordination sphere is difficult. Notably, the 4f electrons are buried under outer 5s and 5p valence orbitals; hence, the intrinsic properties of the Ln ions are rather insensitive to environmental factors.[12] On the other hand, the properties of the complexes are mostly dictated by the specific bound organic ligands.

The emission properties of lanthanides stem from *f-f* internal transitions, and they yield unique line-like emission peaks throughout the visible and near infrared (NIR) spectral regions.[2,4] In principle, these transitions are parity forbidden ($\Delta S \neq 0$),[4] but the exceptionally strong spin-orbit coupling of lanthanides overcomes the selection rules and drives the electronic transitions. These forbidden transitions result in two major consequences. First, the molar extinction coefficient ($\boldsymbol{\varepsilon}$) of all Ln(III) ions is extremely low.[2,4,14] This strongly hampers the direct excitation of the metal ions with conventional lamps, making necessary the use of more powerful laser sources. Attaching organic chromophores helps to circumvent this drawback, by exerting the "*antenna effect*" through efficient energy transfer processes.[2,4,5,15] Additionally, the ligands provide extra protection to the metal center and help to dissolve them in organic solvents. This eases the processing and implementation of Ln ions in many applications. Most importantly, the

emission properties of Ln(III) ions are governed by the intrinsic electronic features of the organic chromophores.[15] The second issue brought about by the forbidden transition is the long emission decay time, which is placed in the μs to milliseconds (ms) time scale.[2,4] Actually this is one of the key properties of the Ln emitters which stimulate their use in biodiagnostic tools.[9] On the other hand, the long lifetime opens many non-radiative deactivation pathways through interactions with the surrounding medium, which can ultimately reduce the overall emission efficiency (*vide infra*).[12] As mentioned above, the quantum efficiency of Ln(III) emission depends on the nature of the organic ligands; however, the NIR emissive Ln(III) ions show intrinsically weaker quantum yields compared to those emitting visible light, due to the *energy gap law* effect.[16]

The photosensitization of Ln(III) ions through energy transfer is crucial to impart lanthanide compounds strong emission properties. Transferring the energy from organic chromophores and some inorganic crystal lattices (for example Y_2O_3) to Ln(III) ions occurs through either *coulombic* or *exchange* interactions. The *coulombic interaction* takes place via electromagnetic field and so it is not necessary to have a chemical bond between donor and acceptor moieties. The excited donor molecule induces dipole oscillation in the acceptor unit and establishes a dipole-dipole interaction, and via this route the excited state of the sensitizer transfers its energy to Ln(III) ions. The efficiency of this energy transfer process is indirectly proportional to the sixth power of interchromophoric distance. This type of mechanism was initially proposed by Förster, and thus it is termed *Förster mechanism.*[17] In contrast, the *exchange* interaction occurs through double electron transfer between the donor and acceptor frontier orbitals. This process is efficient at shorter interchromophoric distances; if this distance is increased, the rate of the reaction will be decreased exponentially. This concept was developed by David L. Dexter, hence it is known as *Dexter* mechanism.[18] Both mechanisms are schematically represented in **Figure 2.2.1**. The detailed background of these mechanisms can be rationalized by quantum mechanical methods.

The structural and electronic features of the systems dictate the type of energy transfer mechanism. For example, inorganic phosphors have Ln(III) metal ions and other elements at a defined distance in crystal lattices of the metal oxide. Hence, *Förster* mechanism is the most probable way to transfer the energy to the Ln(III) ions. On the other hand, in Ln(III) complexes, the energy is transferred to the Ln(III) ions from the excited triplet states of the directly attached ligands and Dexter mechanism prevails.[15] The back energy transfer from excited states of the metal ions to the sensitizer is possible through the same mechanisms; however, in most cases, the process is thermodynamically not favored.

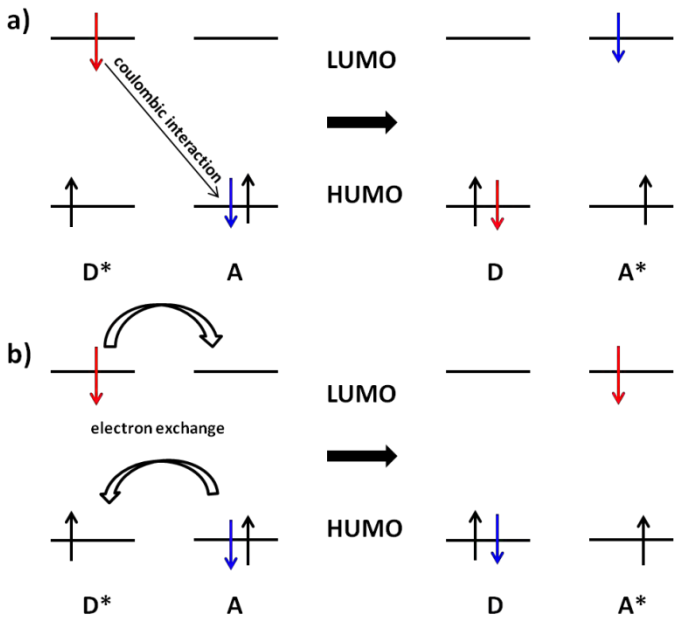

Figure 2.2.1 *Graphical representation of singlet-singlet (a) Förster and (b) Dexter type energy transfer mechanisms.*

The excited states of the Ln(III) ions exhibit with mixed spin multiplicities due to strong spin-orbit coupling effects. The same affects the organic chromophores attached to Ln(III) metal ions and facilitates intersystem crossing to populate the triplet state. This phenomenon is known as *"heavy atom effect"*.[2,4] This explains the commonly observed triplet state energy transfer from the ligand to the metal ions. As stated above, due to parity forbidden transitions, the Ln(III) ions excited state are long-lived and thus prone to non-radiative pathways through interaction with other species in the surroundings such as –OH, –NH or –CH vibronic states of solvent molecules.[2] In the Ln series, Sm(III), Eu(III), Tb(III) and Dy(III) ions are the stronger emitters with band gap energies of 7400, 12300, 14200 and 7850 cm^{-1}, respectively. The vibrational frequencies of –OH, –NH and –CH are 3400, >3000 and 2900-3100 cm^{-1}, respectively. Due to the high bandgap energy, apart from Tb(III), the other 3 metal excited states resonate with the mentioned vibronic states, and consequently rapidly deactivate to the ground state non-radiatively. This quenching effect is linear to the number of water molecules around the metal ion, and therefore the bound water molecules should be kept away from the coordination sphere of Ln(III) ions. This problem can be possibly overtaken by using deuterium substituted solvents, where the lower oscillating vibration ($\nu_{O\text{-}D}$ = 2400 cm^{-1}) minimizes the quenching due to weak resonance. The interactions between Ln(III) excited states and –OH and –OD vibronic oscillators are depicted in **Figure 2.2.2**. Another option is to use chelating organic ligands, which possibly can keep the vibronic quenchers away from the metal center.

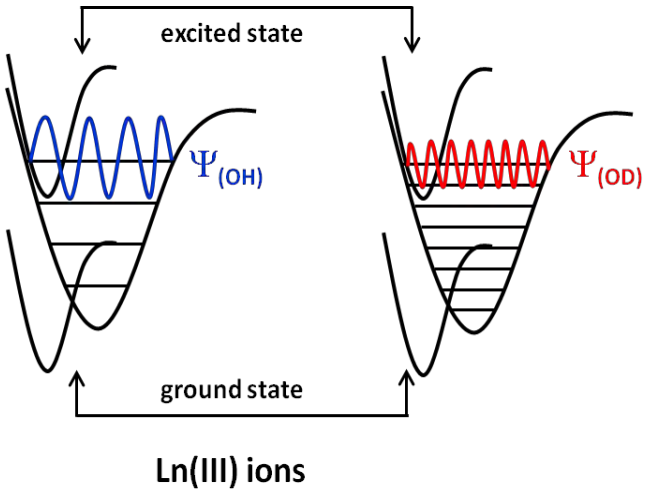

Figure 2.2.2 *Representation of energy resonance between Ln(III) ion excited states and –OH and –OD vibronic oscillators.*

2.2.1 Photophysical properties of Eu(III) and Tb(III) ions

Among lanthanides, green and red emissive terbium (Tb) and europium (Eu) trivalent ions respectively, are widely studied due to their high luminescence efficiency. The emission of Eu(III) originates from $^5D_0$ to ^7F_j internal transitions, where j = 0-6 (**Figure 2.2.3**).[2,4] The $^5D_0 \rightarrow {}^7F_1$ transition is magnetic dipolar (M.D) in nature and hence, it is insensitive to ligand field effects. Other transitions involving $^7F_{2,4,6}$ have electric dipolar (E.D) nature, which are highly affected by the symmetry, ligand field and overall dipole moment of the complexes.[19] Especially, the $^5D_0 \rightarrow {}^7F_2$ emission peak is known as "*hypersensitive*";[19,20] this feature makes it particularly interesting and allows having more information about the symmetry of primary coordination sphere.[19] This issue will be discussed in detail in chapter **4**. Other transitions, $^5D_0 \rightarrow {}^7F_{0,3,5}$ can acquire magnetic dipole intensity based on spin-orbit coupling. Experimental data suggests that $^5D_0 \rightarrow {}^7F_1$ and $^5D_0 \rightarrow {}^7F_2$ transitions show intense emission peaks; the intensity ratio between these two peaks {(M.D)/(E.D)} varies significantly upon changes in the overall symmetry of the complex. In a centro-symmetric environment, for example in $Eu(DBM)_3H_2O$ (DBM = 1,3-diphenyl-1,3-dipropanedionate), the M.D peak dominates in the emission spectra; on the other hand, E.D peak prevails in $Eu(DBM)_3Phen$ (Phen = phenanthroline), due to the symmetry lowering.[19,20] Ultimately, the strong emission efficiencies, beyond 90% in certain media, stimulate a huge amount of studies on these complexes, making them highly promising candidates for novel luminescent materials for practical applications. The electronic transition from $^5D_1$ also leads to an emission signal, but up to now, this have been observed only at low temperature (< 150 K).

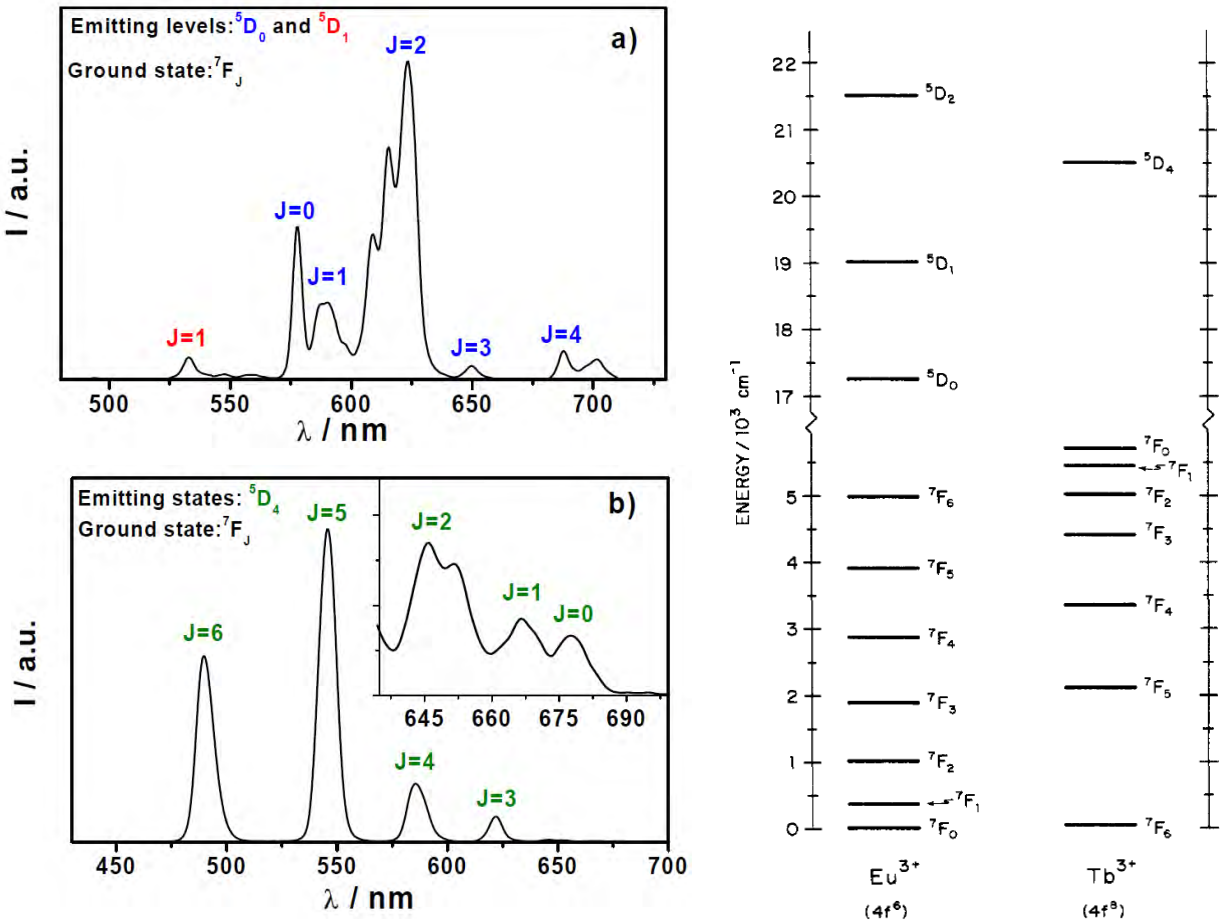

Figure 2.2.3 *Left: characteristic emission spectra of (a) Eu(III) and (b) Tb(III) ions. Right: the energy levels corresponding to the emission of Eu(III) and Tb(III) ions.*

The green Tb(III) ion is one of the strongest emitters among Ln(III) complexes;[2] its luminescent excited state lies 20,400 cm^{-1} above the ground state. In Tb(III) complexes, essentially all emission peaks originate from $^5D_4 \rightarrow {}^7F_J$ transitions, where J = 0,1,2,3,4,5 and 6 (**Figure 2.2.3**).[2,5] The most intense peak observed within the 540-555 nm spectral range comes from $^5D_4 \rightarrow {}^7F_5$ transition and other transitions show relative intensity in the following order $^5D_4 \rightarrow {}^7F_6 > {}^7F_4 > {}^7F_3 > {}^7F_2$. As similar to Eu(III), Tb(III) $^5D_4 \rightarrow {}^7F_6$, $^7F_4$, $^7F_2$ transitions are sensitive to the ligand nature; however, these are not "*hypersensitive*" and cannot explain the detailed nature of the ligand environment.[19,20] The Tb(III) emission is scarcely affected by aqueous coordination compared to Eu(III), and this is rationalized in terms of weak resonance between the high energy excited states of Tb(III) and vibronic oscillators. This property, along with the long emission lifetime of Tb(III) complexes (in the range of a few hundred ⊠s), makes it interesting as probe in bio-imaging applications.[8,9]

2.2.2 Europium(III) complexes

As mentioned earlier, Ln(III) ions show strong tendency to bind with organic ligands containing negatively charged oxygen due to their hard nature. Among others, β-diketone or acetylacetonate (acac) derivatives show exceptional affinity towards Eu(III) ions.[2] In addition, from the synthetic point of view, substituting any chromophores on the periphery of β-diketones is feasible through nucleophilic substitution reactions. Notably, these complexes are quite stable and show interesting luminescence properties in solution and in solid media. **Chart 2.2.1** shows the chemical structures of a set of acac based Eu(III) complexes whose luminescence properties have been thoroughly characterized in this work. Complexes **1-9** share a few common features like anionic coordination sphere, octacoordination and similar structural arrangements. This allows direct comparison of changes in the luminescence properties along the series, resulting from different electronic properties caused by the substituents on the acac ligand, and also by the different counter cations.

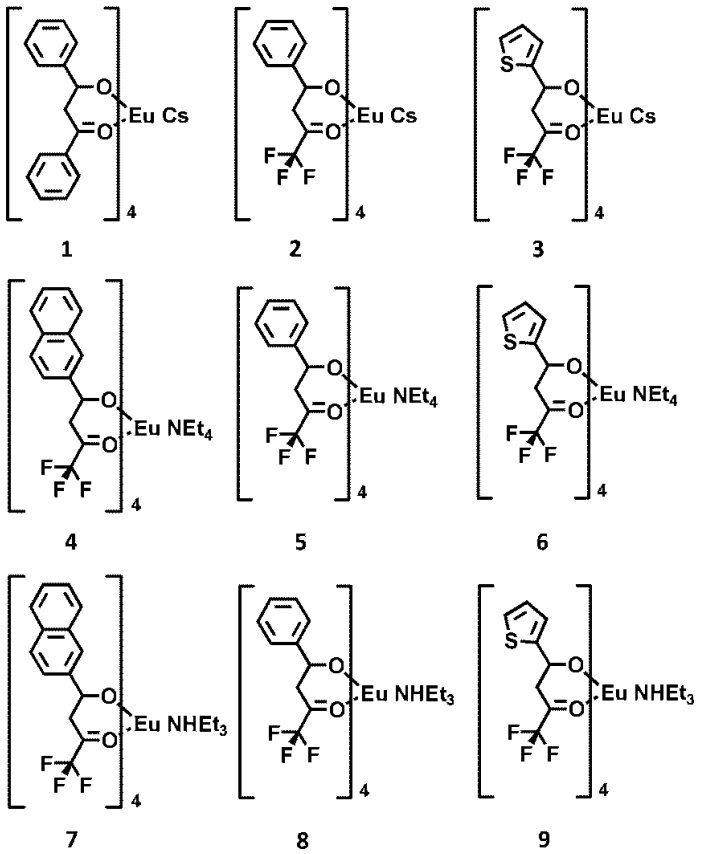

Chart 2.2.1 *Chemical structures of benzene, thiophene and naphthalene tethered acac-Eu(III) complexes.*

The photophysical characterization of **1-9** was carried out in solution and in the solid phase. Dichloromethane (DCM) is used as solvent for the Eu(III) complexes due to high solubility

and non-coordinating nature. The electronic absorption spectra of **1-9** show high intense peaks with $\varepsilon > 5 \times 10^4$ M^{-1} cm^{-1} in the UV region, corresponding to the π-π* transition of the attached organic chromophores. In particular, complexes **4** and **7** show strong absorption peaks compared to others due to naphthalene substituent. On the other hand, complexes **1-9** do not show any characteristic absorption signals of Eu(III) ions, due to the intrinsic low molar extinction coefficient values. Exciting **1-9** at their respective absorption maxima results in characteristic Eu(III) red emission; this suggests the occurrence of energy transfer (En.T) from the ligand moieties to the metal center. Further, no fluorescence from the attached chromophore was observed from the complexes, suggesting a highly efficient antenna effect. The excitation spectra were collected at the corresponding emission maxima of all the complexes and turned out to be matched with their respective optical absorption spectra, confirming the occurrence of En.T from the attached chromophores to the metal centers. In the present set of complexes, the En.T process most likely follows the Dexter mechanism, as is often evidenced by the triplet energy transfer from the ligands. The emission spectra of **1-9** show Eu(III) emission peaks corresponding to $^5D_0 \rightarrow {}^7F_J$ transitions.[4] Among the other peaks, the hypersensitive electric dipolar $^5D_0 \rightarrow {}^7F_2$ signal dominates the spectra; this indicates that these complexes are not in a centro-symmetric ligand environment.[2] Since all the complexes display similar properties, the absorption, excitation and emission spectra of **4-6** in DCM, are shown in **Figure 2.2.4** as an example to compare the effect of different substituents on the acac ligand. The emission quantum yields of **1-9** were calculated using air-equilibrated, $Ru(bpy)_3Cl_2$ water solution (Φ = 0.028) as reference. The excited state lifetime values were also measured using a time correlated single photon counting spectrometer and all the quantitative emission properties are collected in **Table 2.2.1**.

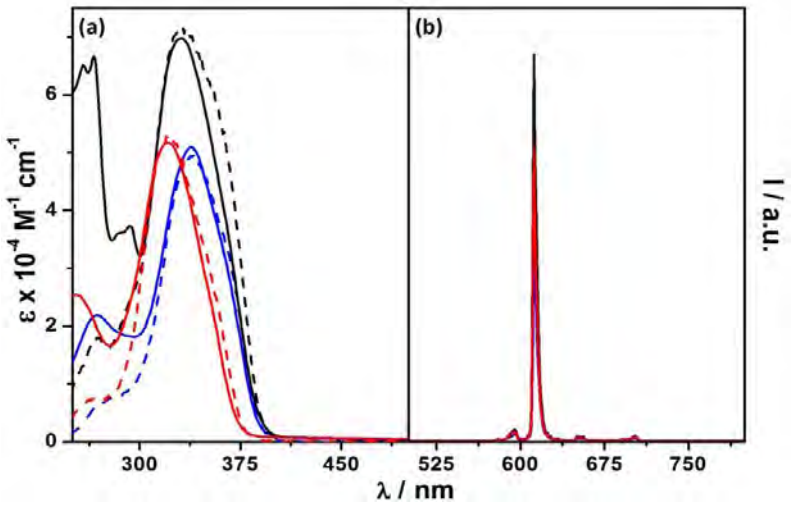

Figure 2.2.4 *(a) Electronic absorption (full lines), excitation (dashed lines) and (b) emission spectra of* ***4*** *(black),* ***5*** *(red) and* ***6*** *(blue) in DCM. The emission spectra of the complexes are collected upon exciting at the*

corresponding absorption maxima and the excitation spectra are collected from the corresponding emission maxima of the complexes.

Similar emission measurements were performed on all the complexes in the solid state, using discs made by grinding Eu(III) complex with potassium bromide (KBr). Qualitatively, emission and excitation spectra of **1-9** in the solid state display similar features to those in the solution phase. The absolute emission quantum efficiency of complexes is calculated using an integrating sphere fitted with the spectrofluorimeter. Compared to the solution phase, the quantum yield and lifetime values of the complexes in solid state are enhanced by a few orders of magnitude, which is a well known effect among Ln(III) complexes (**Table 2.2.1**). The absence of luminescence quenching vibronic interactions from the solvent molecules and other non-radiative decay paths is at the origin of the strong emission in the solid state. The complexes **1-9** show reasonable quantum efficiencies in the solid state (> 15%), which are somewhat higher than the same observed in solution. According to the different substituents like benzene, thiophene and naphthalene on acac ligands, these complexes can be divided into 3 sets, like **2-3**, **4-6** and **7-9**. Since the remaining parts of the complexes are invariably the same, their photoluminescence properties can be compared directly.

Table 2.2.1 *Luminescence data of the Eu(III) complexes **1-16** in DCM and in solid state.*

Compound	Solution phase (DCM)			Solid state		
s	λ_{max}	Φ	τ (ms)	λ_{max}	Φ	τ (ms)
1	614	<0.01	*a*	612	0.16	0.56
2	612	0.04	0.58	612	0.19	0.57
3	612	0.04	0.25	612	0.23	0.40
4	612	0.58	0.52	612	0.30	0.25
5	612	0.42	0.61	612	0.33	0.44
6	612	0.48	0.55	612	0.37	0.45
7	612	0.11	0.40	612	0.50	0.46
8	612	0.06	0.55	612	0.55	0.45
9	612	0.09	0.45	613	0.43	0.45
10	613	0.01	0.21	612	0.12	0.29
11	613	0.05	0.30	612	0.22	0.38
12	615	0.16	0.58	616	0.74	0.52
13	614	0.46	0.72	614	0.70	0.58
14	613	0.31	0.45	614	0.74	0.66
15	614	0.60	0.94	614	0.86	0.69
16	612	0.60	0.93	612	0.89	0.74

a – not measured due to the weak emission signal

By comparing the emission properties of **2** and **3**, no significant changes in the photoluminescence quantum yields (PLQY) are observed; but the former shows comparatively longer lifetime in solution and solid media. The same trend has been observed from **5**-**6** and **8**-**9** regardless of the counter ion effect. It should be noted that the molar extinction coefficient and the absorption maxima of benzene and thiophene substituted acac coordinated complexes are approximately the same. Therefore, quantitatively similar "*antenna effect*" is anticipated from the corresponding ligands. Hence, there is no surprise that the pairs **2**/**3**, **5**/**6**, and **8**/**9** show approximately the same PLQY (see **Table 2.2.1**). On the other hand, the comparatively lower lifetimes observed from the thiophene substituted complexes can be attributed to the presence of heteroatoms, which may stimulate faster decay processes.

Owing to the high molar extinction coefficient of naphthalene, strong antenna effect is anticipated in naphthalene acac-Eu(III) complexes. In fact, complexes **4** and **7** show high PLQY values compared to benzene and thiophene substituted acac-Eu(III) complexes. Thus, Eu(III) emission output can be enhanced by coordinating with strong chromophores. The lifetime values of **4** and **7** lie below the same of thiophene analogues. This would be the consequence of high π conjugation, which alters the position of frontier orbitals of ligand, and consequently leads to fast energy transfer process.

The series **1**-**9** also help to understand the effect of counter ion on the luminescence properties. To this purpose, the complexes are divided under 3 categories; namely, naphthalene bearing **4** and **7**, benzene containing **2**, **5** and **8**, and thiophene-acac attached **3**, **6** and **9**. It should be noted that, within the same group, e.g. between **4** and **7**, the coordination sphere remains invariably the same and only the counter cation changes, which allows a good comparison of luminescent properties between the complexes. The luminescence data from **Table 2.2.1** indicate that the complexes having cesium cation (Cs^+) as counter ion display lower emission efficiency. Similarly, by comparing complexes containing tetraethylammonium ion (NEt_4^+) and triethyl ammonium ion ($NHEt_3^+$), largely varying photoluminescence quantum yields in different media are evidenced. Since virtually no other factors can influence the emission properties of the complexes in the same set, it is assumed that the quantum yield and lifetime variations stem from different degree of counter ion interaction with the Eu(III) coordination sphere. The significantly low quantum yield of $NHEt_3^+$ containing **7**-**9** compared to the same of NEt_4^+ containing **4**-**6** in solution supports the above hypothesis. The N-H vibronic oscillators are considered to be one of the strong emission quenchers of Eu(III) complexes, due to the efficient resonance between Eu(III) excited states and N-H vibronic states (see above), assuming a close contact between $NHEt_3^+$ and Eu(III) coordination sphere. Upon photoexcitation, Eu(III) excited states will be populated through

antenna effect and, subsequently, the excited energy will be transferred to the N-H vibronic states of the counter ion. Hence, the overall process can result in reduced luminescence from the Eu(III) center. By contrast, in the case of NEt_4^+, though C-H bonds also can behave similar to N-H bonds, the low energy gap between the vibronic states of the former leads to reduced energy resonance interactions. This is in line with the strong emission properties of complexes **4**-**6** compared to that of **7**-**9** in solution. In the solid state, the dynamic interactions between the coordination sphere and the counterion are not possible; hence the quenching effects are absent. This is supported by the similar lifetime values of **4**-**9** in the solid state. However, the quantum yield values show drastic changes, but this remains unclear due to the lack of detailed X-ray crystal structures of the complexes under study.[21]

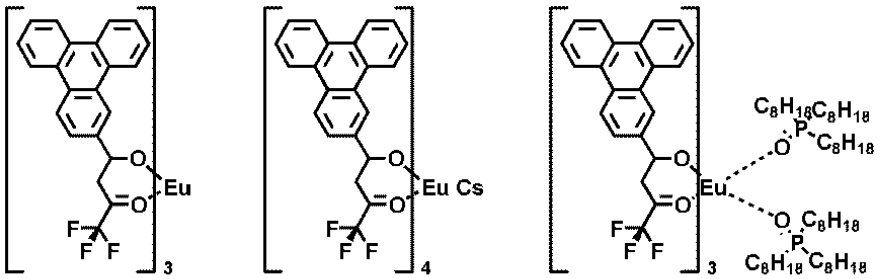

10 **11** **12**

Chart 2.2.2 *Chemical structures of triphenylene substituted acac-Eu(III) complexes.*

Chart 2.2.2 displays the triphenylene substituted acac-Eu(III) complexes **10**-**12**, which are structurally similar to the above mentioned compounds. The complexes **10** and **12** are neutral, and hexa and octa coordinated respectively, whereas **11** contains negatively charged coordination sphere with Cs counter cation. The absorption spectra of **10**-**12** show the maxima around 350 nm, corresponding to triphenylene π-π* transition, and the molar extinction coefficient values of **10** and **12** are approximately 7 x 10^4 M^{-1} cm^{-1}. Undoubtedly, **11** should have higher **ε** value due to the presence an additional chromophoric ligand. The emission spectra of **10**-**12** collected by exciting the triphenylene absorption maximum display the characteristic Eu(III) peaks, centered at 613 nm. Importantly, all the 3 complexes show an additional broad emission band around 450 nm (**Figure 2.2.5**), which is attributed to the fluorescence of triphenylene unit. The same is observed in the solid state emission spectra. The incomplete energy transfer from the ligand to the Eu(III) center or the presence of residual uncomplexed ligands in the bulk should be the origin of the fluorescence signal. Other emission properties of **10**-**12** are mostly similar to the previously discussed complexes and are listed in **Table 2.2.1**.

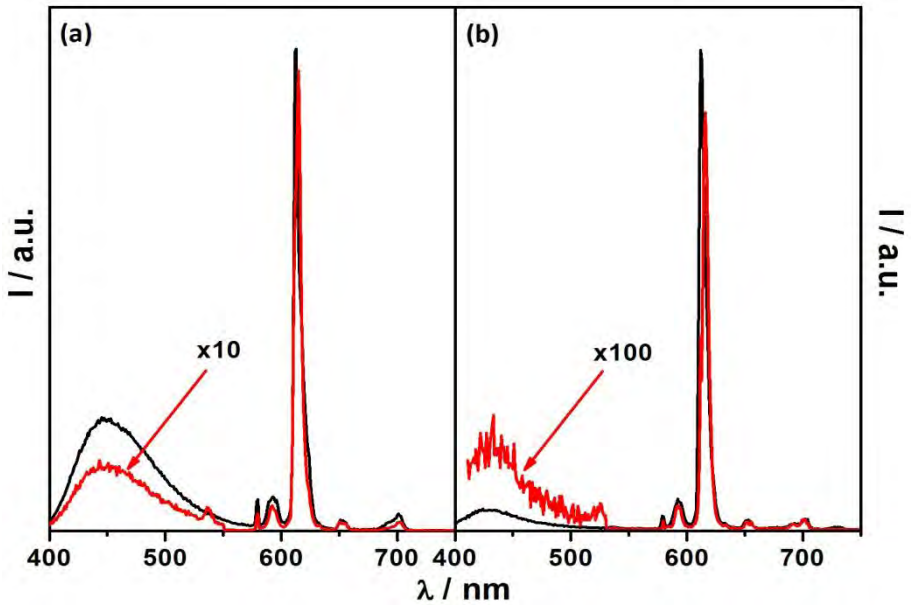

Figure 2.2.5 *Emission spectra (λ_{ex} = 360 nm) of* ***10*** *(black) and* ***12*** *(red) (a) in DCM and (b) in solid state.*

The PLQY and lifetime values of hexa coordinated **10** are lower than those of **11** and **12**. As mentioned before, the hydration of Eu(III) ion to complete the coordination sphere is a possible reason, which would quench the luminescence properties through O-H vibronic oscillators. Making the same comparison for **11** and **12** indicates that the octa coordination somehow increases the emission efficiency; however, the interaction of Cs ion with the coordination sphere leads to reduced quantum efficiency and lifetime (*vide supra*). The coordination with phosphine oxide makes the difference in **12** relative to **10** and **11**, and this drastically enhances the luminescence properties. The bulky ancillary phosphine oxide ligands protect the coordination sphere from luminescence quenching environmental effects, such as solvent or other nucleophilic attacks. The comparatively strong π accepting ability of phosphine oxide may increase the charge density on the metal ion; consequently, this would cause strong acac coordination, and an increase of the total rigidity of the complex. Thus, the vibrational relaxation of the excited state energy is minimal with phosphine oxide coordination. Altogether, **12** shows a lifetime longer than 0.50 ms in both solution and solid media, and ca. 70% quantum yield in the solid state, which supports the above concepts.

The observed strong emission from the phosphine oxide coordinated Eu(III) complex **12,** prompted the design and synthesis of analogues with different acac based Eu(III) complex (**13-16**, **Chart 2.2.3**). The complexes **13** and **14** contain thiophene and trifluoromethyl groups at the β position of the acac, with different phosphine oxide derivatives. On the other hand, **15** and **16** hold two trifluoromethyl groups in acac, aimed to reduce the vibrational relaxation of the excited energy through -CH bonds.[12,22] The spectral positions of absorption and emission features of **13**

and **14** are apparently the same. This indicates that the coordination of different phosphine oxide derivatives with Eu(III) does not perturb the electronic properties of the acac ligands. However, the effect of different structural features of the phosphine derivatives can be discerned from the quantitative analysis of luminescence properties (**Table 2.2.1**). For instance, the PLQY and lifetime values of **13** is higher than that of **14** in solution, probably due to the reduced steric effects in the latter, which may cause luminescence quenching solvent interactions. This is confirmed by the similar emission efficiency and lifetime of both complexes in the solid state, due to the absence of quenching effects from solvent molecules.

Further, placing trifluoromethyl group in acac instead of thiophene, significantly alters the absorption and emission properties of **15** and **16**. The absence of π-conjugated chromophores in these complexes reduces the molar extinction coefficient (ε = 3 x 10^4 M^{-1} cm^{-1}) to the half of **13** and also blue shifts the absorption maxima. Virtually, the hypersensitive peak dominates the emission spectra of **15** and **16** upon exciting at the absorption maximum, showing the absence of centro-symmetric geometry.

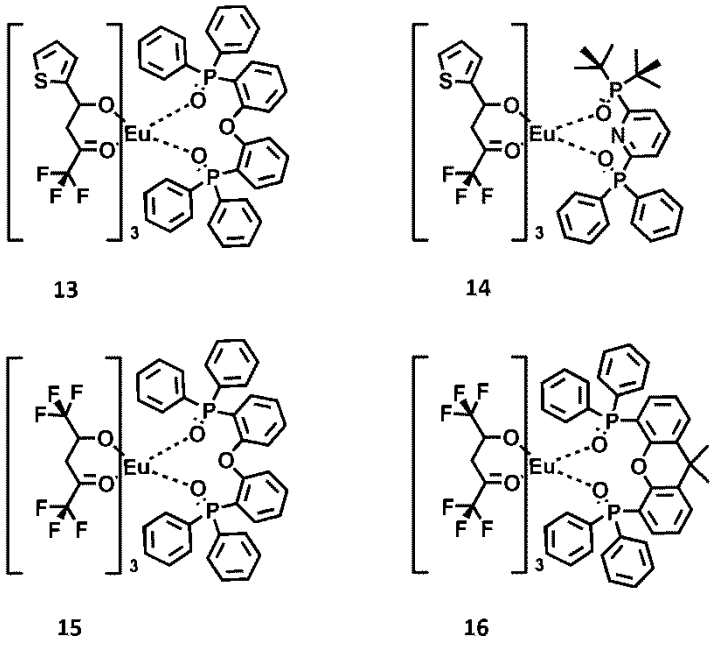

Chart 2.2.3 *Chemical structure of phosphine oxide coordinated acac-Eu(III) complexes.*

The PLQY and lifetime values of **15** and **16** are surprisingly higher than any other complex listed in **Table 2.2.1**. Hence, it is clear that the substitution of trifluoromethyl groups helps reducing the internal quenching effects and consequently increases the PLQY and lifetime of Eu(III) ion drastically. It should be noted that **15** and **16** behave similarly, though different phosphine derivatives have been used; thus, it is clear that the bulky structural feature of the

neutral phosphine oxide derivatives is far more important in dictating the emission properties than the intrinsic electronic properties.

2.2.3 Terbium(III) complexes

Tb(III) emitters are renowned in the field of luminescent biodiagnostics.[8,9] The maximum of Tb(III) emission lies in the green spectral region, due to the high band gap value (20,400 cm^{-1}), Tb(III) emitters are scarcely sensitive to the O-H, N-H or C-H vibronic oscillators.[2,12] This can make them strongly emissive even in aqueous medium. This factor and the long lifetime make Tb(III) complexes particularly suitable for *in-vivo* imaging studies. Unlike Eu(III), complexes of acac-Tb(III) are not stable and also not emissive. This may be due to the position of acac's triplet state which may lie at lower energy with respect to the excited emissive states of Tb(III); thus, energy transfer processes are weak and consequently lead to weak emission. This problem is overtaken by using pyrazolone derivatives as ligands to coordinate Tb(III) ions. The studied pyrazolane complexes are shown in **Chart 2.2.4**.

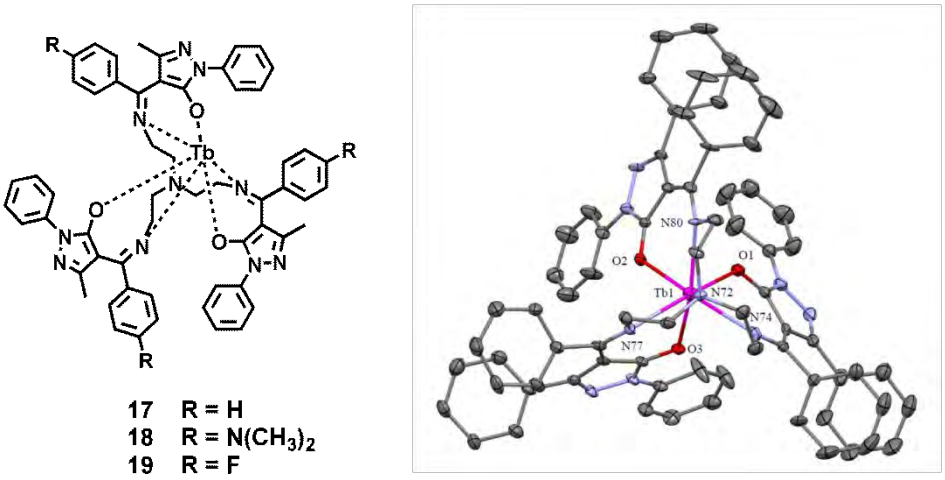

Chart 2.2.4 *Chemical structure of pyrazolone derivatives based Tb(III) complexes (right) and the X-ray structure of analogous Tb(III) complex, where a benzene ring is substituted at 3-pyrazolone position.*

The elemental analysis and IR spectra (broad peak centered at 3430 cm^{-1}) of these Tb(III) complexes evidence the presence of water molecules in the coordination sphere.[23] It should be noted that Tb(III) holds only 6 coordination bonds, and the peculiar "tripod" like structure hampers further coordination of other bulky ligands. The X-ray model structure of an analogous compound is shown in **Chart 2.2.4**.

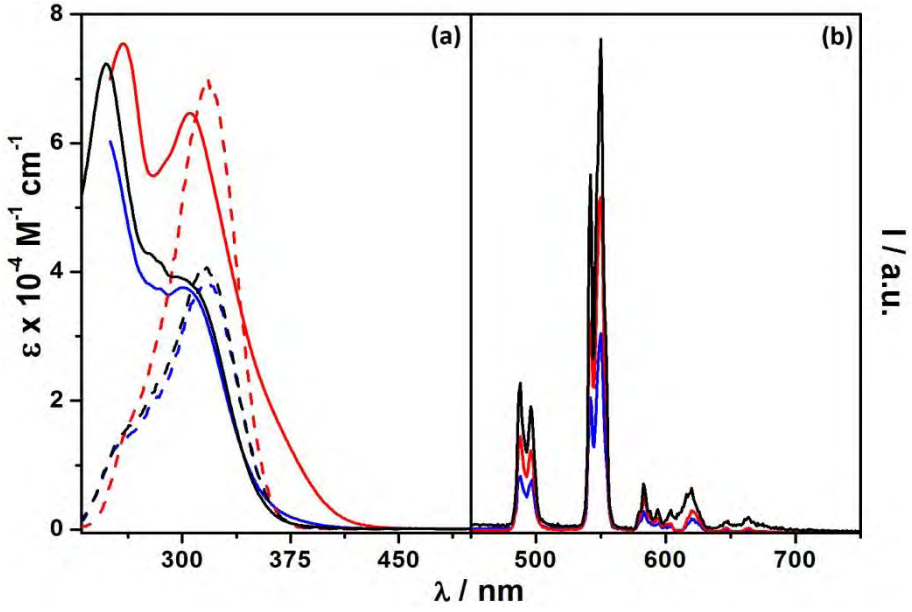

Figure 2.2.6 *(a) electronic absorption (full lines), excitation (dashed lines) and (b) emission spectra of* ***17*** *(black),* ***18*** *(red) and* ***19*** *(blue) in DCM. The emission spectra of the complexes are collected upon exciting at the corresponding absorption maxima. The excitation spectra are collected from the corresponding emission maxima of the complexes.*

The absorption spectra of the complexes **17**-**19** in DCM display two major bands with maxima located at ca.250 and 310 nm, corresponding to the singlet-singlet transitions of the ligand.[23] Notably, the band intensity at 310 nm varies significantly along **17**-**19**, suggesting the perturbation in electronic levels due to the substituents at the benzene ring (**Figure 2.2.6**). On the other hand, the intense peak at 250 nm remains the same in all the cases with molar extinction coefficient value of ca. 7 x 10^4 M^{-1} cm^{-1}. Upon exciting **17**-**19** at 300 nm, the characteristic Tb(III) emission peak with maximum at 549 nm is observed with PLQY of 0.09%, 0.17% and 0.04% respectively (**Figure 2.2.6**). Though -OH vibronic oscillators weakly resonate with Tb(III) emissive states, the presence of water molecules in the Tb(III) coordination sphere should be the main reason for such low emission efficiencies. The effect of different substituents in **17**-**19** can be discerned from the solid state emission measurements. The quantitative analysis on **17**, **18** and **19** shows PLQY of 14%, 6% and 27% and lifetime of 0.6, 0.5 and 0.8 ms respectively. This trend suggests that the para- position of the benzene ring, located in secondary ketimine carbon, is susceptible for electron withdrawing and donating effects. The reduced emission efficiency and lifetime of **18** compared to **17** implies the reduced energy transfer efficiency from the ligand to the metal ion, possibly due to the electron donation effects. This is quite reasonable, if the para position of the benzene ring plays a key role in deciding the position of HOMO orbitals. In fact, this is in line with observed PLQY and lifetime of **19**, which are significantly higher than its analogues. The highly electronegative -F would reduce the energy of the HOMO, thereby

increasing the band gap. This ensures the efficient energy transfer from the excited ligand orbitals to the metal center, yielding strong emission properties. To sum up, the band gap of pyrazolone is finely tuned by substituting electron donating and withdrawing residues at the benzene ring located in secondary ketimine carbon, which in turn affects the emission properties of the Tb(III) metal ion.

2.2.4 Summary

A series of Eu(III) and Tb(III) complexes have been analyzed and a library of photophysical data was collected. From the photophysical characterization, it can be deduced that the emission properties of negatively charged Eu(III) coordination spheres are susceptible to interactions with the counterions in solution. Apparently, the same effect is negligible in the solid state. The peculiar coordination environment of phosphine oxide derivatives results in enhanced emission properties, due to the increased steric effect and structural rigidity. Substitution of fluoride enriched acac ligands together with phosphine oxide complexation of Eu(III) results in significantly high PLQY and longer lifetime values. As far as Tb(III) complexes are concerned, a way to alter the band gap of the pyrazolone ligand has been unveiled and this may open the way to design new complexes with enhanced emission properties. A few selected, strongly emissive Eu(III) and Tb(III) complexes can be utilized to probe with carbon nanostructures and prepare luminescent hybrids.

2.3 Transition metals based emitters

The establishment of the area of luminescent transition metal complexes dates back to 1960's with the observation of red orange emission from $[Ru(bpy)_3]^{2+}$. Thereafter, an intense research has been dedicated to develop analogous luminescent complexes based on different transition metal ions. In general, the interaction of ligands with transition metals splits the d orbitals into stabilized and destabilized orbitals with an energy difference (Δ_o). The Δ_o between two sets of orbitals depends on (i) the ionic charge: the higher the oxidation state, the higher the Δ_o splitting; (ii) the spatial extensions of the d orbitals: Δ_o is smallest for 3d metals and progressively increases with 4d and 5d metals; (iii) the field strength exerted by the ligands, following the so-called spectrochemical series. Considering the photophysical properties of the polypyridine complexes of Fe(II), Ru(II) and Os(II) metal ions,[24]

a) Fe^{II}, $3d^6$ configuration: as the Δ_o splitting is very small, hence the lowest-lying excited state is ^{1}MC in nature (i.e., centered on e_g metal orbitals) and, therefore, not emissive.

b) Ru^{II}, $4d^6$ configuration: the Δ_o splitting is increased and the lowest (emissive) excited state is a metal-to-ligand charge transfer triplet (^{3}MLCT), relatively close to ^{3}MC states that can be thermally populated and open a competitive radiationless deactivation pathway deactivation pathway to either the ground state or to degradation products; accordingly, Ru^{II} complexes substantially increase the PLQY by decreasing temperature.

c) Os^{II}, $5d^6$ configuration: the Δ_o splitting is considerable and the ^{3}MC states are usually too high to affect emission properties, but the emissive ^{3}MLCT excited state has lower energy compared to Ru^{II} analogues (emission bands typically peaking in the red/infrared edge of the spectrum) and this favors radiationless pathways thanks to the "energy gap law"; accordingly, PLQYs of these complexes are typically low, often below 1–2%.

Schematic representation of ^{3}MLCT and ^{3}MC states Fe(II), Ru(II) and Os(II) poly pyridine complexes are depicted in **Figure 2.3.1**.

A few transition metal complexes like $[Ru(N\text{^}N)_3]^{2+}$, $[Cu(P\text{^}N)_2]^{+}$, $[Ir(C\text{^}N)_2]$ etc. are particularly unique due to the features like (i) ease of preparation; (ii) reversible electrochemical behavior; (iii) visible light absorption; (iv) intense and tunable emission; (v) long living excited states. Owing to these advantages, transition metal complexes acquired great deal of interest in recent years, in the fields of OLED (Organic light emitting diode), LEC (light emitting electrochemical cell) and DSSC (dye sensitized solar cell).

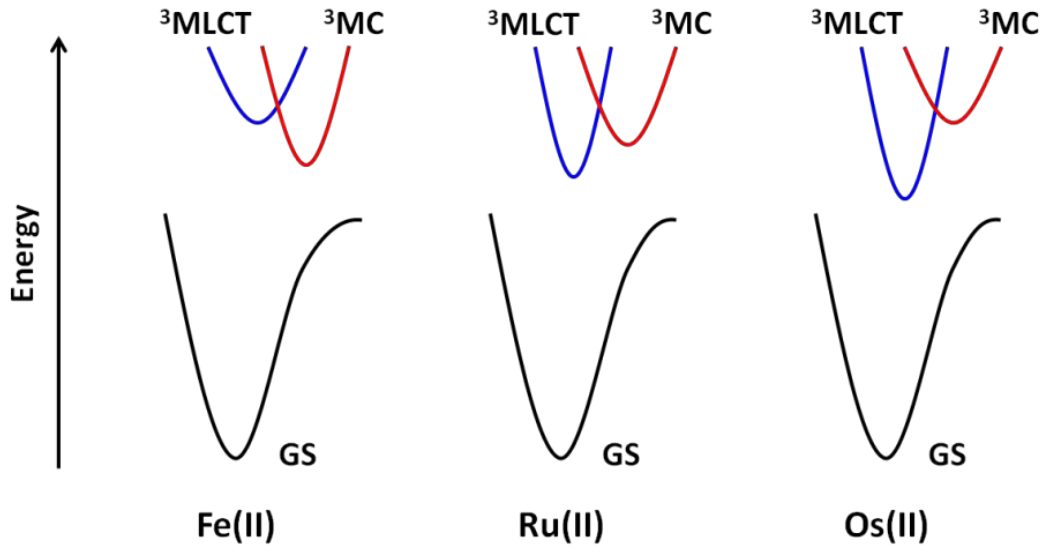

Figure 2.3.1 *Comparison of relative positions of MLCT, MC and ground state (GS) potential curves of Fe(II), Ru(II) and Os(II) polypyridine complexes.*

2.3.1 Luminescent Copper(I) complexes

$[Ru(bpy)_3]^{2+}$, where bpy is 2,2'-bipyridine, is one of the most studied transition metal complexes.[3] This compound shows many attractive properties such as, high stability, intense visible absorption and emission, well defined redox chemistry, and microsecond lifetime.[25] Though, this has been implemented in a few practical luminescent devices, high cost, low abundance and environmental aspects are potential drawbacks that stimulate the search for alternatives. Copper(I) transition metal complexes are gaining an increasing attention through the development of new synthetic strategies and a deeper insight into the rationalization of their photophysical properties.[26] Indeed, $[Cu(N\hat{}N)_2]^+$, where N^N stands for diimine, complexes are the only first row transition metal complexes with excited state properties comparable to $[Ru(bpy)_3]^{2+}$. These complexes absorb in the visible region (350 – 650 nm) with relatively high molar extinction coefficient values (above 10^3 M^{-1}). Upon light excitation, $[Cu(N\hat{}N)_2]^+$ complexes undergo dynamic symmetry change from tetrahedral to square planar, due to the oxidation of Cu(I) to Cu(II).[27] This opens the way to nucleophilic attack of solvent or other electron rich molecules and leads to non-radiative decay to the ground state. Complexes with phenanthroline ligands that contain bulky groups at 2,9-positons show sizable emission properties with long lifetime values in solution.[28] Importantly, copper is less toxic, economical and environment friendly than ruthenium.

In recent years, heteroleptic $[Cu(N\hat{}N)(P\hat{}P)]^+$ type complexes, where P^P indicates bisphosphine ligand, has partially replaced the conventional $[Cu(N\hat{}N)_2]^+$ complexes, by showing remarkably enhanced emission properties and moderate stability, thanks to the electron withdrawing and stabilizing effects of phosphine ligands.[29,30] Further, owing to the strong π accepting nature of phosphine ligands, the efficiency of back electron donation from Cu(I) to N^N ligands decreases significantly. This is quite evident from the increased oxidation potential of the Cu(I) in cyclic voltammetry experiments.[29] At the same time, this increases the energy gap between the excited emissive levels and the ground state, eventually resulting in enhanced emission according to the *energy gap law*. Recently, $[Cu(P\hat{}N)(P\hat{}P)]^+$ type heteroleptic complexes are receiving increasing interest, thanks to their emission properties. For example, amidophosphine (P^N) derivatives and phosphine chelating groups (P^P), $[Cu(P\hat{}N)(P\hat{}P)]^+$ can give rise to a heteroleptic complex showing PLQY of 0.7 in benzene and 10-20 μs lifetime, similar to popular Ir(III) cyclometalated complexes.[31] Taking motivations from this and to promote Cu(I) complexes to the next level, a novel family of complexes, $[Cu_2(P\hat{}N)_3X]^+$, have been synthesized and their photophysical properties fully characterized. The derivatives of amido phosphines along

with one ancillary ligand (X) are used to prepare the binuclear Cu(I) complexes **20**-**24**. The ancillary ligands in **20**-**24** are acetonitrile, benzonitrile, 1-cyano-4-nitrobenzene, 1-cyano-4(N,N')dimethylaminobenzene and phosphine oxide, respectively. The chemical structures of **20**-**24** and the corresponding ligands are shown in **Chart 2.3.1** and **2.3.2** respectively. The purity and the depicted structures are confirmed by ^{1}H-NMR, ^{31}P-NMR and X-ray analyses.

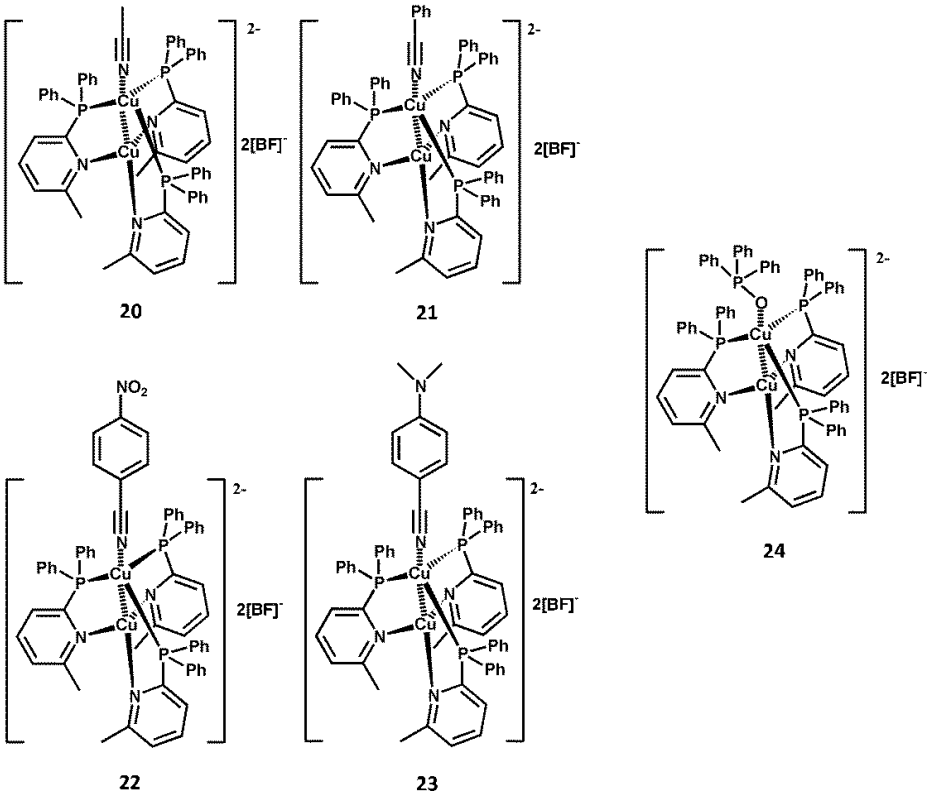

Chart 2.3.1 *Chemical structure of amido phosphine coordinated $[Cu_2(P\hat{}N)_3X]^+$ type complexes.*

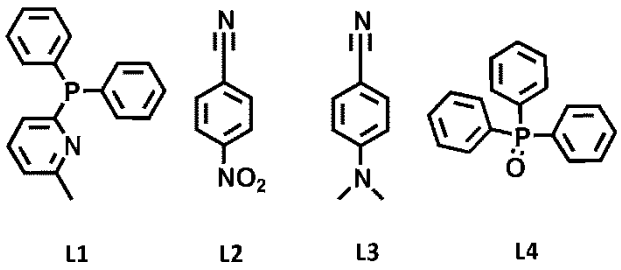

Chart 2.3.2 *Chemical structure of amido phosphine and other anciliary ligands used in **20**-**24** complexes.*

The electronic absorption spectra of complexes **20**-**24** and of the related ligands in CH_2Cl_2 are shown in **Figure 2.3.1**. The spectral shapes of **20**, **21** and **24** are similar, whereas **22** and **23** show moderate changes due to the additional absorption features of ancillary chromophoric ligands L2 and L3. By comparison with the spectra of the ligands (**Figure 2.3.1**), the intense UV

bands of **20-24** up to about 330 nm are attributable to ligand centered π–π* transition, whereas the weak, broad tails, in the range 330-380 nm, are tentatively assigned to MLCT transitions.[25,27] Such bands are significantly blue-shifted compared to other phosphorus (P) and nitrogen (N) based heteroleptic Cu(I) complexes.[24,29,32,33] This may be due to the effective coordination and electron withdrawing properties of P ligands, which stabilize the HOMO of complexes and consequently increases the energy gap with the LUMO.[27,29,34] At room temperature, all the complexes exhibit featureless, weak, bluish-green emission at any excitation wavelength in aerated CH_2Cl_2 (**Figure 2.3.2**). The PLQY and excited state lifetime values are gathered in **Table 2.3.1**; upon deoxygenating the samples, such values are substantially increased and are comparable with some other heteroleptic (N- and P-) Cu(I) complexes reported in the literature.[24] In addition, the peculiar ligand structure assures tight packing of the complexes in the ground state and also possibly in the excited state; in fact, **20-24** exhibit exceptional stability over many days in CH_2Cl_2 solution.

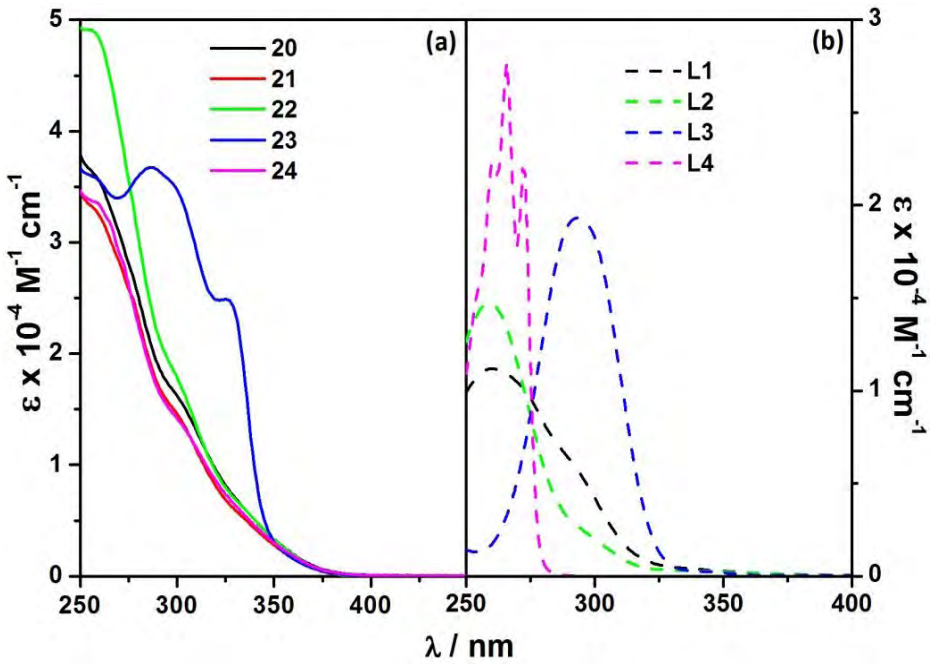

Figure 2.3.1 *Electronic absorption spectra of (a) complexes **20-24** (black, red, green, blue, and magenta, respectively) and (b) ligands L1 (black), L2 (green), L3 (blue) and L4 (magenta) in CH_2Cl_2.*

In line with previously reported Cu(I) luminescent complexes, the observed emission can be attributed to MLCT state(s), and this is supported by density functional theory calculations carried out on similar systems.[35] The strong sensitivity of the emission intensity to the oxygen presence, the μs-scale lifetime and the large shift between absorption and excitation maxima (**Figure 2.3.2b**) suggest a triplet nature for the emissive state.[25,27] Furthermore, the bi-exponential character of the luminescence decay (except for **23**, **Figure 2.3.3**) and the extended emission tail

at longer wavelengths suggest the participation of multiple CT levels to the emission profiles. The long lifetime of the complexes **20**, **21**, **23** and **24** with high relative amplitude (**Table 2.3.1**) advocates the dominant contribution of a ^{3}MLCT state to the emission, although the trend is reversed in **22**. The absence of shoulders or well resolved emission bands suggests a minimal energy gap between non-degenerate MLCT levels. As a result, at room temperature, such levels are thermally equilibrated and this can explain the broad emission bands observed. This concept is corroborated by luminescence studies carried out at 77K.

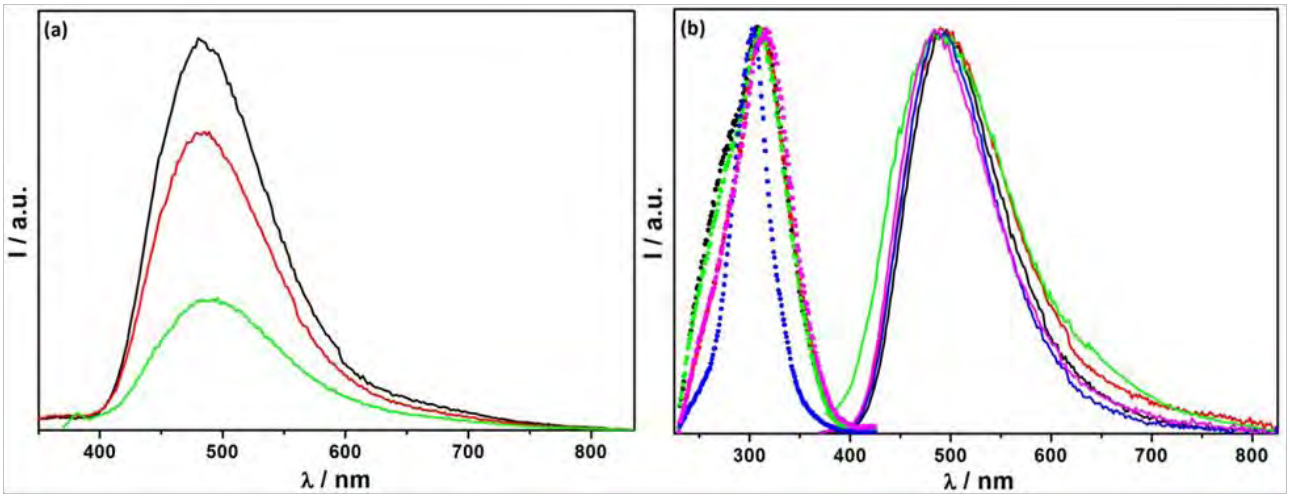

Figure 2.3.2 *(a) Emission spectra of **20** upon exciting at 270 nm (black), 305 nm (red) and 340 nm (green) in CH_2Cl_2; (b) Excitation (dotted lines) and emission (full lines) spectra of complexes **1**-**5** (black, red, green, blue and magenta respectively, uncorrected) in degassed CH_2Cl_2. Emission spectra are recorded upon exciting **1** and **3** at 320 nm, and **2**, **4** and **5** at 340 nm. Excitation spectra are collected at the respective emission maximum of each complex.*

Compared to the solution phase, the emission of **20**-**24** at 77 K is very intense and hypsochromically shifted of about 20 nm (**Figure 2.3.4**). Moreover, all the complexes show monoexponential and substantially longer lifetimes (**Table 2.3.1**). It is worth noticing that this behavior contrasts with what often found for both homoleptic [36] and heteroleptic[32,37,38] Cu(I) complexes in which lowering of the temperature implies (i) red-shift of emission maxima, (ii) decrease of emission intensity, (iii) prolongation of the lifetime. This frequent pattern is interpreted with the so-called two state model which implies an interplay between thermally equilibrated singlet and triplet MLCT levels.[27] The featureless, unresolved emission bands and monoexponential excited state lifetimes of the order of a few tens of μs also rule out a relevant role of intraligand charge transfer (ILCT) states or micro-environmental effects in the frozen state, as suggested elsewhere for heteroleptic (N- and P-) Cu(I) complexes.[39-41]

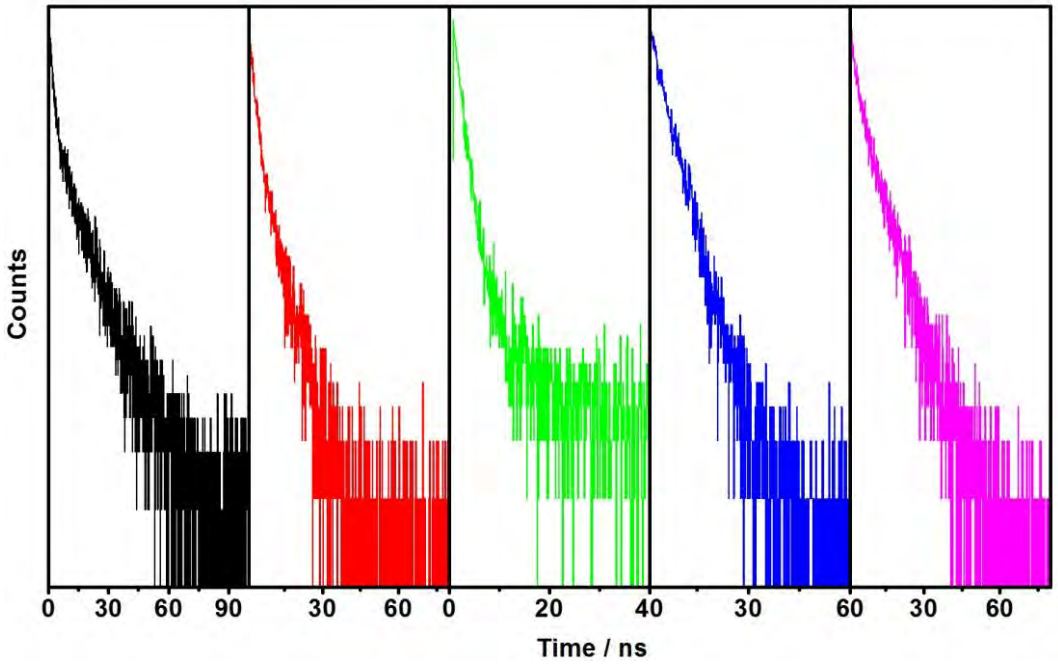

Figure 2.3.3 *Emission decay curves of* ***20-24*** *(black, red, green, blue and magenta respectively) excited at 373 nm in* CH_2Cl_2.

Table 2.3.1 *Luminescence data of complexes* ***20-24*** *in* CH_2Cl_2 *at 298 K, at 77K, and in solid state.*

	CH_2Cl_2 solution (298 K)						Rigid matrix (77 K)			Solid state (298 K)			
	aerated			deaerated									
	Φ x 10^{-3}	τ (μs)[a]	λ_{max} (nm)	Φ	τ (μs)[a]	FWHM (nm)	λ_{max} (nm)	τ (μs)	FWHM (nm)	λ_{max} (nm)	Φ	τ (μs)	FWHM (nm)
20	2.3	0.32 (93); 0.03 (7)	490	0.028	11.7 (71); 1.5 (29)	109	470	35	67.6	502	0.46	28 (50); 7 (50)	109
21	6.2	0.43 (88); 0.9 (12)	490	0.032	7.5 (63); 2 (37)	124	465	42	69.8	479	0.21	32 (71); 3 (29)	102
22	3.8	0.33 (91); 0.04 (9)	489	0.012	7 (23); 1.7 (77)	139	478	43	83.6	*b*	*b*	*b*	*b*
23	2.1	0.22 (78); 0.004 (22)	488	0.035	5.7 (100)	107	477	98	102.2	477	0.06	38 (73); 3.5 (27)	131
24	2.6	0.39 (87); 0.11 (13)	486	0.018	9 (85); 2 (15)	109	465	45	70.1	465	0.20	19 (77); 4 (23)	95

[a] *The values in brackets are the relative weight of each component of the emission decay.*
[b] *Complex* ***22*** *shows multiple emission bands in the solid state (see text).*

On the other hand, the trend observed for **20-24** is that found for some "classic" MLCT luminescent transition metal complexes (e.g. Ru(II)-polypyridines), where the emission blue shift at low temperature is attributed to (a) the lack of solvent reorganization in the frozen matrix and consequent destabilization of the emissive charge transfer state and (b) reduced non-radiative

pathways according to the energy gap law.[3,42] Notably, for a few Cu(I) complexes, equipped with very bulky phenanthroline ligands, a blue-shift with lowering temperature is observed, which is the consequence of a tightly locked tetrahedral structure of the complexes in the excited state.[28,43-45]

In the present set of Cu(I) complexes, similarly, the efficient coordination of P and N as well as the rigid structure assure minimal distortion upon irradiation in CH_2Cl_2, which removes the degeneracy of low lying MLCT states.[3,37] Consequently, at room temperature, non-degenerate MLCT levels likely establish a complex thermal equilibrium and simultaneously contribute to the luminescence of the complexes. **20-24** exhibit wide spectra at room temperature (FWHM in the range 100-140 nm) and, for **20-22** and **24**, the observed dual lifetime suggests the participation of ^{1}MLCT and ^{3}MLCT levels.[3,31,36,38,40] Lifetimes are always longer than 1 μs in deoxygenated solutions and this might appear unusual for spin permitted ^{1}MLCT deactivations. However, ^{1}MLCT states may not be pure singlets due to spin orbit coupling induced by the Cu(I) ion[46] and, moreover, the establishment of excited state equilibria may substantially elongate excited state lifetimes, depending on specific deactivation rate constants of the equilibrated levels.[47,48] As compared to the solution case, the excited state structural deformation of the complexes in the rigid matrix is further restricted; hence, negligible perturbation of the MLCT states is expected. This is evidenced by the monoexponential and comparatively longer lifetime values (μs range), as well as from the much smaller FWHM of the emission bands (**Table 2.3.1**).

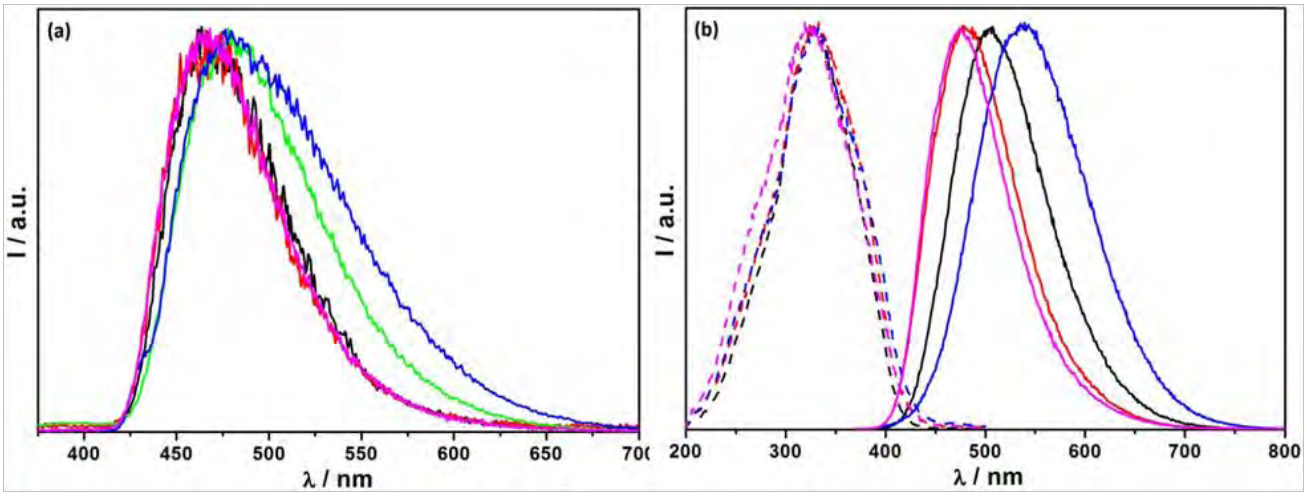

Figure 2.3.4 *(a) Emission spectra of complexes **20-24** (black, red, green, blue and magenta respectively) upon exciting at 330 nm in CH_2Cl_2 rigid matrix at 77 K (uncorrected profiles); (b) Excitation (dashed lines) and emission (full lines, λ_{ex} = 340 nm) spectra of complexes **20**, **21**, **23** and **24** (black, red, blue and magenta respectively, uncorrected) in the solid state. Excitation spectra are recorded at the emission maximum of each complex.*

Interestingly, complex **23** shows virtually the same emission band profile in solution and rigid matrix (FWHM - 107 nm at rt. and 102 at 77 K), suggesting emission from a distinct excited state and indicating that minimal changes of the coordination environment may cause substantial variation of the photophysical properties. The effect of the ancillary ligands on the HOMO/LUMO gap appears to be negligible[35] and this is reflected by the similar emission maxima of complexes both in CH_2Cl_2 and in rigid matrix. However, the PLQY and lifetime values are different along the series.

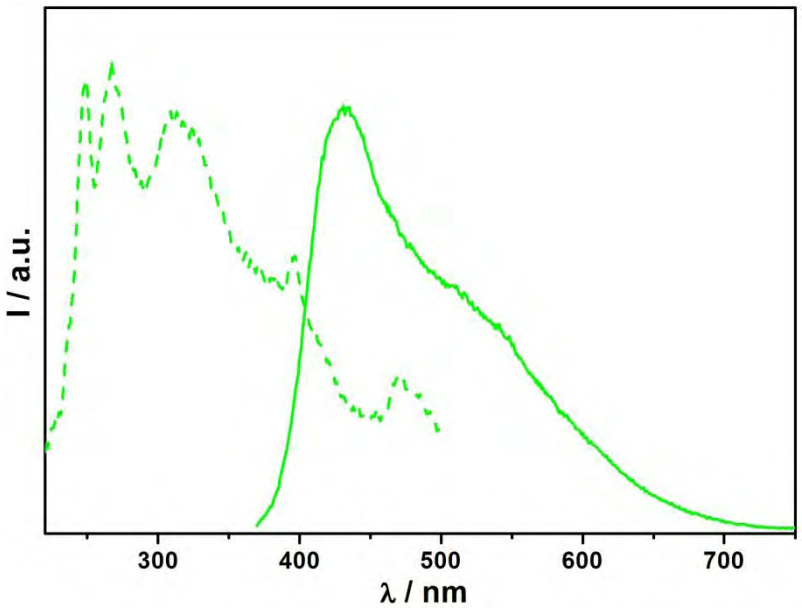

Figure 2.3.5 *Excitation (dashed line) and emission (full line, λ_{ex} = 340 nm) spectra of **22** in solid state. The excitation spectrum was collected at the respective emission maximum of the the complex.*

This trend is further confirmed by the excitation and emission spectra in the solid state (KBr matrix, **Figure 2.3.4**). The excitation spectra of **20**, **21**, **23** and **24** are superimposed on each other, irrespective of the ancillary ligand. This shows a virtually constant energy gap between the frontier orbitals, as also suggested by theoretical studies.[35] On the other hand, these complexes exhibit different emission maxima and, notably, PLQY values as high as 0.46, a remarkable finding for Cu(I) complexes.[24,25] Excited state lifetimes are substantially longer than in CH_2Cl_2 solution but still biexponential (**Table 2.3.1**). On the other hand, **22** shows different emission bands as a function of the excitation wavelength, and the excitation spectrum did not match the absorption profile (**Figure 2.3.5)**.

2.3.2 Summary

The newly prepared amidophosphine based Cu(I) complexes **20**-**24** are highly stable in solutions and show characteristic MLCT absorption and bluish-green emission with maxima around 500

nm. The oxygen sensitivity to the emission, high Stokes shift and longer lifetime of the complexes corroborate the MLCT nature of the emitting excited state. The solid state luminescence measurements evidence the strong emission properties of the complexes with PLQY reaching the maximum up to 46%, and 38 μs lifetime. The extraordinary stability with strong luminescent properties of this type of complexes can pave the way to design similar compounds, and advantage will be taken on these complexes to probe with carbon nano structures.

2.4 References

1. J. R. Lakowicz, *Principles of fluorescence spectroscopy - Third edition*, Springer, New York, 2006.
2. D. Parker and J. A. G. Williams, *J. Chem. Soc.-Dalton Trans.*, **1996**, 3613-3628.
3. T. J. Meyer, *Pure Appl. Chem.*, **1986**, *58*, 1193-1206.
4. J.-C. G. Bünzli and C. Piguet, *Chem. Soc. Rev.*, **2005**, *34*, 1048-1048.
5. J.-C. G. Bünzli, *Acc. Chem. Res.*, **2006**, *39*, 53-61.
6. L. Armelao, S. Quici, F. Barigelletti, G. Accorsi, G. Bottaro, M. Cavazzini and E. Tondello, *Coord. Chem. Rev.*, **2010**, *254*, 487-505.
7. L. D. Carlos, R. A. S. Ferreira, V. D. Bermudez and S. J. L. Ribeiro, *Adv. Mater.*, **2009**, *21*, 509-534.
8. J. C. G. Bunzli, *Chem. Rev.*, **2010**, *110*, 2729-2755.
9. F. S. Richardson, *Chem. Rev.*, **1982**, *82*, 541-552.
10. A. P. de Silva, H. Q. N. Gunaratne and T. E. Rice, *Angew. Chem. Int. Ed. Engl.*, **1996**, *35*, 2116-2118.
11. D. Parker, *Coord. Chem. Rev.*, **2000**, *205*, 109-130.
12. A. Dossing, *Eur. J. Inorg. Chem.*, **2005**, 1425-1434.
13. N. Armaroli, G. Accorsi, P. Barigelletti, S. M. Couchman, J. S. Fleming, N. C. Harden, J. C. Jeffery, K. L. V. Mann, J. A. McCleverty, L. H. Rees, S. R. Starling and M. D. Ward, *Inorg. Chem.*, **1999**, *38*, 5769-5776.
14. N. Sabbatini, M. Guardigli and J. M. Lehn, *Coord. Chem. Rev.*, **1993**, *123*, 201-228.
15. S. Quici, M. Cavazzini, G. Marzanni, G. Accorsi, N. Armaroli, B. Ventura and F. Barigelletti, *Inorg. Chem.*, **2005**, *44*, 529-537.
16. R. Englman and J. Jortner, *Mol. Phys.*, **1970**, *18*, 145-164.
17. T. Forster, *Faraday Discuss.*, **1959**, *27*, 7-17.

18. D. L. Dexter, *J. Chem. Phys.*, **1953**, *21*, 836-850.
19. C. Jorgensen and B. R. Judd, *Mol. Phys.*, **1964**, *8*, 281-290.
20. G. Ligner, R. Mohan, S. Knittel and G. Duportail, *Spectrochim. Acta, Part A*, **1990**, *46*, 797-802.
21. S. M. Bruno, R. A. S. Ferreira, F. A. A. Paz, L. D. Carlos, M. Pillinger, P. Ribeiro-Claro and I. S. Goncalves, *Inorg. Chem.*, **2009**, *48*, 4882-4895.
22. F. Halverson, J. S. Brinen and J. R. Leto, *J. Chem. Phys.*, **1964**, *40*, 2790-2792.
23. A. Listkowski, M. Pietraszkiewicz, G. Accorsi and J. Mohanraj, *Synth. Met.*, **2010**, *160*, 2377-2380.
24. A. Barbieri, G. Accorsi and N. Armaroli, *Chem. Commun.*, **2008**, 2185-2193.
25. N. Armaroli, *Chem. Soc. Rev.*, **2001**, *30*, 113-124.
26. D. V. Scaltrito, D. W. Thompson, J. A. O'Callaghan and G. J. Meyer, *Coord. Chem. Rev.*, **2000**, *208*, 243-266.
27. N. Armaroli, G. Accorsi, F. Cardinali and A. Listorti, *Top. Curr. Chem.*, **2007**, *280*, 69-115.
28. D. Felder, J. F. Nierengarten, F. Barigelletti, B. Ventura and N. Armaroli, *J. Am. Chem. Soc.*, **2001**, *123*, 6291-6299.
29. T. McCormick, W.-L. Jia and S. Wang, *Inorg. Chem.*, **2005**, *45*, 147-155.
30. D. G. Cuttell, S. M. Kuang, P. E. Fanwick, D. R. McMillin and R. A. Walton, *J. Am. Chem. Soc.*, **2002**, *124*, 6-7.
31. A. J. M. Miller, J. L. Dempsey and J. C. Peters, *Inorg. Chem.*, **2007**, *46*, 7244-7246.
32. S. M. Kuang, D. G. Cuttell, D. R. McMillin, P. E. Fanwick and R. A. Walton, *Inorg. Chem.*, **2002**, *41*, 3313-3322.
33. K. Saito, T. Arai, N. Takahashi, T. Tsukuda and T. Tsubomura, *Dalton Trans.*, **2006**, 4444-4448.
34. N. Armaroli, G. Accorsi, M. Holler, O. Moudam, J. F. Nierengarten, Z. Zhou, R. T. Wegh and R. Welter, *Adv. Mater.*, **2006**, *18*, 1313-1316.
35. Y.-J. Li, Z.-Y. Deng, X.-F. Xu, H.-B. Wu, Z.-X. Cao and Q.-M. Wang, *Chem. Commun.*, **2011**, *47*, 9179-9181.
36. J. R. Kirchhoff, R. E. Gamache, M. W. Blaskie, A. A. Del Paggio, R. K. Lengel and D. R. McMillin, *Inorg. Chem.*, **1983**, *22*, 2380-2384.
37. C. E. A. Palmer and D. R. McMillin, *Inorg. Chem.*, **1987**, *26*, 3837-3840.
38. P. A. Breddels, P. A. M. Berdowski, G. Blasse and D. R. McMillin, *J. Chem. Soc., Faraday Trans. 2*, **1982**, *78*, 595-601.

39. M. T. Buckner, T. G. Matthews, F. E. Lytle and D. R. McMillin, *J. Am. Chem. Soc.*, **1979**, *101*, 5846-5848.
40. D. J. Casadonte and D. R. McMillin, *J. Am. Chem. Soc.*, **1987**, *109*, 331-337.
41. R. A. Rader, D. R. McMillin, M. T. Buckner, T. G. Matthews, D. J. Casadonte, R. K. Lengel, S. B. Whittaker, L. M. Darmon and F. E. Lytle, *J. Am. Chem. Soc.*, **1981**, *103*, 5906-5912.
42. S. Campagna, F. Puntoriero, F. Nastasi, G. Bergamini and V. Balzani, *Top. Curr. Chem.*, **2007**, *280*, 117-214.
43. G. Accorsi, N. Armaroli, C. Duhayon, A. Saquet, B. Delavaux-Nicot, R. Welter, O. Moudam, M. Holler and J. F. Nierengarten, *Eur. J. Inorg. Chem.*, **2010**, 164-173.
44. R. M. Everly, R. Ziessel, J. Suffert and D. R. McMillin, *Inorg. Chem.*, **1991**, *30*, 559-561.
45. V. Kalsani, M. Schmittel, A. Listorti, G. Accorsi and N. Armaroli, *Inorg. Chem.*, **2006**, *45*, 2061-2067.
46. Z. A. Siddique, Y. Yamamoto, T. Ohno and K. Nozaki, *Inorg. Chem.*, **2003**, *42*, 6366-6378.
47. N. Armaroli, *ChemPhysChem*, **2008**, *9*, 371-373.
48. U. Hahn, J.-F. Nierengarten, B. Delavaux-Nicot, F. Monti, C. Chiorboli and N. Armaroli, *New J. Chem.*, **2011**, *35*, 2234-2244.

Chapter 3

Carbon nanotubes: processing techniques

3.1 Introduction

Carbon nanotubes (CNTs) are well renowned for their unparallel physical and chemical characters. From their discovery, CNTs have been grabbing attention around the globe, due to their potential applications in field–emission devices,[1] molecular electronics,[2] microelectronics,[3] optoelectronics,[4] gas storage,[5] sensing[6] and, other fields involving nanotechnology. The solubility and other handling problems of CNTs are as famous as their advantages, which limit their widespread uses in real world applications. To render these materials processable and enhance their applications, chemical functionalization with tailored appended functional groups has been undertaken,[7-9] enabling the integration of CNT's into multi–component organic materials.[10] The chemical approaches for the modification of CNTs can be covalent or non–covalent (*i.e.* supramolecular)[9] and, while the latter approach does not lead to structural modification of the carbon framework, preserving its key electronic and structural properties, covalent derivatization often leads to substantial structural and physical alterations, as a consequence of the rupture of π-conjugation. In principle, flexible oligomeric and polymeric architectures such as polyaromatic conjugates,[11-14] polymers[15-19] or DNA[20-22] can provide structures capable of a non–covalent wrapping of the CNTs surface by exploiting van der Waals and π-π interactions.[19] Notably, some conjugated oligomeric structures may lead to an improvement of the electronic properties, such as conductivities and charge mobility.[23-26] Hence, this approach is extremely versatile for the development of reproducible and facile processing methods, which improve the solubility[27-30] of CNTs without compromising their structural and physical properties. Exploring supramolecular chemistry would be handy to fabricate such polymers due to their directionality, strength, and versatility. In addition, their dynamic and combinatorial nature may enable healing and adaptation, and thereby self–organization, by means of secondary weak interactions, such as π–π and van der Waals.[31-34] Especially, the multiple–hydrogen bonds assisted engineering of polymeric structures renders reversibility in self-assembling processes.[35,36] Eventually,

supramolecular polymers are ideal candidates for the solubilization, manipulation and supramolecular functionalization of CNTs, because they could reversibly wrap around the graphitic walls.

The early part of this chapter deals with the reversible solubilization and functionalization of multiwalled carbon nanotubes (MWCNTs) through combined self-assembly and self–organization processes mediated by H-bonds. Following this, engineering supramolecular chiral fibres to solubilize selective chiral CNTs is discussed in detail.

3.2 Reversible solubilization of multiwalled carbon nanotubes

To accomplish the reversible solubilization of MWCNTs, a library of ditopic molecular modules that expose, complementary recognition motifs at their peripheries are designed and synthesized. Exploiting the mimics of complementary base pairing of DNA, a series of molecules featuring 2,6–di(acetylamino)pyridine moieties able to selectively and reversibly recognize uracil–bearing modules have been prepared (**Chart 3.2.1**). The hetero–molecular recognition between these units is mediated by triple parallel H-bonds established between the NH-N-NH (DAD) functions of the 2,6–di(acetylamino)pyridine and the CO-NH-CO (ADA) imidic groups of the uracil derivatives. Two types of molecular modules have been prepared: linear modules with the recognition sites positioned at 180° relative to each other (molecules **1a**-**b, 4**), and angular units (**2**, **3**) with binding residues at 60° or 120°. Our previous studies have shown that under suitable solvent polarity and temperature control molecules **1a/b** self–assembles and self–organizes with its complementary modules **2-4** to form nanowires.[35,36] The self-assembly and self–organization leading to the formation of the supramolecular polymers are driven by the H-bonding interactions between the complementary recognition sites linked to the aromatic units, which are characterized by different geometric constraints. These molecular components undergo self-assembly in $CHCl_3$, CH_2Cl_2 or toluene and, in presence of MWCNTs, they self–organize into supramolecular polymers that enfold the external MWCNTs' surface, prompting the solubilization of CNTs. Eventually, addition of polar solvents such as DMSO or MeOH, causes the rupture of the H-bonding interactions and, consequently, the partial detachment of the polymer from the carbon frameworks, followed by rapid precipitation of the CNTs. The precipitate is then re-solubilized upon solvent removal under vacuum, showing the reversibility of the proposed strategy.

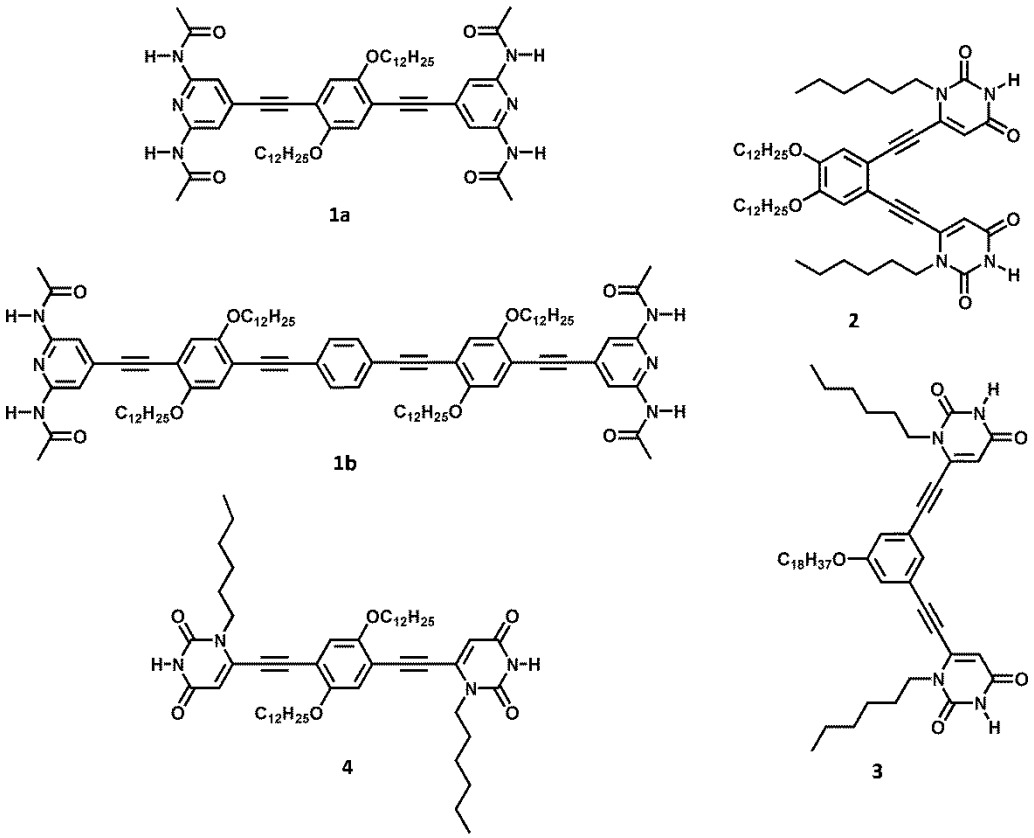

Chart 3.2.1 *Complementary H-bond forming 2,6-di(acetylamino)pyridine-(**1a**-**b**) and uracil-bearing (**2**-**4**) π-conjugated monomeric modules.*

3.2.1 Solubilization strategy

The strategy adopted for the reversible solubilization cycle of the MWCNTs is depicted in **Scheme 3.2.1**. The solution behavior of the hybrid **MWCNTs•[X•Y]$_n$** was monitored both by visual inspection and by using UV–VIS spectroscopy. In a classical experiment, a sample of **MWCNTs•[X•Y]$_n$** was prepared by addition of an equimolar solution of the complementary monomeric modules to a pre-sonicated dispersion of the pristine MWCNTs in $CHCl_3$ and stirred for 16 hours (**Figure 3.2.1c**). Interestingly, this procedure resulted in a very stable black solution (Step 1, **Scheme 3.2.1**). The crude solution was further purified by centrifuging at 15 krpm for 30 minutes (Step 2, **Scheme 3.2.1**) to remove unsolubilized MWCNTs and the supernatant solution was filtered through a Teflon(JH)Millipore® (0.45 μm) and washed with $CHCl_3$ to remove the excess of unbounded molecules, which could be recovered for subsequent solubilization cycles (Step 3, **Scheme 3.2.1**). The resulting black powder, **MWCNTs•[X•Y]$_n$** hybrid, was dried overnight in vacuum and re-dissolved (Step 4, **Scheme 3.2.1**) in $CHCl_3$ (or toluene or CH_2Cl_2) leading to very stable (after several months no precipitation has been detected, **Figure 3.2.1d**) dark solutions. These purified **MWCNTs•[X•Y]$_n$** hybrid solutions were further characterized

using various microscopic and spectroscopic techniques (*vide infra*). At this stage we assume that the solubility of MWCNTs is induced by intermolecular H-bonding interactions between the complementary monomeric molecular modules leading to a supramolecular polymer that wrap around CNTs. This proposed mechanism was indirectly confirmed in two ways: (i) ultrasonication and stirring of MWCNTs in the presence of individual molecular modules (i.e., bearing di(acetylamino)pyridine groups) lead to no apparent solubilization (**Figure 3.2.1b**) and (ii) addition of polar solvents like DMSO or MeOH causes immediate precipitation of CNTs (Step 5, **Scheme 3.2.1**, **Figure 3.2.1e**). The spectroscopic investigations carried out on the supernatant solution showed the presence of the constituting molecular units (*vide infra*), thus confirming the polymer detachment from the CNT walls. As a matter of fact, the efficiency of these triple hydrogen bonding interactions is known to decrease considerably in polar solvents like DMSO or MeOH, inducing the disruption of the H-bonded polymeric species and triggering desorption from the MWCNTs and consequent precipitation.

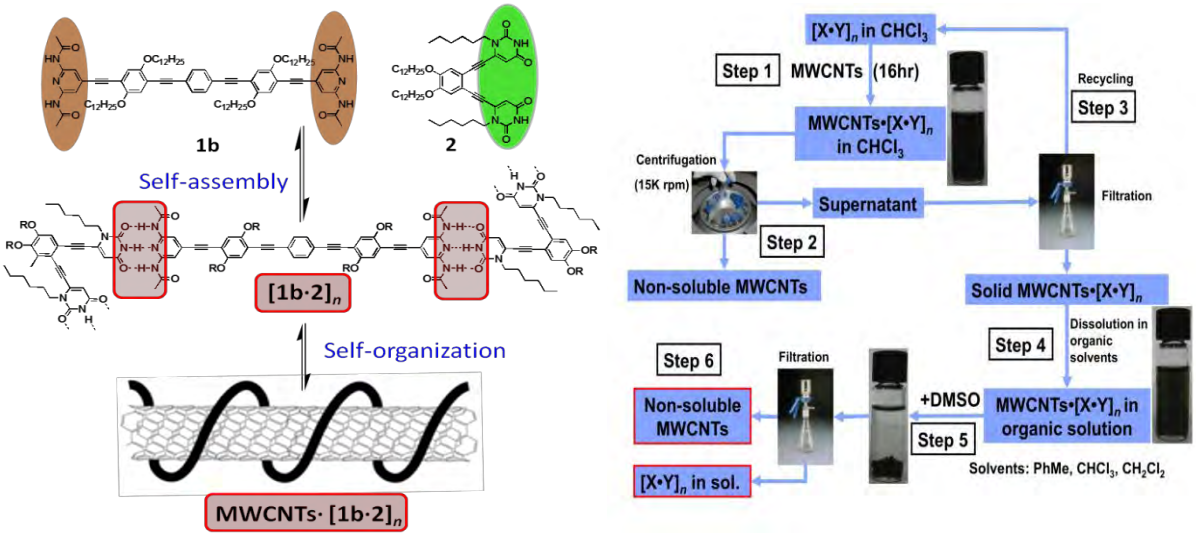

Scheme 3.2.1 *Left: schematic representation of the envisaged self-assembly between* ***1b*** *and* ***2****, and self–organization processes taking place in the presence of the MWCNTs; Right: schematic representation of the supramolecular functionalization protocol for the reversible solubilization of MWCNTs with supramolecular polymers* $[\mathbf{X{\bullet}Y}]_n$.

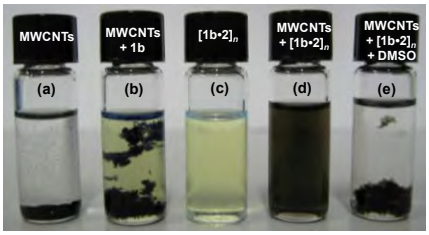

Figure 3.2.1 *$CHCl_3$ solution containing (a) MWCNTs, (b) MWCNTs and* ***1b****, (c) polymer* $[\mathbf{1b{\bullet}2}]_n$*, (d) hybrid* $\mathbf{MWCNTs{\bullet}[1b{\bullet}2]}_n$*, and (e)* ***MWCNTs****,* ***1*** *and* ***2*** *after the addition of DMSO.*

3.2.2 Photophysical investigations: absorption and fluorescence spectroscopies.

The absorption and emission properties of the investigated hydrogen bonding molecular units are depicted in **Figure 3.2.2** and their photophysical properties are summarized in **Table 3.2.1**. Our previous investigations[35-37] have shown that molecules **1-4** exhibit intense absorption in the UV–visible region and are good luminophores in solution ($CHCl_3$). For example **1a**, **1b** and **4** exhibit emission quantum yields as high as ~1, 0.8 and 0.9 respectively, whereas **2** and **3** show weaker quantum yields of ~0.3 and ~0.01.

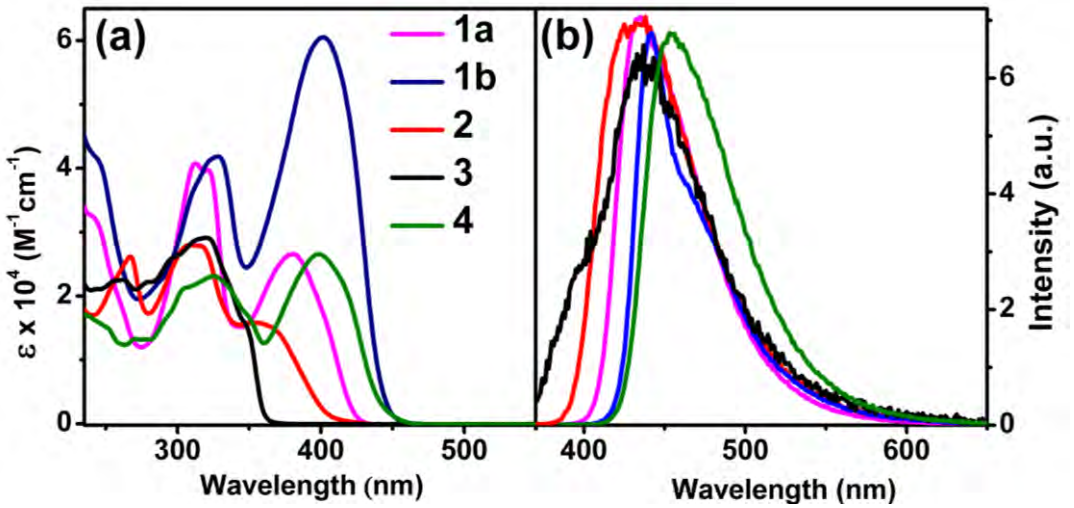

Figure 3.2.2 *(a) Absorption and (b) fluorescence spectra of **1-4** in chloroform. Emission profiles were recorded upon excitation at 308 nm.*

Table 3.2.1 *Photophysical properties of H-bond forming molecular modules in $CHCl_3$.*

Compounds	$\lambda_{abs.\ max}$ (nm)	$\lambda_{em.\ max}$ (nm)	Φ_{em} (%)	τ_{em} (ns)
1a	312, 380	435	~100	2.5
1b	330, 398	440	84	1.0
2	305, 354	430	28	1.4
3	320, 350	435	1	2.3
4	325, 400	455	93	1.9

Figure 3.2.3 summarizes the absorption spectral study on different combinations of the complementary hydrogen bonding modules **1a**, **1b**, **2** and **3** compared to the corresponding optically transparent solutions of supramolecularly solubilized **MWCNTs•[X•Y]$_n$** in $CHCl_3$ (UV-Vis measurement on series of [1b•4]$_n$ could not be carried out due to lack of samples). Equimolar

mixtures of the complementary molecules resemble those of their corresponding algebraic sum, except for the combinations of linear linkers **1a** and **1b** with **3**, which exhibit a weak new feature on the lower energy side (420 nm for **[1a•3]**$_n$, 460 nm for **[1b•3]**$_n$, see the arrows in **Figure 3.2.3**). The presence of this new feature at longer wavelengths is taken as a clue for the formation of supramolecular polymers arising from the combination of H-bond–directed self-assembly and self–organization processes (*vide infra*).[35-37] On the contrary, the absorption spectra of solubilized MWCNTs did not reveal any features corresponding to the presence of either of the molecular components. The possible reasons for this observation are (i) overwhelming absorption of CNTs (ii) supramolecular organization of molecules into new material which perturbs their initial spectra or (iii) a combination of these effects. More interestingly, in the case of MWCNTs solubilized using **1b** with a combination of either **2** or **3**, we observed a weak band at the longer wavelengths (see the encircled areas in **Figure 3.2.3**). For example, the **MWCNTs•[1b•2]**$_n$ exhibits a shoulder at 490 nm and **MWCNTs•[1b•3]**$_n$ has weak absorption at 455 nm. In other cases, **MWCNTs•[1a•2]**$_n$ and **MWCNTs•[1a•3]**$_n$ the new bands are hardly visible. The origin of this new absorption feature is attributed to the presence of supramolecular polymeric materials on the surface of MWCNTs (*vide infra*).[35-37]

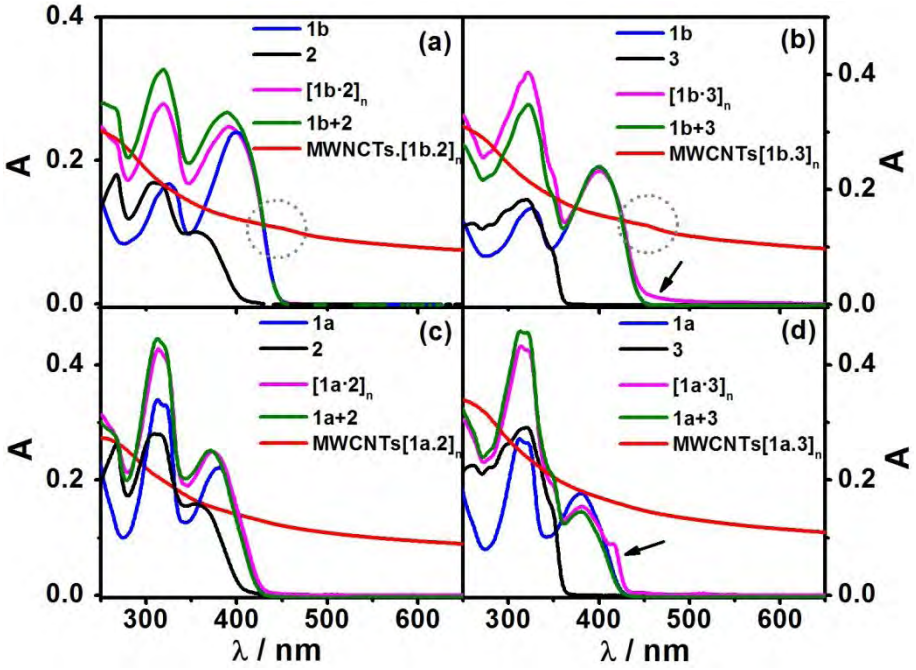

Figure 3.2.3 *Absorption spectra of isolated molecular subunits (**1-3,** blue and black) and their combinations with (red) and without MWCNTs (magenta) in $CHCl_3$. Green lines correspond to the algebraic sum of absorption of individual complementary units.*

In parallel to the absorption spectral measurements, we investigated the emission properties of the **MWCNTs•[X•Y]**$_n$ materials. None of the solubilized **MWCNTs•[X•Y]**$_n$ materials show significant emission signals. As an example, the fluorescence spectra of **1b**, **2**,

their equimolar mixture (**[1b•2]$_n$**), and an optically transparent solution of **MWCNTs•[1b•2]$_n$** in $CHCl_3$ are reported in **Figure 3.2.4**. The solutions were excited at 360 nm where the two molecules, **1b** and **2** exhibit the same absorbance at the used concentration (3.3×10^{-6} M in $CHCl_3$). The largely predominant luminescence signal in **[1b•2]$_n$** stems from molecule **1b** because it exhibits a higher fluorescence quantum yield (84%) compared to the angular module **2** (28%), and this is confirmed by the excitation spectrum, which matches with that of **1b** (**Figure 3.2.4**). By contrast, under identical conditions, **MWCNTs•[1b•2]$_n$** did not show any significant fluorescence; the residual signal, shown in the inset of **Figure 3.2.4** arises most likely from the presence of traces of unbound molecules in solution as it is confirmed by lifetime measurements (τ = 1 ns).

In principle, this observation could be due to the virtual absence of molecules in solution or to the fluorescence quenching of the fluorophore through energy transfer to the low lying states of MWCNTs. The former explanation is ruled out by further manipulation of the sample. Addition of DMSO (1:3 v/v), followed by filtration of the resulting precipitated MWCNTs, leads to a solution exhibiting a neat fluorescence band fully superimposable in shape to that of **[1b+2]**; the absorption traces also match with related absorption features of **[1b+2]** (**Figure 3.2.5**). It should be noted that the differences in the absorption features at shorter wavelengths is due to the presence of DMSO and to the non–precipitated CNTs. Notably, upon addition of DMSO, the feature observed at 490 nm for a solution of **MWCNTs•[1b•2]$_n$** in $CHCl_3$ is blue shifted to 400 nm (before the filtration of MWCNTs, see the arrows in **Figure 3.2.5c**). Our previous investigations have shown that in non-polar solvents like cyclohexane and toluene a 1:1 mixture of molecular modules bearing complementary H-bonding functionalities at both ends undergo self-assembly and self-organization leading to the formation of nanowires, which exhibit red–shifted absorption features due to $\pi-\pi$ interactions.[35-38] The new band observed at 490 nm for **MWCNTs•[1b•2]$_n$** is thus attributed to the supramolecular **[1b•2]$_n$** polymer species on the surface of MWCNTs. This assumption is corroborated by the spectral studies performed as a function of temperature. In fact, an increase of temperature is expected to cause the disassembling of supramolecular polymers and the detachment of molecules from the surface of nanotubes,[37,38] with suppression of energy transfer from molecules to MWCNTs. Absorption spectral studies performed as a function of temperature did not provide reliable data due to lack of optical transparency, following the formation of large CNTs' aggregates at higher temperatures. On the contrary, fluorescence spectra recorded in the temperature range of 303-353 K show a more than a two–fold increase of the **[1b•2]$_n$**-centered fluorescence intensity (**Figure 3.2.5d**).

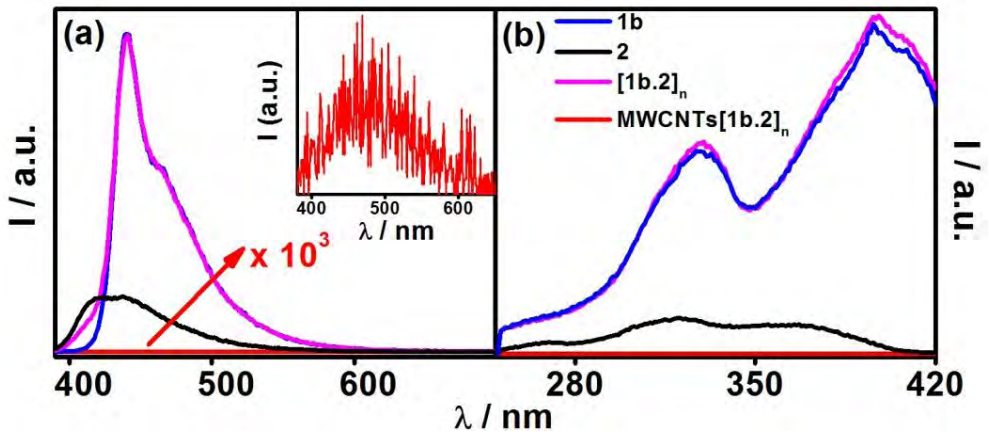

Figure 3.2.4 *(a) Emission and (b) excitation spectra of* ***1b*** *(blue),* ***2*** *(black),* ***[1b•2]$_n$*** *(magenta) and* ***MWCNTs•[1b•2]$_n$*** *(red) in $CHCl_3$. Inset: residual emission from* ***MWCNTs•[1b•2]$_n$****. Emission spectra are collected upon excitation at 360 nm and excitation spectra are recorded at the respective emission maximum.*

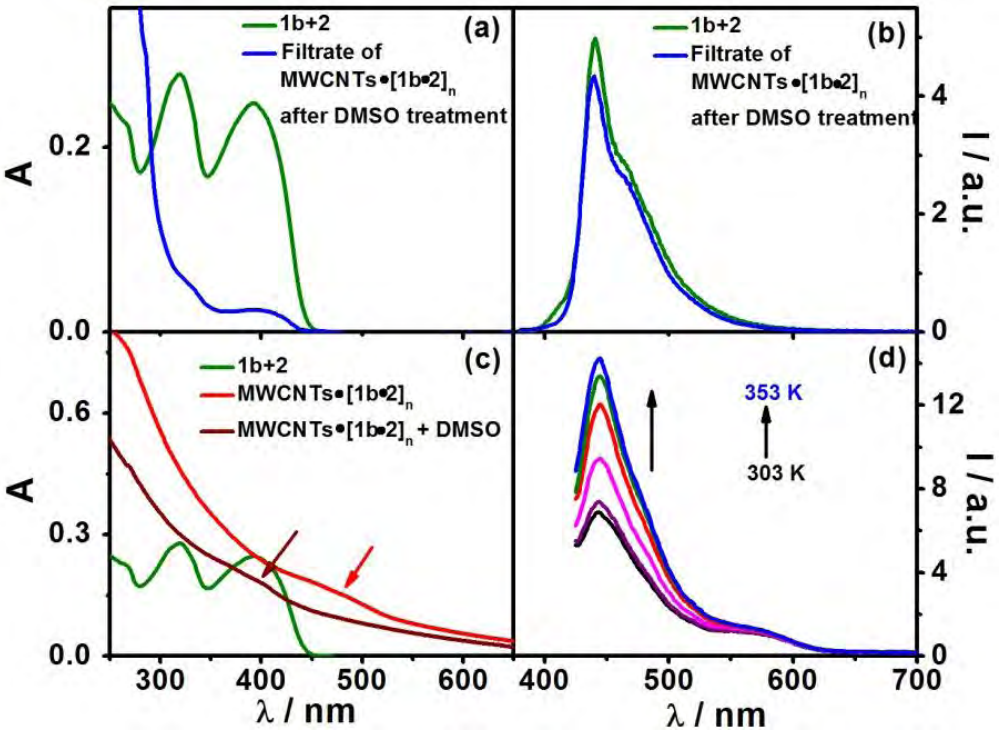

Figure 3.2.5 *(a) Absorption and (b) emission spectra of* ***[1b•2]$_n$*** *(green) and the filtrate of* ***MWCNTs•[1b•2]$_n$*** *(blue) after DMSO treatment. (c) comparison of absorption spectra of* ***[1b•2]$_n$*** *(green),* ***MWCNTs•[1b•2]$_n$*** *(red) and* ***MWCNTs•[1b•2]$_n$*** *in presence of DMSO (brown) (d) Emission spectral changes of* ***MWCNTs•[1b•2]$_n$*** *as a function of temperature.*

A further proof for the reversibility of polymer (see **Scheme 3.2.1**) wrapping onto the CNTs is displayed in **Figure 3.2.6**. Upon addition of MeOH (2:1 v/v) into a solution of **MWCNTs•[1b•2]$_n$** in $CHCl_3$, a precipitation of MWCNTs was observed as a consequence of the disruption of the hydrogen-bonding interactions (see the particles in sample b, **Figure 3.2.6a**). Complete removal of the solvent through *in-vacuo* evaporation, left the sample at the bottom of the flask as black precipitate. Re-dispersion of the black precipitate in $CHCl_3$ under mild

sonication led to an optically neat solution (sample d in **Figure 3.2.6a**). The normalized absorption spectra of **MWCNTs•[1b•2]$_n$** before and after MeOH treatment in $CHCl_3$ (**Figure 3.2.6b**) largely exhibit the same spectroscopic features, indicating the reversibility of the self-assembly and self–organization processes.

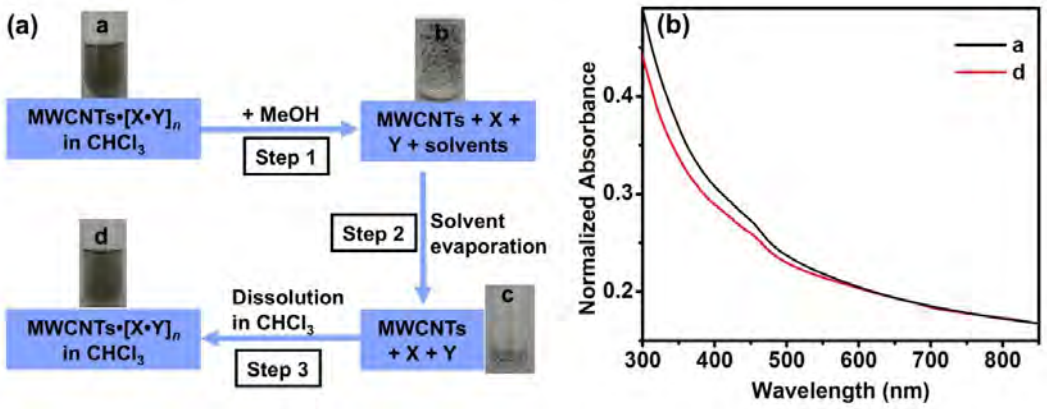

Figure 3.2.6 *(a) Photographs showing visual changes under MeOH treatment and resolublization of* ***MWCNTs•[1b•2]$_n$*** *in $CHCl_3$. (b) Normalized absorption spectra of* ***MWCNTs•[1b•2]$_n$*** *before MeOH treatment in chloroform (a, black) and redissolved in $CHCl_3$ after MeOH addition (d, red); absorption spectra are normalized at 850 nm.*

3.2.3 Microscopic analysis: AFM and UHV-STM studies

The attachment of supramolecular polymers on the surface of MWCNTs is further confirmed with AFM/STM investigations. AFM samples were prepared by drop-casting ~20 μL of the corresponding solubilized **MWCNTs•[X•Y]$_n$** onto a freshly cleaved mica surface. The samples were air dried and imaged with an AFM apparatus in the tapping mode. Typical AFM images of solubilized MWCNTs using different molecular combinations are presented in **Figure 3.2.7**. The large–scale images recorded from different areas of the samples indicated the presence of well–separated MWCNTs. A closer analysis of these samples by real-time zooming clearly showed the presence of periodic structures having alternating lumps on MWCNTs. The distance between either two adjacent heights or depths ranges from 50–100 nm. These periodic structures are attributed to the supramolecular hydrogen bonded polymeric nanowires that efficiently wrap around MWCNTs (see **Scheme 3.2.1**), thus imparting solubility.

The morphological properties of the **MWCNTs•[X•Y]$_n$** hybrids have been also investigated by means of STM under UHV conditions (see **MWCNTs•[1a•2]$_n$** as an example in **Figure 3.2.7**) after spin coating $CHCl_3$ solution onto a Au/mica substrate. Due to the convolution of the tip shape with the surface topography, the measure of a **MWCNTs•[1a•2]$_n$** diameter by STM must be extracted from the height of the **MWCNTs•[1a•2]$_n$**, rather than their apparent

width. The diameter of the **MWCNTs•[1a•2]$_n$** ranges from 8 to 18 nm. The MWCNTs used is these studies are size selected.

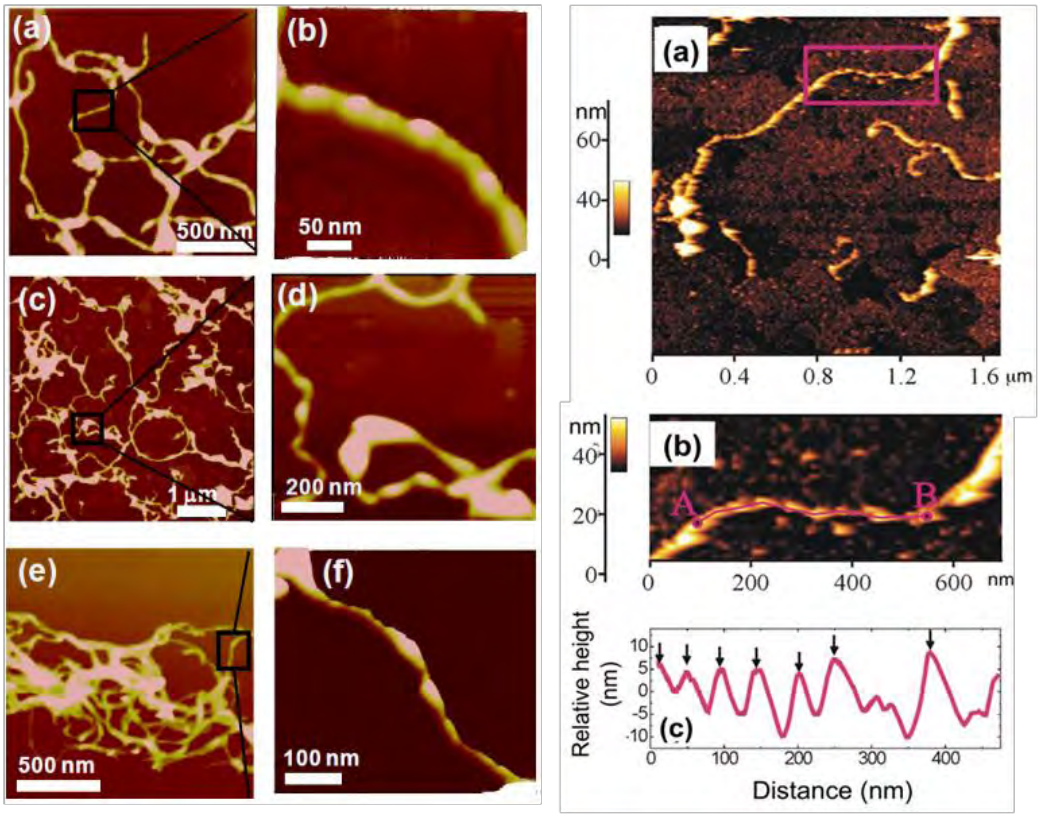

Figure 3.2.7 *Left: Topographic TM–AFM images of (a)* ***MWCNTs•[1a•3]$_n$****, (c)* ***MWCNTs•[1b•2]$_n$*** *and (e)* ***MWCNTs•[1b•3]$_n$*** *as deposited by spin-coating $CHCl_3$ solution on silicon surfaces. Images (b), (d), and (f) represent the zoomed 3D images clearly showing a periodic structures of the helical wrapping of the MWCNT (images (b) and (f) are rotated by 90° for clarity reasons).Right: STM image of (a)* ***MWCNTs•[1a•2]$_n$*** *spin-coated onto Au(111)/mica surface; (b) zoomed area showing the presence of periodic lumps on the* ***MWCNTs•[1a•2]$_n$*** *hybrids; (c) height profile along the line A to B, clearly displaying the periodic height oscillation that derives from the helical wrapping of the polymer around a MWCNT (cfr with AFM images).*

The reason for the spreading of **MWCNTs•[1a•2]$_n$** height measurement is attributed to the wrapping of polymer **[1a•2]$_n$**. The most striking characteristic observed in the images is the presence of bright periodic lumps (**Figure 3.2.7b and c**) on the outer surface of all analyzed **MWCNTs•[1a•2]$_n$** hybrids. The corrugation (resp. periodicity) of the pattern is approximately 9 nm (resp. 50 nm), which are attributed to the organic functions of the polymeric structure.

3.3 Supramolecularly engineered, chirality induced helical fibers

As **Section 3.2** and our earlier work[35-38] demonstrate the facile route to engineer polymeric nano structures such as, nanoparticles, nanovesicles, nanofibres and nanorods, once again, the advantage has been taken on multiple H-bonding organic scaffolds, peripherally equipped with 2,6-di(acetylamino)pyridine or uracil units to impart molecular chirality to the microscopic level. With this aim, enantiomerically-pure uracil-derived binaphtols (**1R** and **1S)** and bis 2,6-di(acetylamino)pyridine derivative (**2**) are synthesiszed and their self-assembling properties are traced with variable temperature 1H-NMR, circular dichroism, photophysical studies and microscopic analysis. The optimized geometries of the synthesized compounds and the envisaged self-assembled polymeric structure are displayed in **Scheme 3.3.1**.

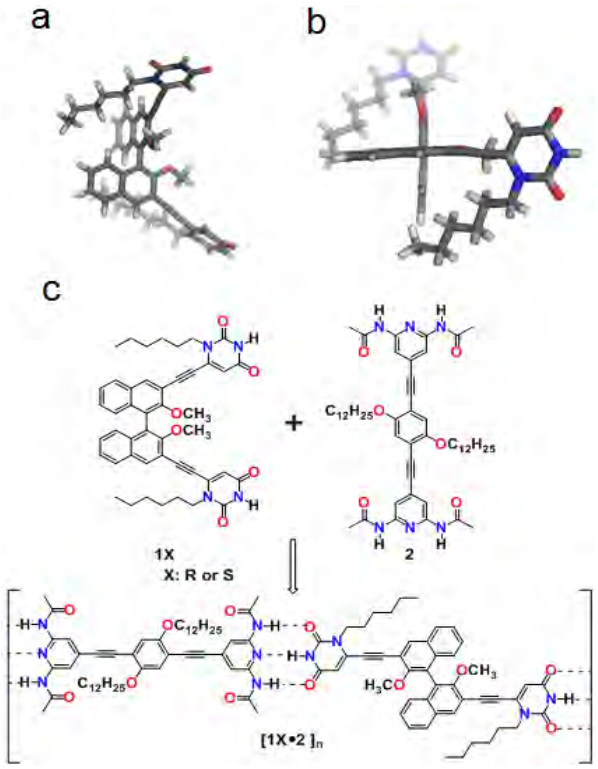

Scheme 3.3.1 *Lateral (a) and top (b) view of the PM3 optimized geometrical structure of binaphtol derivative **1** (R) as implemented within Spartan. Schematic representation (c) of self-assembly process between molecular modules **1X** and **2** leading to [**1X•2**]$_n$. X: **R** or **S**.*

3.3.1 Synthesis of H-bond forming complementary modules

The complementary modules are prepared following a four-step synthetic protocol starting from the enantiomerically pure R/S-binol (**Scheme 3.3.2**). Methylation of the hydroxyl groups of binol by treatment with MeI in presence of K_2CO_3 afforded the alkylated derivatives **3**, which were

subsequently reacted with BuLi and I_2 in presence of TMEDA to originate the diiododerivatives **4**.[39] Pd-catalyzed *Sonogashira* cross-coupling between **4** and TMSA in presence of $[Pd(PPh_3)_2Cl_2]$ and CuI at 110 °C, followed by in situ deprotection with K_2CO_3 afforded diethynylated compound **5**.[40] *Sonogashira*-type cross-coupling reaction between **5** and **6** in the presence of $[Pd(PPh_3)]_4$ and CuI yielded modules **1R**-**S**. The linear module **2** and the uracilic derivatives **6** were prepared following previously reported protocols.[35,36]

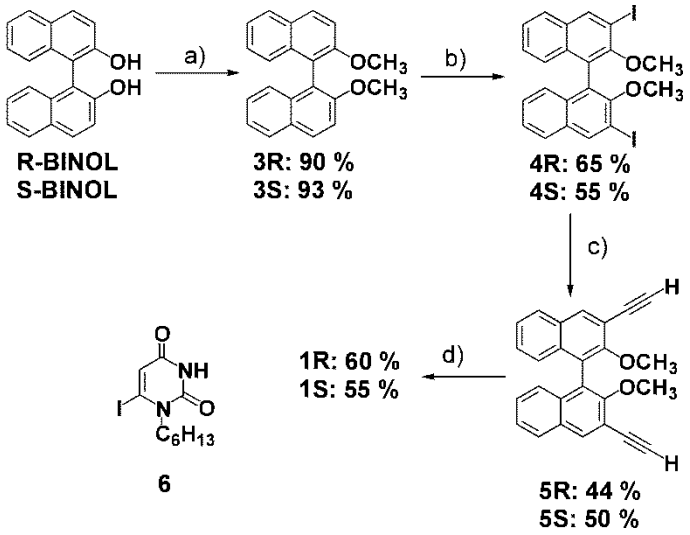

***Scheme** 3.3.2 Synthetic pathway adopted for the preparation of **1R-S**. (a) K_2CO_3, MeI, Acetone, reflux; (b) BuLi, TMEDA, I_2, Et_2O, -78 °C; (c) 1.$[Pd(PPh_3)_2Cl_2]$, CuI, TMSA, Tol, NEt_3 110 °C; 2. K_2CO_3, THF/MeOH; (d) $[Pd(PPh_3)_4]$, CuI, **6**, THF, NEt_3, r.t. TMSA: trimethylsilylacetylene.*

3.3.2 Characterization of supramolecular assembly

3.3.2.1 Variable temperature ^{1}H-NMR studies

To shed light on the effective molecular recognition of 2,6-di(acetylamino)pyridine and uracil motifs, variable temperature (VT) ^{1}H-NMR analysis was performed on a stoichiometric 1:1 mixture of **1R** and **2** in tetrachloroethane-d_2 (**Figure 3.3.1**). Upon increasing the temperature from 20 to 80 °C, a clear shift at higher fields of the "NH" proton resonances involved in the multiple H-bonding has been observed (from 10.5 to 9.0 ppm and 8.0 to 7.6 ppm, respectively), clearly indicating the progressive disruption of the H-bonds, and thus of the self-organized structure.

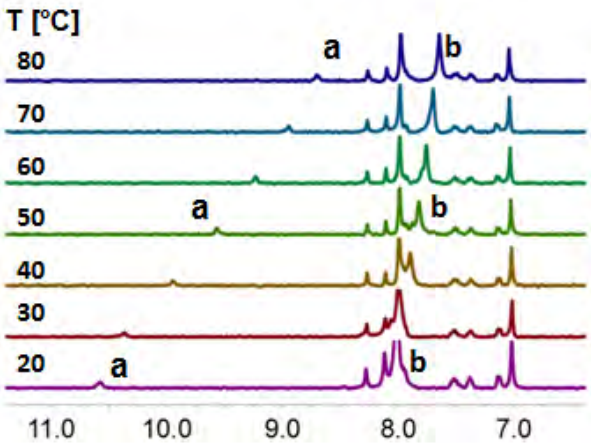

Figure 3.3.1 *VT-^{1}H-NMR spectra of a 1:1 mixture of **1R** and **2** in tetrachloroethane-d_2, immidic protons of **1R** and amidic protons of **2** are marked with letter a and b, respectively.*

3.3.2.2 Photophysical analysis

The electronic absorption and emission spectra of **1R**, **2** and supramolecular adduct **[1R•2]$_n$** obtained by mixing the two components in a 1:1 ratio (3.5 μM each) in CHX/THF, (5% v/v) are shown in **Figure 3.3.2a**. The absorption spectrum of **1** is placed entirely in the UV region and is weaker and narrower compared to the same of **2**. Both molecules exhibit fluorescence and the quantum yield of **1R** (Φ_{fl} = 0.12) is smaller than that of **2** (Φ_{fl} = 0.18). Notably, the absorption and emission features of **2** in the CHX/THF mixture are red-shifted compared to the same in more polar solvents such as methanol and THF.[35,41] These findings confirm the self-aggregation of **2**, most likely through *J*-type association, driven by solvophobic interactions as previously observed.[37,42,43] Although the UV-Vis spectrum of **[1R•2]$_n$** is dominated by the characteristic features of **2**, some notable differences are present in comparison with the algebraic sum of the two components alones. A smaller intensity ratio between the peaks at 340 and 415 nm, along with an enhanced absorption tail after 450 nm, are observed. Furthermore, the emission of **[1R•2]$_n$** shows a weak shoulder at the longer wavelengths and, compared to **2**, a lower quantum yield (Φ_{fl} = 0.12) and a higher full width at half maximum (FWHM), *i.e.* 80 nm (**2**: 62 nm, **Figure 3.3.2a** inset). In this case, differently from previous reports,[37,44] the supramolecular interaction between **1R** and **2** does not result in distinctly new absorption and fluorescence bands in the low energy spectral region. Despite the presence of a self-organized fiber-like arrangement as displayed by the microscopy imaging technique (*vide infra*), the perpendicular orientation adopted by the naphthyl rings drastically reduce the inter-polymeric π-π interactions between single self-assembled **[1R•2]$_n$** chains, thus leading to looser aggregation. However, the small changes observed in the absorption and emission spectra of **[1R•2]$_n$** along with the lifetime

values (3.4 ns for **1R**; τ_1 = 1.5 ns; τ_2 = 3.7 ns for **2**; τ_1 = 1.2 ns; τ_2 = 4.2 ns for **[1R•2]$_n$**) are ascribed to the presence of the H-bonded self-organized structures in CHX/THF (**Figure 3.3.3**).

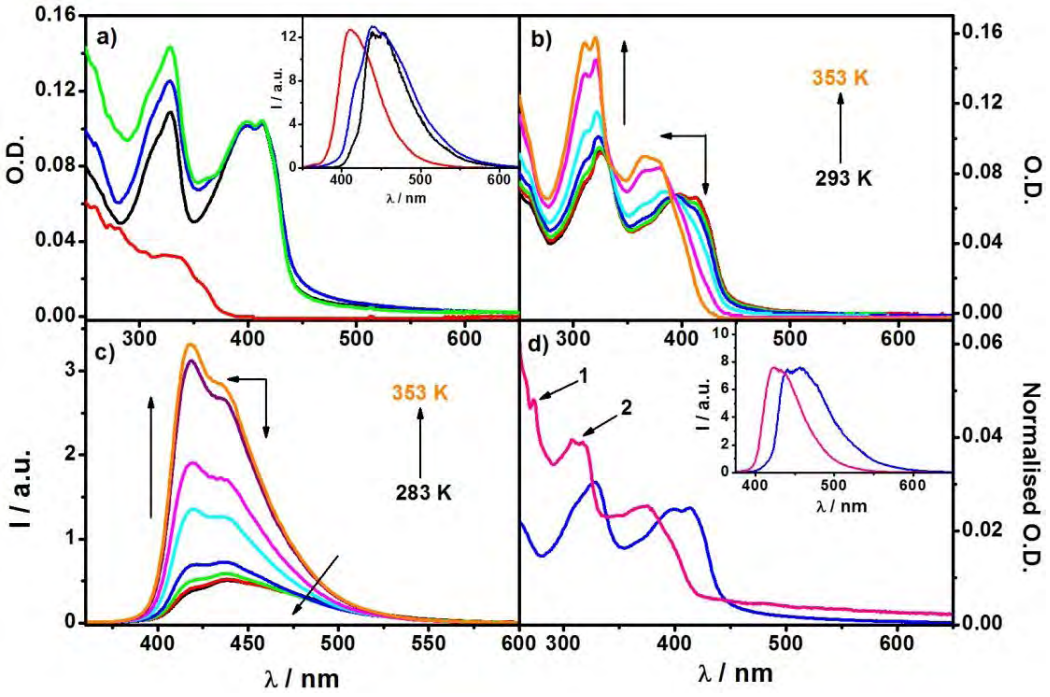

Figure 3.3.2 *a) Electronic absorption and (inset) normalized fluorescence spectra of* ***1R*** *(red),* ***2*** *(black),* ***[1R•2]$_n$*** *(blue) and algebraic sum of* ***1R*** *and* ***2*** *(green) in CHX/THF (95:5 v/v). b) Absorption spectral changes of 1:1 ([**C**] = 3.5 μM each) mixture of* ***1R*** *and* ***2*** *during VT measurement. c) VT Emission spectral changes of* ***[1R•2]$_n$*** *at the heating rate of 10 K. d) Absorption and (inset) normalized fluorescence spectra of* ***[1R•2]$_n$*** *before (blue) and after (pink) the addition of DMSO.*

The self-organization process between **1R** and **2** in the CHX/THF mixture is further confirmed by VT-UV-vis and fluorescence measurements. On increasing the temperature to 353 K, the absorption spectrum of **[1R•2]$_n$** shows an isosbestic point at 393 nm, a gradual hypsochromic shift and an increased peak intensity ratio between the bands centered at 340 and 415 nm (**Figure 3.3.2b**). In particular, the absorption tail in the lowest-energy spectrum completely vanishes. Likewise, the emission at high temperature shows blue shifted maximum with substantially reduced FWHM (52 nm) and disappearance of the extended shoulder at longer wavelengths (**Figure 3.3.2c**). These observations indicate the presence of isolated units of **2** in the sample. In order to corroborate the presence of H-bonds between **1R** and **2**, a H-bond disrupting polar solvent such as DMSO (5% v/v) was added to a solution of **[1R•2]$_n$**. Due to the loss of H-bonds, the absorption spectrum of **[1R•2]$_n$** shows blue shifted spectral features with discernible signatures of individual molecular units **1R** and **2** (**Figure 3.3.2d**). Similarly, the fluorescence spectrum moves to higher energy (as observed at 353 K), and exhibits much higher intensity (**Figure 3.3.2d** inset). Owing to the high quantum yield of monomer unit **2** (Φ_{fl} = 0.81), the

emission peak of the latter masks the signal from weakly emissive **1R** (Φ_{fl} = 0.15) in the present solvents mixture.

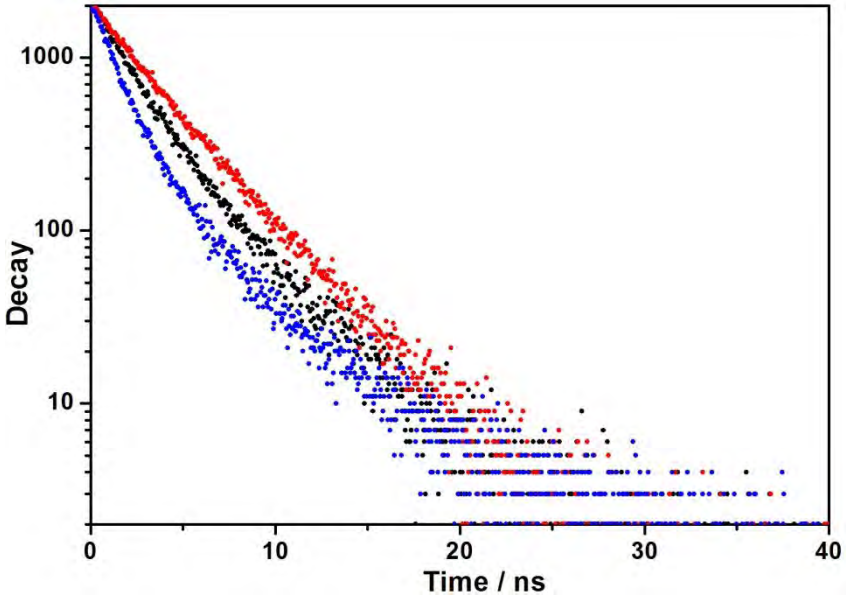

Figure 3.3.3 *Emission decay profiles of **1** (red), **2** (black) and **[1•2]$_n$** (blue) in CHX/THF (5 v/v) solvent mixture.*

3.3.2.3 Variable temperature circular dichroism measurements

To investigate the chirality expression on the self-organized assemblies originated from the combination of **1R** and **1S** with the linear ditopic unit **2**, CD experiments were also carried out both on the single components and on the relative assemblies. The CD spectra of the binaphtol derivatives are characterized by a maximum at 260 nm and an overall CD effect which take place in the region between 220 and 390 nm (**Figure 3.3.4a**). When linear module **2** is added to a CHX-THF solution of **1R** or **1S**, a new band appears in 400-480 nm region (**Figure 3.3.4b**), in which no single components are CD active. This new band can be attributed to the formation of a new chiral entity defined by a high order level between its molecular components. The variation of the CD effect as a function of temperature was recorded for both **[1R•2]$_n$** and **[1S•2]$_n$** assemblies displaying similar trends (**Figure 3.3.4b**). Notably, the behavior of the new band at 430 nm is in strict accordance with the data reported in the temperature-dependent UV measurements (**Figure 3.3.2**). Also in this case the VT experiments from 10 to 80 °C induce a progressive reduction of the CD effect (attaining zero at approximatively 50 °C) displaying the rupture of self-assembled chiral structures at high temperatures.

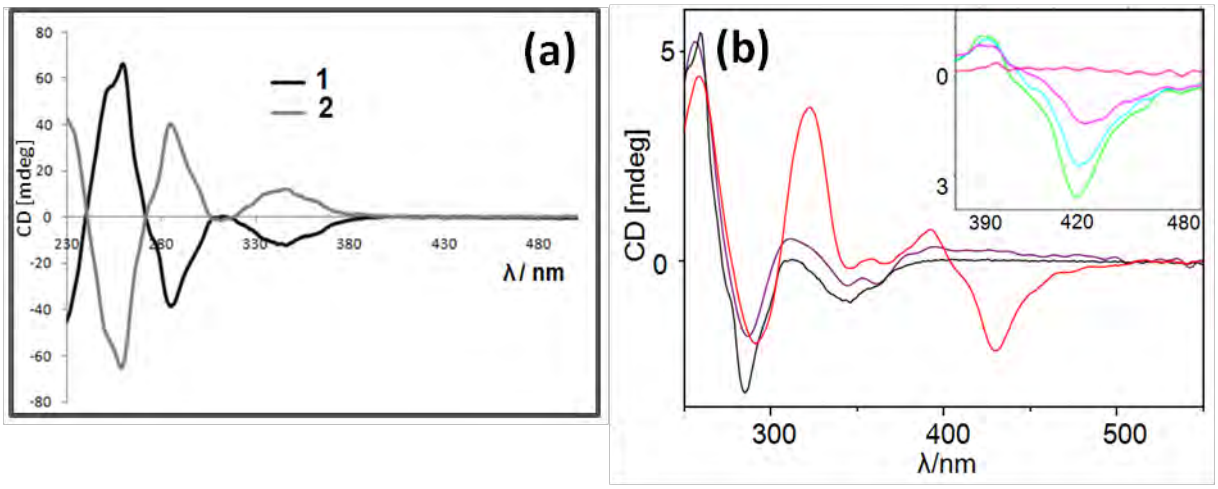

Figure 3.3.4 *CD spectra (a) recorded at 20 °C of* ***1R*** *(black line) and* ***1S*** *(grey line) in a 95:5 (v/v) mixture of CHX-THF at the concentration of 1.3 * 10^{-3} M.(b) CD-spectral profile of* ***1R*** *at rt (black line),* ***[1R•2]$_n$*** *at 5 °C (red line) and at 60 °C (purple line) in CHX-THF (95-5). The inset shows the complete disappearance of the band centered at 430 nm upon T increasing (from 5 to 60 °C).*

3.3.2.4 Microscopic analyses

Further confirmation of the presence of nanometric fibers is obtained through microscopical tapping mode (TM)-AFM analysis of a drop-casted CHX-THF solution containing **[1R•2]$_n$** or **[1S•2]$_n$** onto mica surfaces (**Figure 3.3.5**). The same results are also obtained with TEM imaging of **[1R•2]$_n$** and **[1S•2]$_n$** deposited on glassy-carbon grids. The TEM images of **[1R•2]$_n$** and **[1S•2]$_n$**, taken at different magnification are reported in Figure **3.3.6**.

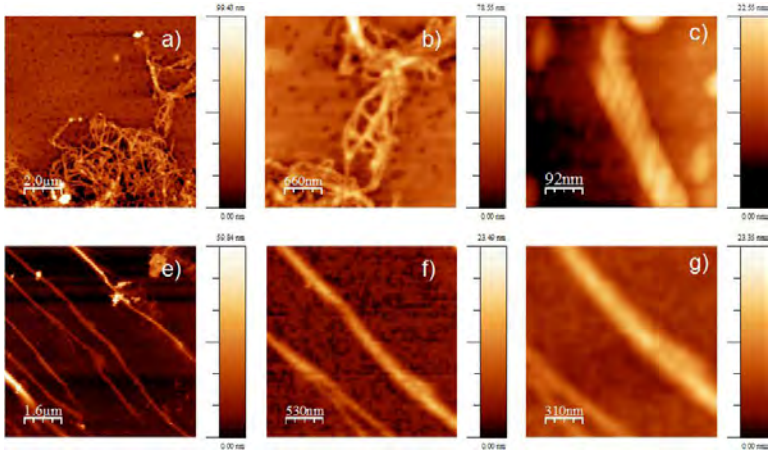

Figure 3.3.5 *TM-AFM images of assemblies* ***[1R•2]$_n$*** *(a-c) and* ***[1S•2]$_n$*** *(d-f) as deposited on mica surface following the above procedure.*

The fibrous materials display diameters ranging from 5 to 10 nm and an average length between 800 nm and 3.0 μm. Notably, all nanofibres show a remarkable inclination to wrap, forming "super coiled" helicoidal architectures (**Figure 3.3.5c** and **Figure 3.3.6c**). Considering the

presence of CHX as the main solvent, it is reasonable to hypothesize that the $C_{12}H_{25}$ appends of linear molecular modules **2** are reasonably exposed on the external side of the fibres forming a hydrophobic coat, allowing extensive van der Waals inter-fibre interactions.

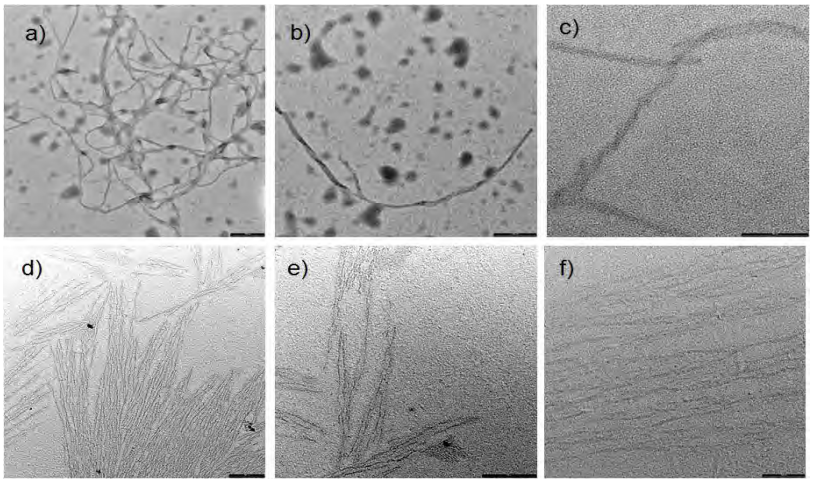

Figure 3.3.6 *TEM images at different magnification of the* ***[1R•2]$_n$*** *assembly (a-c) and of the* ***[1S•2]$_n$*** *(d-f) as obtained after drop casting on a carbon coated nickel grid.*

3.4 Summary

The research works described in this chapter introduce the idea of using H-bonded polymers to carry out a reversible supramolecular derivatization of MWCNTs, exploiting the dynamic non-covalent character of weak triple H-bonding interactions such as those established between complementary uracil and the 2,6-di(acetylamino)pyridyl recognition moieties. In particular, oligophenyleneethynylene molecular modules promote the self-assembly process of H-bonded supramolecular polymers that self-organize on the CNTs' surfaces in non-polar organic media and disassemble upon addition of polar H-bond-breaking solvents (*e.g.* MeOH or DMSO). Unambiguous proofs of the formation of **MWCNTs•[X•Y]$_n$** hybrids have been provided by several spectroscopic (absorption and emission) and microscopic (AFM, STM) techniques. The concept of reversible solubilization of MWCNTs is unequivocally proved by photophysical methods. By exploiting the same principle, chiral polymeric structures have been prepared using enantiomerically pure uracil-derived binaphtols and di(acetylamino)pyridinic linear units, under solvent and temperature control. These chiral structures can hold great promises to selectively solubilise or to separate chiral nanotubes from the bulk mixture. In fact, if properly functionalized, the supramolecular polymers here introduced can be regarded as an alternative strategy to introduce desired functionalities onto the CNTs' framework leaving unaltered its

structural, chemical and physical properties. This opens up new avenues toward the use of these carbon nanostructures into novel applications.

3.5 References

1. M. Terrones, *Int. Mater. Rev.*, **2004**, *49*, 325-377.
2. W. Lu and C. M. Lieber, *Nat. Mater.*, **2007**, *6*, 841-850.
3. F. Kreupl, *Carbon Nanotubes in Microelectronic Applications*, Wiley-VCH, Verlag GmbH & Co. KgaA, 2008.
4. P. Avouris, M. Freitag and V. Perebeinos, *Nat. Photonics*, **2008**, *2*, 341-350.
5. K. L. Lim, H. Kazemian, Z. Yaakob and W. R. W. Daud, *Chem. Eng. Technol.*, **2010**, *33*, 213-226.
6. J. Kong, N. R. Franklin, C. W. Zhou, M. G. Chapline, S. Peng, K. J. Cho and H. J. Dai, *Science*, **2000**, *287*, 622-625.
7. D. M. Guldi, G. M. A. Rahman, V. Sgobba and C. Ehli, *Chem. Soc. Rev.*, **2006**, *35*, 471-487.
8. M. Prato, K. Kostarelos and A. Bianco, *Acc. Chem. Res.*, **2008**, *41*, 60-68.
9. P. Singh, S. Campidelli, S. Giordani, D. Bonifazi, A. Bianco and M. Prato, *Chem. Soc. Rev.*, **2009**, *38*, 2214-2230.
10. F. D'Souza and O. Ito, *Chem. Commun.*, **2009**, 4913-4928.
11. J. Liu, O. Bibari, P. Mailley, J. Dijon, E. Rouviere, F. Sauter-Starace, P. Caillat, F. Vinet and G. Marchand, *New J. Chem.*, **2009**, *33*, 1017-1024.
12. E. M. Perez, B. M. Illescas, M. A. Herranz and N. Martin, *New J. Chem.*, **2009**, *33*, 228-234.
13. M. Yu, S.-Z. Zu, Y. Chen, Y.-P. Liu, B.-H. Han and Y. Liu, *Chem. Eur. J.*, **2010**, *16*, 1168-1174.
14. S.-Z. Zu, X.-X. Sun, Y. Liu and B.-H. Han, *Chem. Asian J.*, **2009**, *4*, 1562-1572.
15. J. Chen, H. Liu, W. A. Weimer, M. D. Halls, D. H. Waldeck and G. C. Walker, *J. Am. Chem. Soc.*, **2002**, *124*, 9034.
16. Y. K. Kang, O.-S. Lee, P. Deria, S. H. Kim, T.-H. Park, D. A. Bonnell, J. G. Saven and M. J. Therien, *Nano Lett.*, **2009**, *9*, 1414-1418.
17. S. Srinivasan, S. S. Babu, V. K. Praveen and A. Ajayaghosh, *Angew. Chem. Int. Ed.*, **2008**, *47*, 5746-5749.
18. A. Star, J. F. Stoddart, D. Steuerman, M. Diehl, A. Boukai, E. W. Wong, X. Yang, S.-W. Chung, H. Choi and J. R. Heath, *Angew. Chem. Int. Ed.*, **2001**, *40*, 1721.
19. Z. Zhang, Y. Che, R. A. Smaldone, M. Xu, B. R. Bunes, J. S. Moore and L. Zang, *J. Am. Chem. Soc.*, **2010**, *132*, 14113-14117.
20. Y. Chen, L. Yu, X.-Z. Feng, S. Hou and Y. Liu, *Chem. Commun.*, **2009**, 4106-4108.
21. W. Cheung, P. L. Chiu, R. R. Parajuli, Y. F. Ma, S. R. Ali and H. X. He, *J. Mater. Chem.*, **2009**, *19*, 6465-6480.

22. S. Jung, M. Cha, J. Park, N. Jeong, G. Kim, C. Park, J. Ihm and J. Lee, *J. Am. Chem. Soc.*, **2010**, *132*, 10964-10966.
23. J. M. Lee, J. S. Park, S. H. Lee, H. Kim, S. Yoo and S. O. Kim, *Adv. Mater.*, **2011**, *23*, 629-633.
24. Y. D. Park, J. A. Lim, J. A. Yunseok, M. Hwang, H. S. Lee, D. H. Lee, H. J. Lee, J. B. Baek and K. Cho, *Organic Electronics*, **2008**, *9*, 317-322.
25. L. Qiu, X. Yang, X. Gou, W. Yang, Z.-F. Ma, G. G. Wallace and D. Li, *Chem. Eur. J.*, **2010**, *16*, 10653-10658.
26. V. Saini, Z. Li, S. Bourdo, E. Dervishi, Y. Xu, X. Ma, V. P. Kunets, G. J. Salamo, T. Viswanathan, A. R. Biris, D. Saini and A. S. Biris, *J. Phys. Chem. C*, **2009**, *113*, 8023-8029.
27. A. Ikeda, Y. Totsuka, K. Nobusawa and J. Kikuchi, *J. Mater. Chem.*,, **2009**, *19*, 5785.
28. I. Ling, Y. Alias, M. Makha and C. L. Raston, *New J. Chem.*, **2009**, *33*, 1583-1587.
29. K. Nobusawa, A. Ikeda, J. Kikuchi, S. Kawano, N. Fujita and S. Shinkai, *Angew. Chem. Int. Ed.*, **2008**, *47*, 4577-4580.
30. M. J. O'Connell, P. Boul, L. M. Ericson, C. Huffman, Y. Wang, E. Haroz, C. Kuper, J. Tour, K. D. Ausman and R. E. Smalley, *Chem. Phys. Lett.*, **2001**, *342*, 265-271.
31. M. Antonietti, *Nature Mater.*, **2003**, *2*, 9-10.
32. V. A. Friese and D. G. Kurth, *Coord. Chem. Rev.*, **2008**, *252*, 199-211.
33. F. J. M. Hoeben, P. Jonkheijm, E. W. Meijer and A. P. H. J. Schenning, *Chem. Rev.*,, **2005**, *105*, 1491-1546.
34. M. Quintana and M. Prato, *Chem. Commun.*, **2009**, 6005-6007.
35. K. Yoosaf, A. Belbakra, N. Armaroli, A. Llanes-Pallas and D. Bonifazi, *Chem. Commun.*, **2009**, 2830-2832.
36. K. Yoosaf, A. Llanes-Pallas, T. Marangoni, A. Belbakra, R. Marega, E. Botek, B. Champagne, D. Bonifazi and N. Armaroli, *Chem.-Eur. J.*, **2011**, *17*, 3262-3273.
37. K. Yoosaf, A. Belbakra, A. Llanes-Pallas, D. Bonifazi and N. Armaroli, *Pure Appl. Chem.*, **2011**, *83*, 899-912.
38. T. Marangoni, S. A. Mezzasalma, A. Llanes-Pallas, K. Yoosaf, N. Armaroli and D. Bonifazi, *Langmuir*, **2011**, *27*, 1513-1523.
39. L. Gobbi, P. Seiler, F. Diederich and V. Gramlich, *Helv. Chim. Acta*, **2000**, *83*, 1711-1723.
40. J. Hua and W. B. Lin, *Org. Lett.*, **2004**, *6*, 861-864.
41. A. Llanes-Pallas, C. A. Palma, L. Piot, A. Belbakra, A. Listorti, M. Prato, P. Samorı`, N. Armaroli and D. Bonifazi, *J. Am. Chem. Soc.*, **2009**, *131*, 509-520.
42. A. Ajayaghosh, R. Varghese, V. K. Praveen and S. Mahesh, *Angew. Chem. Int. Ed.*, **2006**, *45*, 3261 - 3264.
43. F. C. Spano, *Acc. Chem. Res.*, **2009**, *43*, 429-439.
44. A. Llanes-Pallas, M. Matena, T. Jung, M. Prato, M. Stohr and D. Bonifazi, *Angew. Chem. Int. Ed.*, **2008**, *47*, 7726-7730.

Chapter 4

Luminescent hybrids based on carbon nanotubes

4.1 Introduction

Nanomaterials, notable for their small size and potential applications in wide fields such as electronics, industrial and biomedical, and have been attracting a huge interest around the world.[1] Especially, their unique physical and chemical properties due to their small size render them as ideal alternatives for the classic macro-sized materials in the areas of energy and electronics. The impressive part is their tunable and controllable functional properties, either by size selective preparation or by adding new materials to make composites.[1,2] Nanocomposites are another new class of materials, showing the combined properties of two or more individual materials.[2] The importance of these materials has been realized recently and an intense research has been dedicated to design advanced nanocomposites to meet the present energy problems. Carbon nanotubes (CNTs), renowned for their high aspect ratio, large surface area, conductivity, mechanical strength and physio-chemical properties,[3] provide a good platform to develop such next generation materials. Certainly, the combination of CNTs distinct features with organic/inorganic materials can expand the horizons of its applications. Moreover, functionalization of CNTs both through covalent[4-6] or noncovalent strategies,[2] bestows processability, solubility, and control on electronic and optical properties, which are potential characteristics for the growing modern age optoelectronic devices. In this work, we report two hybrid materials, derived from CNTs and lanthanide complexes. The preparation, structural, chemical, optical and photophysical characterization of these materials are discussed in detail.

4.2 A luminescent host-guest hybrid between a Europium(III) complex and MWCNTs

The luminescence performance of a chromophore, in terms of color and intensity, is dramatically dependent on the local chemical environment.[7] Particularly, in the solid state, luminescent molecules tend to undergo aggregation phenomena which profoundly alter their color quality and

reduce emission output, endangering fruitful exploitation for optoelectronic devices.[8] In solution, quenching with high energy O–H, C–H or N–H oscillators belonging to the solubilizing medium (either water or organic solvents) also significantly reduces their performance (ex. Ln(III) emitters) for analytical and technological applications such as contrast agents or bio-imaging.[9,10] A novel approach to address the problems outlined above, relies on the confinement and insulation of the chromophoric units into hollow structures. Both inorganic and organic approaches have been attempted. For instance, inorganic materials such as zeolites,[11] high porosity glass films from sol-gel processes[12] and mesoporous metal oxides[13] have been employed in endohedral functionalisation experiments and, likewise, some organic systems such as calixarenes,[9] cryptands,[14] cyclodextrins,[15] and cucurbiturils.[16]

Beside the preparation of fullerene C_{60} peapods, carbon nanotubes (CNTs) are still largely unexplored as hollow hosting structures, and a relatively limited number of organic guest molecules have been incorporated within.[17-21] Among these, very few scattered examples of encapsulation of organic luminophores have been reported and their Vis-emitting properties investigated.[22,23] In this respect, functionalization of CNTs with strong Vis-emitting chromophores like Eu(III) complexes, would enhance their appeal towards practical exploitation as these materials only exhibit, in some limited cases, infrared (IR) emission.[24] With the aim to prepare stable and easily accessible luminescent Eu/CNT hybrids, endohedral functionalisation of MWCNTs with a neutral and hydrophobic *tris*-hexafluoro acetylacetonate Eu(III) complex (**1**) was performed *via* host-guest hydrophobic interaction (**Scheme 4.2.1**). This work is envisaged to unravel the intimate interaction between the CNTs and the encapsulated Eu(III) complexes, and its influence on the emitting properties of the resulting hybrid material.

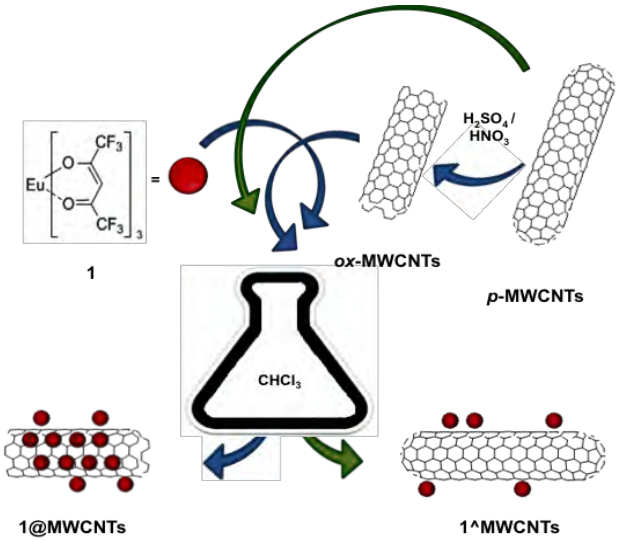

Scheme 4.2.1 *Schematic representation of the nano-extraction technique. The chemical structure of complex* ***1,*** *and possible structure of hybrids* ***1@MWCNTs*** *and* ***1^MWCNTs****.*

4.2.1 Endohedral functionalization of MWCNTs

In order to obtain the desired luminescent hybrid **1@MWCNTs**, *Iijima*'s "nano-extraction" methodology was employed.[18] First, pristine MWCNTs (*p*-MWCNTs) were opened by acid treatment using the oxidizing mixture H_2SO_4/HNO_3 (3:1).[5,25] It is known that, in the course of this procedure, the nanotube ends are functionalized with carboxylic groups, which might hamper efficient encapsulation.[20] Therefore, thermal treatment at 450° C in air for 1 h was used to remove most of these groups. The Eu(III) complex **1** was then dispersed in $CHCl_3$ (4 ml) by ultrasonic treatment for 15 min. Subsequently, powdered *ox*-MWCNTs (10 mg) were added to the saturated solution, before leaving the mixture under gentle stirring at r.t. for 3 days. Filtration on a Millipore apparatus and copious rinsing with $CHCl_3$ afforded the hybrid material as a pellet, which was re-dispersed in $CHCl_3$/MeOH (10:1) and ultrasonicated for 10 minutes to remove all the adsorbed **1** from the CNTs. This purification cycle has been iterated several times, until the washings did not contain any trace of **1**, as detected by emission spectroscopy. In order to evaluate the contribution of externally bound traces of **1** to the luminescent output of **1@MWCNTs**, we also performed the same functionalization procedure using untreated ***p*-MWCNTs**. In this way we obtained hybrid **1^MWCNTs**, the "closed" analogue of **1@MWCNTs** (**Scheme 4.2.1**).

4.2.2 Chemical and microscopic analyses

To determine the atomic composition of the prepared materials, X-ray photoelectron spectroscopy (XPS) elemental analysis was performed. ***p*-MWCNTs** and ***ox*-MWCNTs** presented only the C(1s) and the O(1s) signals, at 284 and 533 eV, respectively (**Table 4.2.1**). An increase in the O/C atomic ratio for ***ox*-MWCNTs** confirmed the effectiveness of the oxidative treatment. The fingerprint signals of **1**, namely Eu(3d) (1134 eV) and F(1s) (686 eV) were detected for **1@MWCNTs**, while the reference hybrid **1^MWCNTs**, exhibited only the C(1s) and the O(1s) signals.

Table 4.2.1 *XPS analysis data for* ***p-MWCNTs***, ***ox-MWCNTs***, ***1@MWCNTs*** *and* ***1^MWCNTs****.*

Samples	C %[a]	O %[a]	F %[a]	Eu %[a]
***p*-MWCNTs**	97.0 ± 1.0	2.0 ± 1.0	-	-
***ox*-MWCNTs**	92.0 ± 2.0	8.0 ± 2.0	-	-
1@MWCNTs	77.2 ± 0.4	9.5 ± 0.3	**13.2 ± 0.7**	**0.1 ± 0.1**
1^MWCNTs	96.2 ± 1.3	3.8 ± 1.2	-	-

[a] Each value is the average of 3 measurements on the sample.

Thermogravimetric analysis (TGA) evidenced another remarkable difference between **1@MWCNTs** and **1^MWCNTs**. Whilst **1^MWCNTs** exhibited only one weight loss event at 240° C, related to the pyrolisis of **1** (**Figure 4.2.1**), **1@MWCNTs** showed a peculiar TGA profile, characterised by three weight loss events. The first one (240° C) corresponds to the decomposition of **1** (**Figure 4.2.1**), whereas the last (800° C) can be assigned to the decomposition of ***ox*-MWCNTs**. The novel central peak (at 450° C, blue box) is attributed to the thermal decomposition of the encapsulated complex, which is expected to possess enhanced stability in the confined environment of MWCNTs, thanks to the multilayered structure of the tubes that can delay pyrolysis. This finding is fully in line with TGA trends of fullerene peapods, in which encapsulated C_{60} shows a higher combustion temperature.[26]

High-resolution transmission electron microscopy (HR-TEM) was also used as a technique to estimate the effectiveness of the encapsulation of **1** within the internal channel of the ***ox*-MWCNTs**. Even though a sizeable focus difference could be expected between luminophores located on top or inside a CNT, this structural characterization turned out to be particularly challenging because of the presence of both externally adsorbed materials (also composed of carbonaceous material present in the CNTs samples deriving from the production process and the oxidative treatments) and encapsulated complex **1**, which often resulted difficult to discern. Therefore, the proof of encapsulation in a given image is mainly obtained *via* morphological evidence. In the case of **1@MWCNTs** (**Figure 4.2.2**), disordered material appears in some of the CNTs present in the sample, which is most probably encapsulated within the tubes as it closely follows the shape of the internal channel. In the case of **1@MWCNTs**, disordered material appears in some of the CNTs of the sample, which is most probably encapsulated within the tubes as it closely seems to follow the shape of their internal channel (**Figure 4.2.2b**). To confirm these findings, HR-TEM measurements were combined with energy dispersive X-ray spectroscopy studies (EDS). This technique allows to obtain information on the local elemental composition and hence the degree of homogeneity of the encapsulated material within the sample. EDS analysis of the region marked with a blue circle, preliminarily assigned to the encapsulated material in the HR-TEM images, unambiguously reports the presence of the signals relative to **1**, namely Eu, F and O.

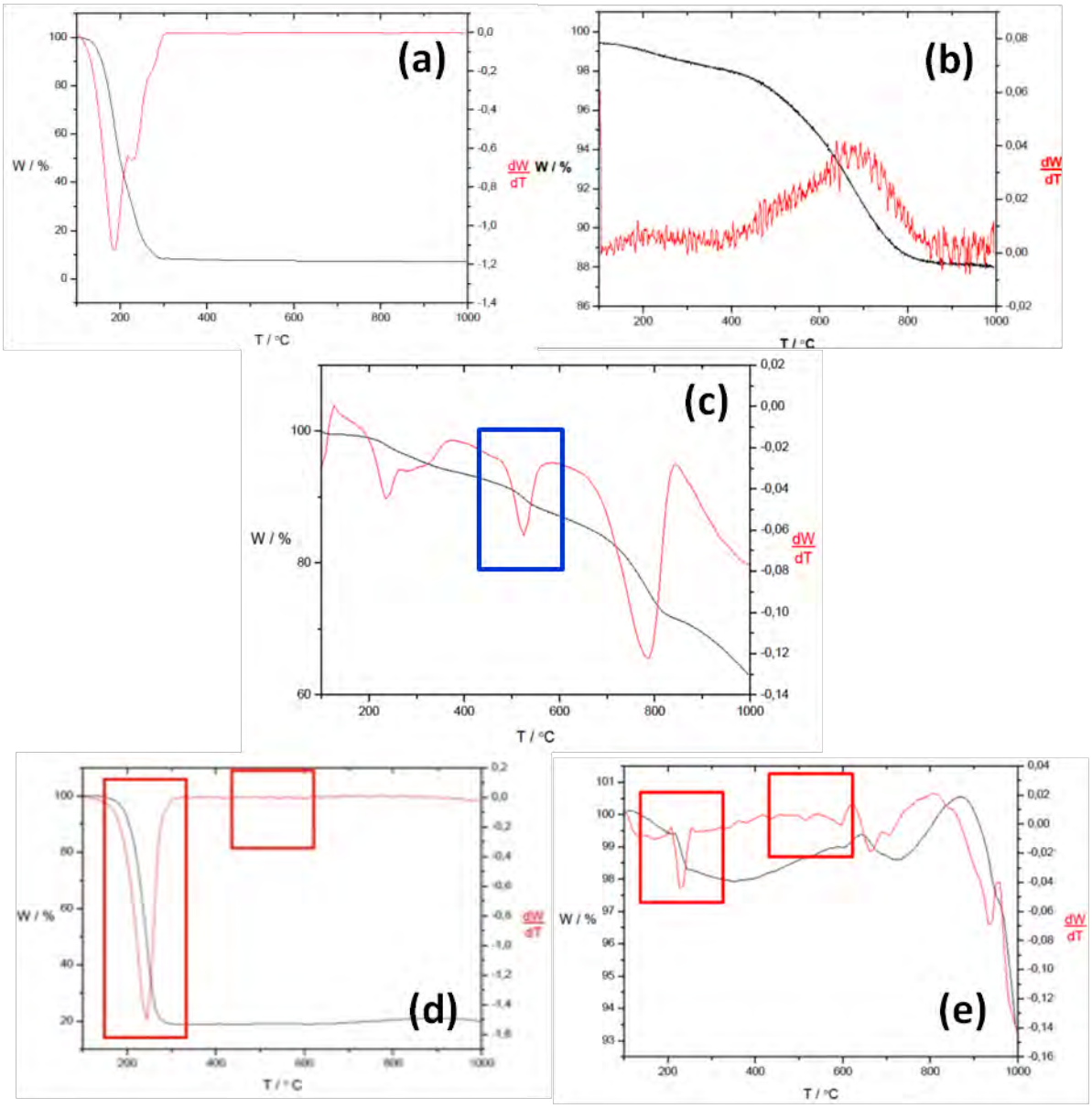

Figure 4.2.1 *Thermogravimetric analysis for* ***1*** *(a),* ***ox-MWCNTs*** *(b),* ***1@MWCNTs*** *(c), unwashed* ***1^MWCNTs*** *(d) and* ***1^MWCNTs*** *(e) performed in N_2 atmosphere with a heating ramp of 10° C / min.*

EDS technique was also important to reveal significant differences between **1@MWCNTs** and **1^MWCNTs**. Several analyses performed throughout **1@MWCNTs** with different dimensions of the electron probe have confirmed the consistent presence of Eu, F and O in the sample. Notably, it was not found in **1^MWCNTs** the same amount of disordered material within the tubes as in the case of **1@MWCNTs**. The detection of Eu on **1^MWCNTs** via EDS resulted rather misleading: in fact, despite having performed analysis on comparable portions of sample as the ones employed for **1@MWCNTs**, the signals of Eu and F were only detected in certain spots (**Figure 4.2.3**), showing a very inhomogeneous distribution of the complex.

A more detailed investigation showed that the Eu signal essentially arises from areas in the sample where small particles were observed at a higher magnification, not to be confused with the numerous smaller dark regions typical of the appearance of edge-on MWCNTs tips. These findings suggest that, in **1^MWCNTs**, most of the Eu complex is mainly adsorbed onto the CNTs external surface, where **1** forms small agglomerated particles as already observed for a similar system.[27]

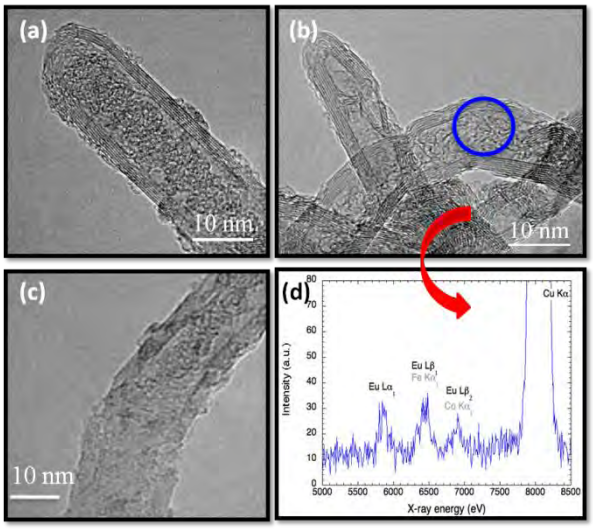

Figure 4.2.2 *HR-TEM images (a-c) of MWCNTs in* ***1@MWCNTs*** *and EDS analysis spectra relative to panel (b). The blue circle marks the position and dimension of the electron beam used for the corresponding EDS analyses reported.*

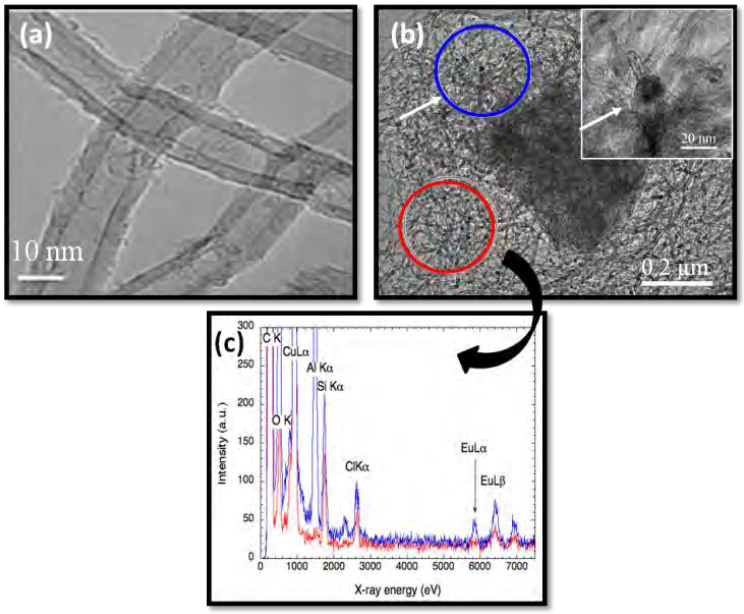

Figure 4.2.3 *(a) HR-TEM image of* ***1^MWCNTs****, showing the presence of some filaments on the tubes but never a more important agglomerate of disordered material as in the case of* ***1@MWCNTs****. (b) HR-TEM image of* ***1^MWCNTs*** *bulk, and (c) EDS spectra taken at the red and blue circled areas in (b).*

4.2.3 Photophysical characterization

photophysical studies on **1**, **1@MWCNTs** and **1^MWCNTs** in the solid state were accomplished. Excitation of **1** and **1@MWCNTs** at 300 nm, corresponding to the absorption maximum of the chelating ligands of **1**, results in the characteristic emission spectrum of the Eu(III) ion, with several sharp emission features between ~570 and 720 nm (**Figure 4.2.4**).[9,10,28,29] By contrast, no Eu(III)-centered emission is detected from **1^MWCNTs**, demonstrating the absence of a significant quantity of **1** in the sample. As a further reference for luminescence studies, a sample of unwashed **1^MWCNTs** (***u*-1^MWCNTs**) was also investigated, to emphasize possible peculiar effects on the luminescence output of **1** upon confinement.

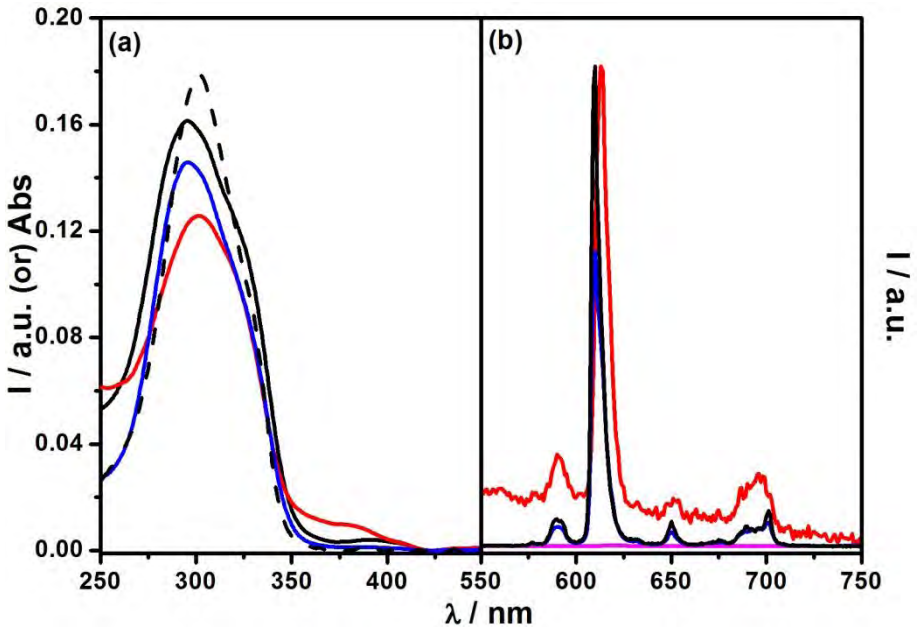

Figure 4.2.4 *(a) Excitation (λ_{em} = 616 nm) and (b) emission (λ_{ex} = 300 nm) spectra of **1** (black), **1@MWCNTs** (red), **u-1^MWCNTs** (blue) and **1^MWCNTs** (magenta) in the solid state. The black dashed line in (a) is the absorption spectrum of **1** in CH_2Cl_2. The weak emission spectrum of **1@MWCNTs** (see text) is normalized to that of **1** at the highest peak.*

Excitation spectra of **1@MWCNTs** and ***u*-1^MWCNTs**, recorded at the most intense emission peaks, match the corresponding spectrum of **1** as well as its absorption profile. This observation shows that an efficient energy transfer from the acetylacetonate "antenna" ligands of **1** to the emitting Eu(III) metal ion occurs and, most importantly, suggests the presence of **1** in both **1@MWCNTs** and ***u*-1^MWCNTs**. This is further supported by the emission spectra collected upon excitation at different wavelengths, including the absorption maxima of the Eu(III) metal ion itself (394 and 465 nm).[30] No emission was observed from **1@MWCNTs**, by

predominantly exciting the metal ion, confirms that the encapsulation of **1** into MWCNTs did not alter its coordination sphere and Eu(III) exists only in complex form and not as ionic clusters.

The Eu(III) emission features of **1**, **1@MWCNTs** and ***u*-1^MWCNTs** arise from $^5D_0 \rightarrow {}^7F_J$ (J = 0-4) *f-f* electronic transitions.[9,10,28] Among others, electric ($^5D_0 \rightarrow {}^7F_2$) and magnetic ($^5D_0 \rightarrow {}^7F_1$) dipolar transitions are predominant at about 610-625 and 585-600 nm, respectively. Notably, although the emission spectra of **1**, **1@MWCNTs**, and ***u*-1^MWCNTs** are similar, differences are observable by comparing the emission intensity ratio of $^5D_0 \rightarrow {}^7F_2$ and $^5D_0 \rightarrow {}^7F_1$ transitions (18, 9, and 16 for **1**, **1@MWCNTs** and ***u*-1^MWCNTs** respectively), which indicates some substantial difference in the symmetry, and thus chemical environment, of the emitting complex in the case of **1@MWCNTs**.[31] This result is corroborated by the position of the hypersensitive[32-34] electric dipolar $^5D_0 \rightarrow {}^7F_2$ transition, which is 613 nm for **1@MWCNTs** and 610 nm for **1** and **1^MWCNTs**. The red shift of the emission maximum of **1@MWCNTs** can be attributed to a change in electric dipole moment of the encapsulated complex, probably related to an increase in the symmetry of the environment in which **1** is placed.

The effect of the interaction of **1** in **1@MWCNTs** and ***u*-1^MWCNTs** with MWCNTs is further observable from the trend of the emission lifetimes. Luminescence decays of the Eu(III) complex can be fitted monoexponentially in the case of pristine **1** and **1@MWCNTs**, yielding values of 0.70 and 0.45 ms respectively. On the contrary, the decay trace of ***u*-1^MWCNTs** is bi-exponential with a predominant value of 0.82 ms and a minor component of 0.32 ms. The more complex pattern observed for ***u*-1^MWCNTs** is interpreted as a consequence of the less homogeneous environment experienced by the luminophores placed at the external interface of the carbon material made of graphitic walls, local defects and functionalized extremities. The monoexponential lifetime value of **1** and **1@MWCNTs** suggests more isotropic surroundings.

The Eu(III) photoluminescence quantum yields (Φ_{Eu}) of **1**, **1@MWCNTs** and ***u*-1^MWCNTs** have been estimated by using eq. (1), where τ_{obs} is the observed (*i.e.* measured) lifetime and τ_{rad} is the radiative lifetime:[10,28]

$$\Phi_{Eu} = \frac{\tau_{obs}}{\tau_{rad}} \quad (1)$$

τ_{rad} can be estimated theoretically from the corrected emission spectra of the Eu(III) complexes, using eq. (2):[10,28]

$$\frac{1}{\tau_{rad}} = A_{MD,0}\ n^3\ \left\{\frac{[I_{tot}]}{[I_{MD}]}\right\} \quad (2)$$

where $A_{MD,0}$ is the probability of the spontaneous $^5D_0 \rightarrow {}^7F_1$ deactivation (14.65 s^{-1}),[10,28] n is the refractive index of the medium (air, 1.0008), I_{tot} is the area of Eu(III) centered corrected emission

spectrum and I_{MD} is the area of the $^5D_0$ – $^7F_1$ band. The higher Φ_{Eu} (0.17, 0.07, and 0.20 for **1**, **1@MWCNTs** and ***u*-1^MWCNTs**, respectively) and longer lifetime of ***u*-1^MWCNTs**, compared to **1**, is attributed to a decrease in vibrational relaxation of the excited states of the ligands, probably due to their proximity to the rigid structure of the MWCNTs' framework.

The weak emission intensity of **1@MWCNTs** can either be due to (i) unfavourable partitioning of light excitation between the Eu(III) complex and the MWCNTs, (ii) re-absorption of the emitted light by the MWCNTs themselves, and (iii) moderate filling of the complex inside MWCNTs. Despite these problems, the intrinsic ⊠$_{Eu}$ of the encapsulated Eu(III) complex remains substantially high (7%). The 60% decrease of this value compared to that of **1** is attributed to a reduced efficiency of the energy transfer from the ligands to Eu(III) ions, as a consequence of the quenching of the ligand triplet state by the nanotube walls.[35] Moreover, the reduced relative intensity of the electric dipolar transition band suggests a symmetry increase of the Eu(III) complex in **1@MWCNTs**.

4.2.4 Summary

Several experimental techniques provided concerted evidence for the encapsulation of a suitably designed luminescent Eu(III) complex inside MWCNTs and, despite some quenching, the luminescence quantum yield of the selected luminophore remains reasonably high (~7%). To the best of our knowledge, these results are the first proof of principle that Vis-emitting host-guest MWCNTs hybrids obtained upon encapsulation of a luminescent metal complex can be prepared. In perspective, appropriate organic functionalization of the external carbon wall and optimization of the filling procedure could lead to a brand new class of novel Vis-emitting CNTs-based materials exploitable for biomedical or bio-diagnostic applications, possibly representing a novel non-toxic and practical tool to track and check the effectiveness of new therapies.

4.3 Electrostatically-driven assembly of Europium(III) complexes on MWCNTs

Amongst the myriad of potential applications of CNTs, their use in the field of biotechnology has recently started to emerge, raising great expectations.[36,37] Surface functionalization enables CNTs to be easily employed as versatile molecular modules for the adsorption or attachment of various biological-active molecules or antigens, which subsequently can be targeted to the desired cell population for immune recognition or therapeutic effects.[38,39] Concerning the biomedical applications of CNTs, their use is becoming relevant in neuroscience research and tissue engineering.[40,41] For example, they have been employed as supports for neuronal and ligamentous tissue growth for regenerative interventions of the central nervous system (e.g., brain and spinal cord).[41] Although safety issues have still to be thoroughly examined, all these findings pave the way for the development of novel CNT-based materials which could lead to new insights into the biological and physical processes in which such carbon nanostructure are involved.

Due to their exceptional luminescence properties, complexes of lanthanide trivalent ions, Ln(III), have attracted a lot of interest in a large spectrum of important electronic and bio-technological fields.[10,28,42,43] For instance, emitting complexes of Tb(III) and Eu(III) ions are employed as markers in fluoro-immunoassay where a quantitative estimate of antigens in biological matrices is needed.[43] Due to their strong and long-lived luminescence, the background signal from the biological matrix can be circumvented making particularly easy the detection of the desired analytical signal. Moreover, most of the research involved in the engineering of a new-generation of *in-vivo* imaging technologies requires low-frequency light due to its penetration capability through biological tissues. To this end, NIR luminescent trivalent cations such as Yb(III), Nd(III), Pr(III), Er(III), and related complexes are particularly attractive.[44,45] These rare earth systems have also found a variety of applications in other fields such as optical amplifiers in laser technologies (e.g., Nd(III)) or in silica-based fibers for optical networks, where the emission wavelengths of Pr(III) (ca. 1330 nm) and Er(III) (ca. 1550 nm) ions closely match the "windows of transparency" in silica used for telecommunications.[46]

The blend of both CNTs and Ln(III) complexes could fetch a novel material with luminescent properties of Ln(III) ion, and electronic and mechanical properties of CNTs. In this regard, in a previous work we have reported a simple method to prepare luminescent CNTs composites by *in-situ* adsorption of a Lanthanide complex (LnC) onto oxidized SWCNTs *via* hydrophobic interaction from a MeOH solution. Though this was the breakthrough in the field of luminescent materials, desorption of the LnC from CNTs surface and the difficulty to control the loading of the complex, turned out to be the main limitations toward the technological

exploitation of this luminescent material. Hence, we developed a new strategy to produce a new class of luminescent materials in which the emissive species are non-covalently adsorbed on the CNTs' outer surface through strong interactions.[47]

4.3.1 Layer-by-layer assembly of a Eu(III) complex on MWCNTs

Inspired by the columbic-directed layer-by-layer methodology,[48] we have envisaged assembling negatively-charged LnCs onto cationic MWCNTs. Among the different possibilities, anionic Eu(III) complexes are good candidates as it has been showed that they can be electrostatically coupled to ionic liquids (ILs) as displayed by X-ray crystallography. This has been further confirmed by recent independent reports by the groups of *Binnemans*[49] and *Gonçalves*,[50] who have confined a tetrakis(2-naphtoyltrifluoro-acetonato)Eu(III) complex ($[\mathbf{EuL_4}]^-$) on silica supports through columbic interactions, showing improved luminescence properties. In this work, we thus report on the covalent and non-covalent functionalization of MWCNTs with imidazolium-based[51] ILs (**1·Br**), bearing a terminal azido function, which can undergo selective adsorption (**Scheme 4.3.1**) with a negatively-charged europium complex, through anion exchange reaction with a precursor $\mathbf{[EuL_4]{\cdot}NEt_4}$ complex. The synthetic pathways to obtain the luminescent materials are shown in **Scheme 4.3.1**.

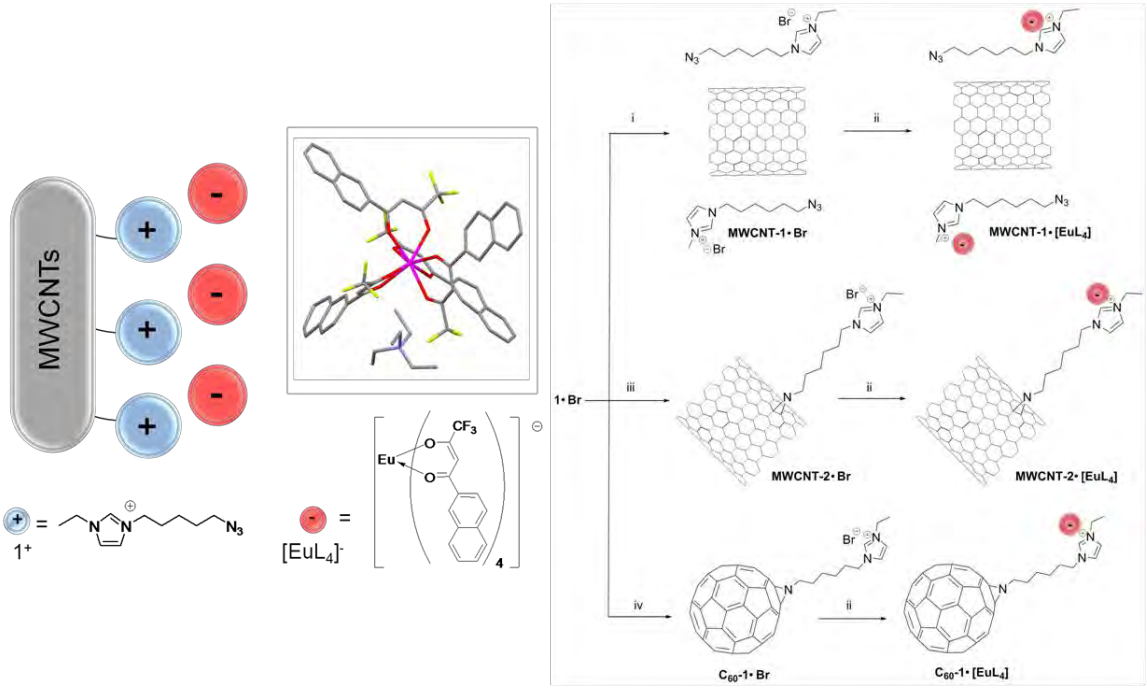

Scheme 4.3.1 *Left: Representation of electrostatically-driven self-assembly on MWCNTs. Inset: X-ray structure of precursor* $\mathbf{[EuL_4]{\cdot}NEt_4}$ *complex; Right: Synthetic scheme for the preparation of* ***MWCNT-1,2·[EuL$_4$]*** *and* ***C$_{60}$-1·Br****. Reagents and conditions: i,* ***p-MWCNTs****, mesitylene, 170°C, 1 h; ii,* $\mathbf{[EuL_4]{\cdot}NEt_4}$*, toluene, r.t., 14 hrs;*

iii, ***p-MWCNTs****, mesitylene, 170°C, 14 hrs and sonication in DMF; iv,* C_{60}*, mesitylene/DMSO (1:1), 140°C, 14 hrs, 30%.*

In a typical experiment, pristine MWCNTs (**p-MWCNT**) were first dispersed in a solution of **1·Br** (20-fold excess) in mesitylene by ultrasonication. The mixture was heated at 170° C to obtain a homogeneous solution of **1·Br**. After 1 h no covalent functionalization of the MWCNTs was observed; impressingly a uniform IL-coated material (**MWCNT-1·Br)** was instead obtained. Prolongation of the reaction to 14 hrs in the same conditions, finally allowed the covalent grafting of the N_3-terminating ILs trough 1,3-dipolar cycloaddition reaction, leading to **MWCNT-2·Br**. Cycles of sonication in DMF were necessary to remove unbounded **1·Br** (see SI). In order to perform the anion exchange reaction, **$[EuL_4]\cdot NEt_4$** (10-fold excess) was added to a dispersion of IL-bearing carbon structure in toluene and stirred for 14 hrs at r.t.

4.3.2 Chemical and photophysical analyses

To elucidate the chemical composition of the functionalized material (see **Table 4.3.1**), XPS studies were undertaken. The elemental analysis of the **p-MWCNTs**, as expected, presents only the C(1s) and the O(1s) signals, which appear at 284 and 533 eV, respectively. Whilst in the case of the covalent material only a small functionalization was obtained (see **Table 4.3.1**).

Table 4.3.1 *XPS analysis results of* ***p-MWCNT****,* ***MWCNT-1,2·Br*** *and* ***MWCNT-1,2·[EuL$_4$]****.*

Sample	C%	O%	N%	F%	Eu%
p-MWCNTs	97 ± 1	2 ± 1	-	-	-
MWCNTs-1·Br	73 ± 3	6 ± 2	12 ± 2	-	-
MWCNTs-2·Br	92.8 ± 0.3	6.3 ± 0.3	0.6 ± 0.1	-	-
MWCNTs-1·[EuL$_4$]	75.2 ± 0.3	11 ± 1	1.8 ± 0.3	11 ± 2	11 ± 2
MWCNTs-2·[EuL$_4$]	90.9 ± 0.8	6.6 ± 0.7	0.7 ± 0.5	1.7 ± 0.1	0.02
Blank test[b]	94 ± 1	11.6 ± 0.9	-	-	-

[b]*Blank test: physical dispersion of MWCNTs with* ***[EuL$_4$]·NEt$_4$*** *after extensive washing in the absence of the ionic liquid functionalities*

More interesting results are obtained from the non-covalently functionalized material. In fact, in the case of **MWCNT-1·Br,** the signal of N(1s) centered at 401 eV, indicating the presence of both the azyridyl ring and the imidaziolium functionality in the sample; the high (12%) atomic

ratio of the latter element revealing an unprecedented loading of the sample on MWCNTs. The luminescent hybrid assembly **MWCNT-1·[EuL$_4$]**, presents signals relative to the anionic complex centered on the Eu(3d) (1134 eV) and F(1s) (686 eV), with atomic percentages of 0.5 and 11% respectively. The amount of F atoms found in the sample is higher than the expected value (considering the structure of **[EuL$_4$]$^-$**, a ratio of 1:12 should be detected), indicating the presence of some free ligand **L**, probably deriving from some decomposition of the complex or some external F-containing impurities.[52] No Br-centered resonances have been detected, evidencing the effectiveness of the anion exchange reaction.

The degree of functionalization of the materials has been also investigated *via* thermogravimetric analysis (TGA) in air. While for **MWCNT-2·Br** and **MWCNT-2·[EuL$_4$]** no defined weight loss has been observed due to the low degree of functionalization, in the case of **MWCNT-1·Br** and **MWCNT-1·[EuL$_4$]**, the TGA curves show a sharp weight loss of about 80% and 60% at 600°C, respectively, as compared to the **p-MWCNTs**. The apparent reduced weight loss for **MWCNT-1·[EuL$_4$]** as compared to **MWCNT-1·Br** is caused by the presence of Eu(III) atoms, which undergo an oxidation reaction during the combustion, leading to oxides.

In order to prove the electrostatic interaction in solution between functionalized **MWCNT-1·Br** and **[EuL$_4$]·NEt$_4$**, luminescence titrations were carried out with the model compound **C$_{60}$-1·Br**.[53] Due to the poor solubility of MWCNTs, it is not possible to carry out reliable optical spectroscopic measurements in solution. Thus, emission titrations were performed with the soluble model derivative **C$_{60}$-1·Br**. Aliquot amounts of **[EuL$_4$]·NEt$_4$** were added to 2.3×10^{-5} M solution of **C$_{60}$-1·Br** in CH_2Cl_2 and luminescence spectra and lifetimes were recorded after each addition. By increasing the concentration of **[EuL$_4$]·NEt$_4$**, first an increase (up to 0.8 equivalents) and then a decrease of Eu(III)-centered emission is observed (**Figure 4.3.1**).

To understand this trend, a blank titration experiment was carried out by increasing the concentration of **[EuL$_4$]·NEt$_4$** alone in CH_2Cl_2, in the absence of **C$_{60}$-1·Br**; an identical pattern of the emission signal was recorded. This showed that the weird emission intensity trend observed is not due to the interaction of **[EuL$_4$]·NEt$_4$** with **C$_{60}$-1·Br** but just to concentration-related optical artifacts.[54] Interestingly, even a single addition of **[EuL$_4$]·NEt$_4$** (0.1 eq) to **C$_{60}$-1·Br** resulted in quenching of the excited state lifetime of **[EuL$_4$]·NEt$_4$** from 0.53 ms to 0.20 ms. On the contrary, titration experiments carried out by adding aliquot amounts of **C$_{60}$-1·Br** in a solution 3.4×10^{-7} M of **[EuL$_4$]·NEt$_4$** resulted in a continuous decrease of the lifetime up to the value of 0.25 ms (**Figure 4.3.2**). A test experiment with uncharged pristine C_{60} gave a longer lifetime of 0.35 ms at the highest concentration level (**Figure 4.3.1b**), as a consequence of diffusional quenching.

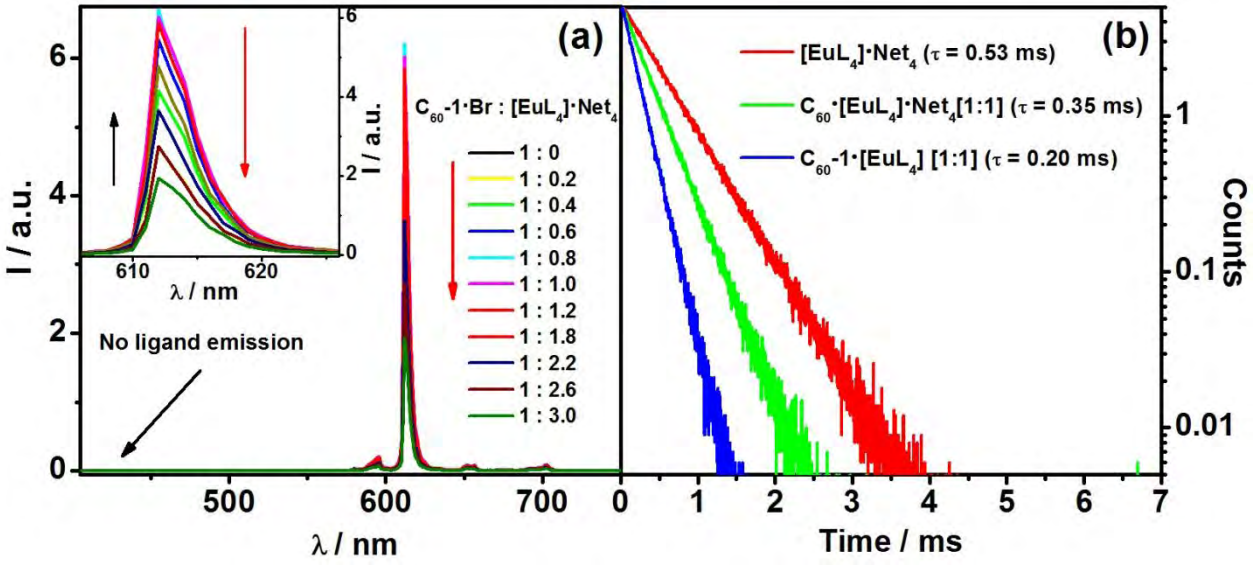

Figure 4.3.1 (a) *Emission spectra of* ***C_{60}-1·Br*** *in presence of increasing amounts of* ***[EuL$_4$]·NEt*** *in CH_2Cl_2. Inset shows the changes in the Eu(III) centered emission maximum.* ***(b)*** *Emission decay profiles of* ***C_{60}-1·Br,*** ***[EuL$_4$]·NEt$_4$,*** *a mixture of* ***C_{60}*** *and* ***[EuL$_4$]·NEt$_4$*** *(1:1), and a mixture of* ***C_{60}-1·Br*** *and* ***[EuL$_4$]·NEt$_4$*** *(1:1). Emission spectral changes were recorded with λ_{exc} = 370 nm and emission decay profiles were collected with excitation at 370 nm and monitoring at 612 nm.*

These results suggest the existence of an interaction between **C_{60}-1·Br** and **[EuL$_4$]·NEt$_4$** which, albeit reducing the excited state lifetime of the emitter, preserves an intense luminescence signal. Notably, within the experimental error, no changes have been observed when luminescence titrations of **[EuL$_4$]·NEt$_4$** were carried out with the imidazolium linker molecule, namely **1·Br**.

The luminescence properties of **MWCNT-1·[EuL$_4$]** were also investigated. **MWCNT-1·[EuL$_4$]** resulted a bright red luminescent material (upon UV excitation) whose optical properties could be investigated only in the solid state (KBr matrix) due to its poor solubility (**Figure 4.3.2**). This material showed an intense and sharp emission peak at 615 nm and weaker features at 593, 654 and 702 nm, characteristic of Eu(III) ions. The excitation spectrum in the solid state, matches the excitation spectrum of the complex alone (**Figure 4.3.2**). The solid state luminescence quantum yield and excited state lifetime of **MWCNT-1·[EuL$_4$]** were measured as 0.44 and 0.29 ms respectively, in accordance with data of the complex [EuL$_4$]·NEt$_4$ in KBr (Φ_f = 0.44 and τ_f = 0.28 ms), which suggests high loading of the luminophore on the surface of MWCNTs through the non-covalent interactions.

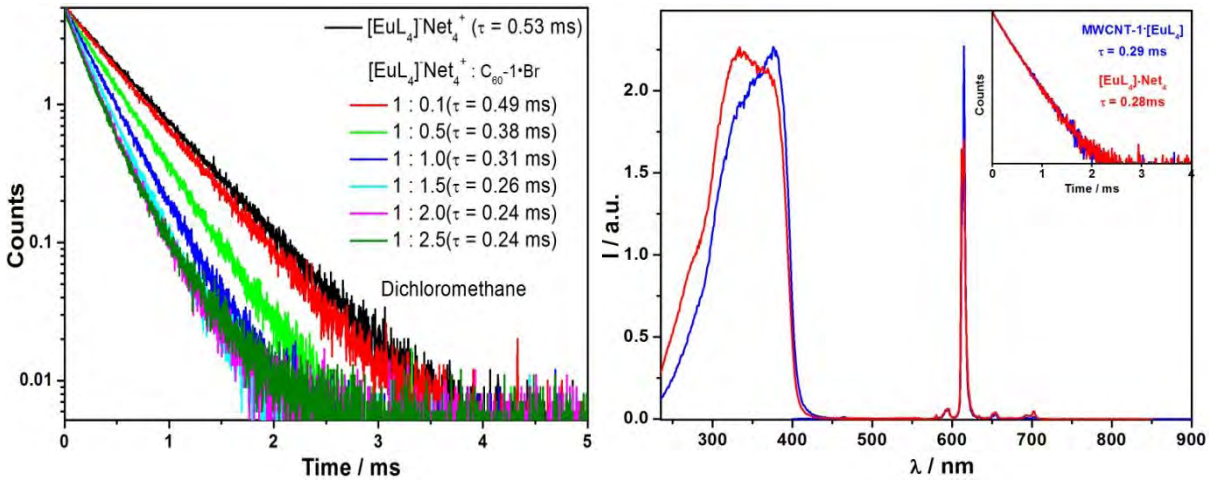

Figure 4.3.2 *Left: luminescence decay profiles of* ***[EuL$_4$]·Net$_4$*** *[3.4 x 10^{-6} M] in presence of various concentration of* ***C$_{60}$-1·Br*** *[0 – 8.5 x 10^{-6} M] in CH_2Cl_2. The decay profiles were collected at 612 nm upon exciting at 370 nm; Right: Excitation (λ_{em}= 612 nm) and emission (λ_{exc}= 370 nm) spectra in the solid state (KBr disc)* ***MWCNT-1·[EuL$_4$]*** *(blue) and* ***[EuL$_4$]·Net$_4$*** *(red); inset shows the corresponding emission decay profiles.*

4.3.3 Microscopic analysis

The composite material **MWCNT-1·[EuL$_4$]** was also characterized using confocal laser scanning microscopy (CLSM), **Figure 4.3.3**. Measurements of $CHCl_3$ dispersions containing **MWCNT-1·[EuL$_4$]** spin-coated onto microscopic glass slides, revealed the presence of bright luminescent particles with size ≤5 μm. Spectral measurements confirmed that they are due to Eu(III)-centered luminescence (**Figure 4.3.3**).

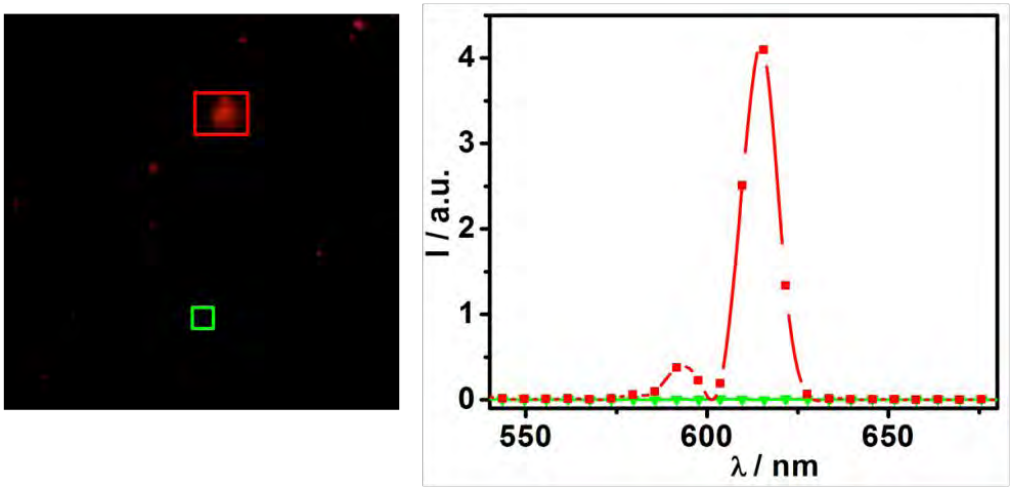

Figure 4.3.3 *Left: confocal image of spin-coated* ***MWCNT-1·[EuL$_4$]*** *onto glass substrate; Right: emission spectra recorded from bright particles (red box) and background (green box); Confocal images were recorded after exciting with 400 nm laser and the emission signal was collected by using a 450 nm cut-off filter*

4.3.4 Summary

Eventually, a simple method for the non-covalent coating of MWCNTs with rare earth luminophores through electrostatic interactions is reported. The electrostatic interaction between the ionic liquid and the luminescent Eu(III) complex has been proved unambiguously by the photophysical studies. Importantly, the intense luminescence of the rare earth metal ion is largely preserved in the non-covalently prepared hybrid material. These newly-designed emissive hybrid CNTs-based materials could open the way to original approaches for the design of electroluminescent devices (OLED, LEC) where the presence of the carbon material could provide substantial improvement of the mechanical and charge conductivity properties of the active layers within devices.

4.4 References

1. C. N. R. Rao and A. K. Cheetham, *J. Mater. Chem.*, **2001**, *11*, 2887-2894.
2. D. Eder, *Chem. Rev.*, **2010**, *110*, 1348-1385.
3. R. A. Hatton, A. J. Miller and S. R. P. Silva, *J. Mater. Chem.*, **2008**, *18*, 1183-1192.
4. M. Prato, K. Kostarelos and A. Bianco, *Acc. Chem. Res.*, **2008**, *41*, 60-68.
5. P. Singh, S. Campidelli, S. Giordani, D. Bonifazi, A. Bianco and M. Prato, *Chem. Soc. Rev.*, **2009**, *38*, 2214-2230.
6. D. Tasis, N. Tagmatarchis, A. Bianco and M. Prato, *Chem. Rev.*, **2006**, *106*, 1105-1136.
7. J. R. Lakowicz, *Principles of fluorescence spectroscopy - Third edition*, Springer, New York, 2006.
8. M. Shimizu and T. Hiyama, *Chem. Asian J.*, **2010**, *5*, 1516-1531.
9. J. P. Leonard, C. B. Nolan, F. Stomeo and T. Gunnlaugsson, *Top. Curr. Chem.*, **2007**, *281*, 1-43.
10. D. Parker and J. A. G. Williams, *J. Chem. Soc.-Dalton Trans.*, **1996**, 3613-3628.
11. G. Calzaferri, S. Huber, H. Maas and C. Minkowski, *Angew. Chem. Int. Ed.*, **2003**, *42*, 3732-3758.
12. L. Armelao, S. Quici, F. Barigelletti, G. Accorsi, G. Bottaro, M. Cavazzini and E. Tondello, *Coord. Chem. Rev.*, **2010**, *254*, 487-505.
13. H. Maas, A. Currao and G. Calzaferri, *Angew. Chem. Int. Ed.*, **2002**, *41*, 2495-2497.
14. N. Sabbatini, M. Guardigli and J. M. Lehn, *Coord. Chem. Rev.*, **1993**, *123*, 201-228.
15. J. M. Haider and Z. Pikramenou, *Chem. Soc. Rev.*, **2005**, *34*, 120-132.
16. L. Isaacs, *Chem. Commun.*, **2009**, 619-629.
17. F. Simon, H. Kuzmany, H. Rauf, T. Pichler, J. Bernardi, H. Peterlik, L. Korecz, F. Fülöp and A. Jánossy, *Chem. Phys. Lett.*, **2004**, *383*, 362-367.
18. M. Yudasaka, K. Ajima, K. Suenaga, T. Ichihashi, A. Hashimoto and S. Iijima, *Chem. Phys. Lett.*, **2003**, *380*, 42-46.
19. A. N. Khlobystov, D. A. Britz and G. A. D. Briggs, *Acc. Chem. Res.*, **2005**, *38*, 901-909.

20. A. N. Khlobystov, D. A. Britz, J. Wang, S. A. O'Neil, M. Poliakoff and G. A. D. Briggs, *J. Mater. Chem.*, **2004**, *14*, 2852-2852.
21. M. Monthioux, *Carbon*, **2002**, *40*, 1809-1823.
22. M. Kalbáč, L. Kavan, S. Gorantla, T. Gemming and L. Dunsch, *Chemistry – A European Journal*, *16*, 11753-11759.
23. M. A. Loi, J. Gao, F. Cordella, P. Blondeau, E. Menna, B. Bartova, C. Hebert, S. Lazar, G. A. Botton, M. Milko and C. Ambrosch-Draxl, *Adv. Mater.*, **2010**, *22*, 1635-1639.
24. M. J. O'Connell, S. M. Bachilo, C. B. Huffman, V. C. Moore, M. S. Strano, E. H. Haroz, K. L. Rialon, P. J. Boul, W. H. Noon, C. Kittrell, J. Ma, R. H. Hauge, R. B. Weisman and R. E. Smalley, *Science*, **2002**, *297*, 593-596.
25. J. Li and Y. Zhang, *Appl. Surf. Sci.*, **2006**, *252*, 2944-2948.
26. M. Zhang, M. Yudasaka, S. Bandow and S. Iijima, *Chem. Phys. Lett.*, **2003**, *369*, 680-683.
27. G. Accorsi, N. Armaroli, A. Parisini, M. Meneghetti, R. Marega, M. Prato and D. Bonifazi, *Adv. Funct. Mater.*, **2007**, *17*, 2975-2982.
28. J. C. G. Bunzli, *Chem. Rev.*, **2010**, *110*, 2729-2755.
29. F. S. Richardson, *Chem. Rev.*, **1982**, *82*, 541-552.
30. I. Billard, S. Mekki, C. Gaillard, P. Hesemann, G. Moutiers, C. Mariet, A. Labet and J. C. G. Bunzli, *Eur. J. Inorg. Chem.*, **2004**, 1190-1197.
31. A. P. Bassett, S. W. Magennis, P. B. Glover, D. J. Lewis, N. Spencer, S. Parsons, R. M. Williams, L. De Cola and Z. Pikramenou, *J. Am. Chem. Soc.*, **2004**, *126*, 9413-9424.
32. C. Jorgensen and B. R. Judd, *Mol. Phys.*, **1964**, *8*, 281-290.
33. A. F. Kirby, D. Foster and F. S. Richardson, *Chem. Phys. Lett.*, **1983**, *95*, 507-512.
34. G. Ligner, R. Mohan, S. Knittel and G. Duportail, *Spectrochim. Acta, Part A*, **1990**, *46*, 797-802.
35. K. Yanagi, K. Iakoubovskii, S. Kazaoui, N. Minami, Y. Maniwa, Y. Miyata and H. Kataura, *Phys. Rev. B.*, **2006**, *74*.
36. A. Bianco, K. Kostarelos, C. D. Partidos and M. Prato, *Chem. Commun.*, **2005**, 571-577.
37. A. Bianco and M. Prato, *Adv. Mater.*, **2003**, *15*, 1765-1768.
38. D. Pantarotto, R. Singh, D. McCarthy, M. Erhardt, J. P. Briand, M. Prato, K. Kostarelos and A. Bianco, *Angew. Chem. Int. Ed.*, **2004**, *43*, 5242-5246.
39. G. Pastorin, W. Wu, S. Wieckowski, J. P. Briand, K. Kostarelos, M. Prato and A. Bianco, *Chem. Commun.*, **2006**, 1182-1184.
40. H. Hu, Y. C. Ni, V. Montana, R. C. Haddon and V. Parpura, *Nano Lett.*, **2004**, *4*, 507-511.
41. V. Lovat, D. Pantarotto, L. Lagostena, B. Cacciari, M. Grandolfo, M. Righi, G. Spalluto, M. Prato and L. Ballerini, *Nano Lett.*, **2005**, *5*, 1107-1110.
42. J.-C. G. Bünzli, *Acc. Chem. Res.*, **2006**, *39*, 53-61.
43. J.-C. G. Bünzli and C. Piguet, *Chem. Soc. Rev.*, **2005**, *34*, 1048-1048.
44. G. M. Davies, H. Adams, S. J. A. Pope, S. Faulkner and M. D. Ward, *Photochem. Photobiol. Sci.*, **2005**, *4*, 829-834.

45. J. M. Herrera, S. J. A. Pope, H. Adams, S. Faulkner and M. D. Ward, *Inorg. Chem.*, **2006**, *45*, 3895-3904.
46. N. M. Shavaleev, S. J. A. Pope, Z. R. Bell, S. Faulkner and M. D. Ward, *Dalton Trans.*, **2003**, 808-814.
47. D. L. Shi, J. Lian, W. Wang, G. K. Liu, P. He, Z. Dong, L. M. Wang and R. C. Ewing, *Adv. Mater.*, **2006**, *18*, 189-193.
48. D. M. Guldi, F. Pellarini, M. Prato, C. Granito and L. Troisi, *Nano Lett.*, **2002**, *2*, 965-968.
49. K. Lunstroot, K. Driesen, P. Nockemann, C. Gorller-Walrand, K. Binnemans, S. Bellayer, J. Le Bideau and A. Vioux, *Chem. Mater.*, **2006**, *18*, 5711-5715.
50. S. M. Bruno, R. A. S. Ferreira, F. A. A. Paz, L. D. Carlos, M. Pillinger, P. Ribeiro-Claro and I. S. Goncalves, *Inorg. Chem.*, **2009**, *48*, 4882-4895.
51. F. Meyer, J. M. Raquez, O. Coulembier, J. De Winter, P. Gerbaux and P. Dubois, *Chem. Commun.*, **2010**, *46*, 5527-5529.
52. F-containing impurities are often observed when Teflon pins arae used to manipulate the sample.
53. Due to the poor solubility of MWCNTs, it is not possible to carry out reliable optical spectoscopy in solition. Thus, emission titrations were performed with the soluble model derivative C_{60}-1•Br
54. A. Credi and L. Prodi, *Spectrochimica Acta Part a-Molecular and Biomolecular Spectroscopy*, **1998**, *54*, 159-170.

Chapter 5

Porphyrin-Carbon nanostructure conjugates

Photovoltaic devices (PV) have attracted the highest attention as alternative electricity generators, as the conventional energy resources of the present days are in their limits.[1] The solar PV devices belong to three main classes: inorganic (*e.g.* silicon), organic (*e.g.*, bulk-heterojunction cells) and photoelectrochemical cells (*e.g.*, dye sensitized solar cells). Amongst those, organic photovoltaic (OPV) systems[2,3] are prepared by cheap solution-based methods and offer high mechanical flexibility for preparing low-cost versatile and large photovoltaic surfaces. In these devices, photoinduced charge separation processes occur at the interface between two distinct materials, namely an electron-donor (D) and an electron-acceptor (A). The interface between these two materials constitutes the analogue of the "inorganic" semiconductor p-n junctions. State-of-the-art organic solar cells are made with disordered bulk heterojunctions, in which electron-donor and -acceptor molecules are intimately mixed to form an interpenetrating phase network at the nanoscale level.[4] The performance of such solar cells dramatically depends on the nanomorphology of the donor-acceptor hybrids and by the layer conductivity. At present, bulk heterojunction OPV cells have still a limited stability and a low efficiency (around 8% at their best),[5] if compared to their inorganic analogues. The low efficiency is mainly due to the fact that the average distance over which an exciton can diffuse between its generation and its recombination is rather short, so that only excitons produced close enough to the heterojunction are effective for electricity generation.[2,3] The high charge mobility is the key factor to increase the overall performance of OPV systems.[6-8] The carbon nanostructures such as fullerenes and carbon nanotubes (CNTs) have been emerged as promising materials to be incorporated in PV systems, due to their high electrical conductance, and thermal and chemical stability. For example, to enhance OPV's performances, conjugated polymer-fullerene thin films have been prepared because of their high charge mobility, crystallinity and thermal stability.[9-12] In line with this, we have developed two novel systems containing double walled carbon nanotubes (DWCNTs) and C_{60} motifs as electron acceptors and transporters, and porphyrin as electron donor units using

covalent approach. The morphological, chemical and photophysical properties of these hybrids are thoroughly characterized in this work.

5.1 Porphyrin-Double Walled Carbon Nanotube dyad systems

CNTs have emerged as active materials to be incorporated in organic photovoltaics[13-15] due to their high charge mobility as well as mechanical, thermal and chemical inertness. However, a few key-issues are still need to be addressed for the realization of multifunctional CNTs-based nanoconjugate and/or nanohybrid PV systems; particularly difficult is the reliable and reproducible control of the surface chemistry of CNTs and of their organization within the active layer owing to their particular intermolecular cohesive forces (0.5 eV nm^{-1}).[16] In fact, CNTs tend to strongly aggregate both in solution and in the solid state forming bundled structures that often cause a low reproducibility of the conducting properties and display a percolation threshold of a few percent.[16] The chemical derivatization, either through covalent[17-22] or non-covalent,[23-33] turned out to be an efficient strategy to create easy-to-process CNT-based materials.[34-37] In particular, the incorporation of photoactive antenna chromophores (displaying high extinction coefficient in the visible region of the solar spectrum) such as porphyrins[38] is one of the most popular routes to engineer charge-separation and photovoltaic conversion.[39-43] To get an intimate insight on the structural and electronic properties of CNT-porphyrin conjugates, in this work we report the preparation and physical characterization of some porphyrin-derived double-walled carbon nanotubes (DWCNTs) conjugates. With respect to single-wall counterparts, DWCNTs can be selectively functionalized at the external sidewall without disrupting the internal carbon layer thus keeping unaltered the conductive CNT properties. Therefore, oxidized DWCNTs (***ox*-DWCNTs**) have been covalently functionalized or physically absorbed to porphyrin molecules producing the three derivatives, **1-DWCNTs**, **1@(1-DWCNTs)** and **1@DWCNTs**. The schematic representation of all 3 Porphyrin-DWCNT hybrids, reference materials **1** and oxidized (ox) DWCNTs, and the corresponding synthetic strategy are depicted in **Scheme 5.1.1**.

5.1.1 Structural and morphological analyses

In order to investigate the degree of DWCNTs functionalization, XPS and TGA measurements were carried out on **1-DWCNTs**, **1@(1-DWCNTs)** and **1@DWCNTs**. The XPS data are presented in **Table 5.1.1**. As expected, all samples present the signature of C and O atoms, but only those bearing the fragments the presence of the N signature (N 1s at 400.0 eV). Notably, going from the non-covalent **1@DWCNTs** (0.4 at%) to the covalent 1-DWCNTs conjugate (1.1

at%), up to complex **1@(1-DWCNTs)** (1.8 at%) a net increase of the N atomic percentage has been observed. The maximum loading of N atoms occurs in the covalent samples as well as in the case of complex **1@(1-DWCNTs)** due to the additional layer of physisorbed porphyrin molecules. Similarly, the results obtained from TGA follow the same trend as that observed by the XPS analysis.

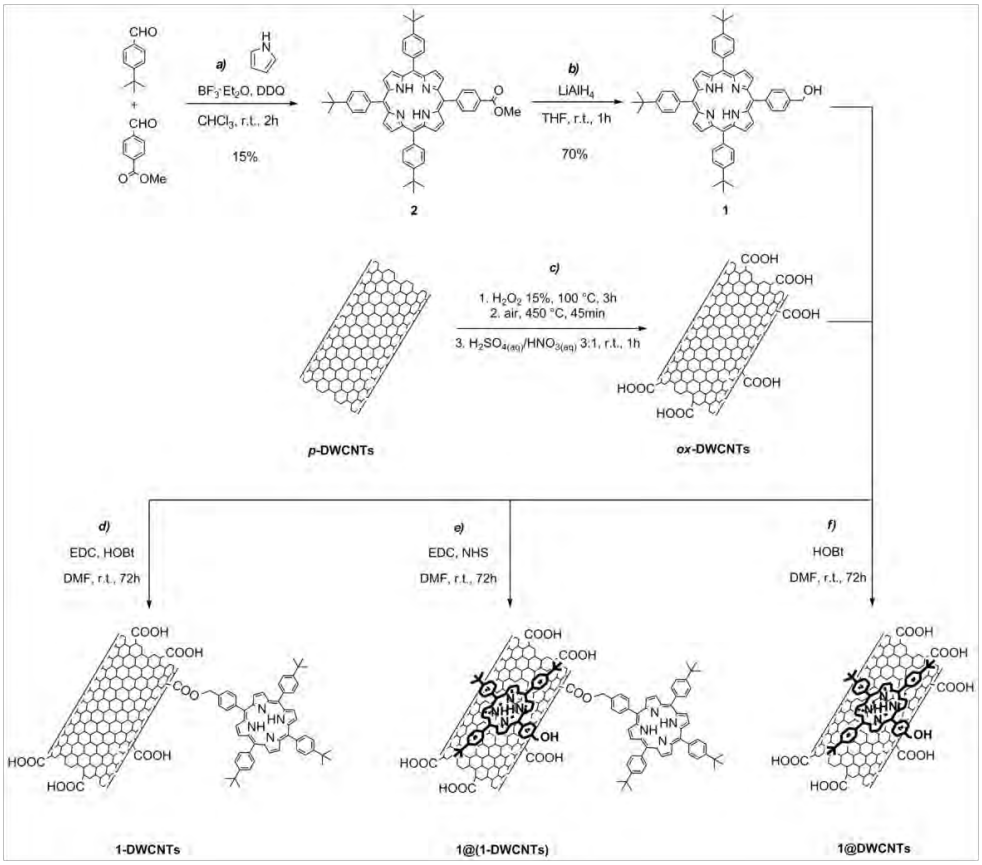

Scheme 5.1.1 *Synthetic pathways towards the preparation of* ***1-DWCNTs***, ***1@(1-DWCNTs)*** *and* ***1@DWCNTs and their*** *schematic representation. EDC: N-[3-(dimethylamino)propyl]-N'-ethylcarbodiimide; HOBt: N-hydroxybenzotriazole; NHS: N-hydroxysuccinimide.*

The pyrolysis of porphyrin **1** alone clearly appears with a prominent weight loss in the temperature range between 420 °C and 600 °C (**Figure 5.1.1b**). This weight loss step is also easily retrieved in the plot of **1@(1-DWCNTs)** complex proving the presence of porphyrin molecules (**Figure 5.1.1c**, arrow c). The differential plot of **1@(1-DWCNTs)** reports two other pyrolytic events between 100 °C and 400 °C (**Figure 5.1.1c** arrows a-b). These peaks can be interpreted as the signature of the pyrolysis of both EDC-functionalities and unreacted carboxylic groups attached on the CNTs frameworks. Once the pyrolysis of **1** has occurred, after 600 °C, **1@(1-DWCNTs)** was subjected to a 25.6% w/w loss, while **1-DWCNTs** and **1@DWCNTs** (**Figure 5.1.1c**) presented weight losses of 9.7% w/w and 8.5% w/w, respectively. Hence, TGA observations corroborate the XPS measurements attesting the higher loading of molecule **1** on the hybrid

complex **1@(1-DWCNTs)**, also highlighting the efficiency of the purification steps carried out on the covalent derivative to remove the exceeding porphyrin quantities.

Table 5.1.1 *Compositional data obtained from XPS analysis of the investigated CNTs derivatives.*

Sample	C (%)	N (%)	O (%)
***p*-DWCNTs**	97.1	-	2.9
***ox*-DWCNTs**	94.0	-	6.0
1-DWCNTs	92.5	1.1	6.4
1@(1-DWCNTs)	89.4	1.8	8.8
1@DWCNTs	92.3	0.4	7.3

As a consequence of the presence of the covalently and non-covalently appended porphyrin units, the porphyrin-bearing DWCNTs show better dispersability than ***ox*-DWCNTs** in organic solvents such as DMF and $CHCl_3$. Interestingly, whereas conjugates **1-DWCNTs** and **1@DWCNTs** form stable dispersions, ***ox*-DWCNTs** show extensive precipitation after an initial apparent dissolution. This indirectly indicates that the amount of CNTs dispersed in solution is expected to be substantially larger for **1-DWCNTs** and **1@DWCNTs** samples, thus enabling a more thorough characterization of the DWCNTs derivatives using optical spectroscopy.

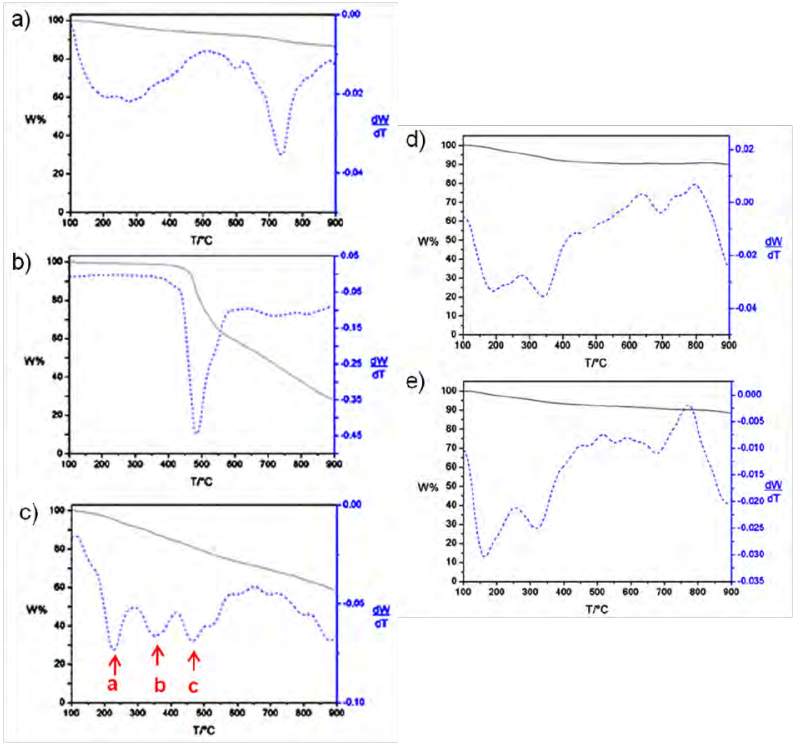

Figure 5.1.1 *Temperature-modulated (solid lines) and differential (dashed lines) gravimetric plots of (a)* ***ox*-DWCNTs***, (b)* ***1*** *(c)* ***1@(1-DWCNTs)***, *(d)* ***1-DWCNTs*** *and (e)* ***1@DWCNTs***, *recorded under N_2 atmosphere with a thermal increase of 10 °C min^{-1}.*

Although solutions of DWCNTs derivatives are transparent in DMF and $CHCl_3$ and do not exhibit any floating matter by visual inspection, the DWCNTs derivatives are, in fact, dispersed in a stable colloidal-like state. This has been confirmed by dynamic light scattering (DLS) measurements which displayed the presence of two groups of objects with different mean size (**Table 5.1.2**). In particular, the size distributions of the suspended carbon nanotube derivatives in clear, eyes-transparent DMF and $CHCl_3$ dispersions of **1-DWCNTs**, and **1@DWCNTs** are shown in **Figures 5.1.2 and 5.1.3**, respectively; the particles sizes are listed in **Table 5.1.2**.

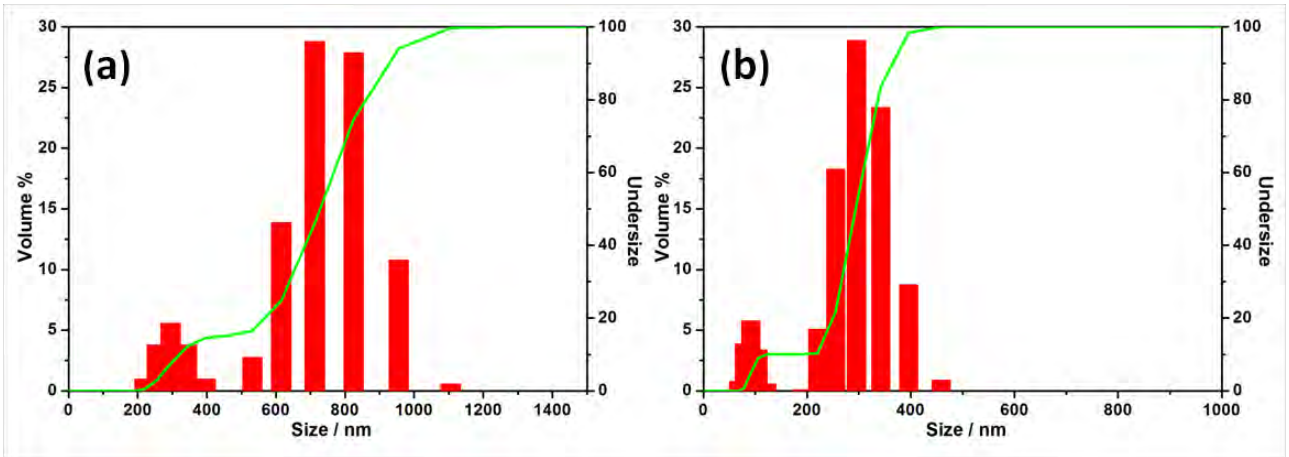

Figure 5.1.2 *Size distribution of DWCNTs bundles in (a) DMF and (b) $CHCl_3$ dispersion of* ***1-DWCNTs****.*

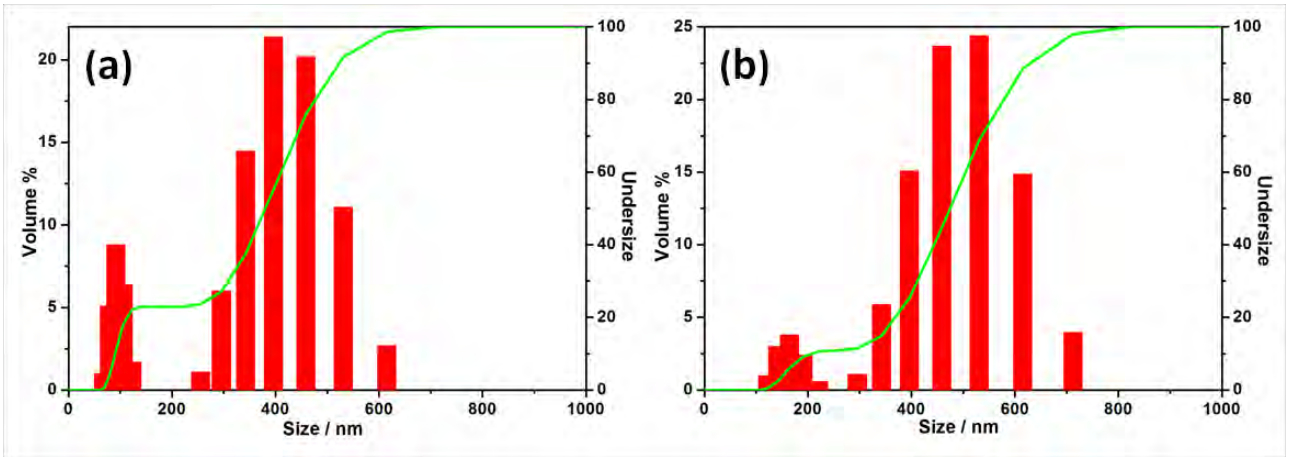

Figure 5.1.3 *Size distribution of DWCNTs bundles in (a) DMF and (b) $CHCl_3$ dispersion of* ***1@DWCNTs****.*

From **Table 5.1.2**, it is clear that the particle sizes of the porphyrin-bearing DWCNTs hybrids in the dispersion are larger than that of the oxidized precursor, ***ox*-DWCNTs**. This is a consequence of the reduced bundling behavior of the functionalized DWCNTs caused by the presence of the porphyrin moieties, which imparts better solubility to the hybrid material (*i.e.* increasing the number of large particles stable in solution). In the case of ***ox*-DWCNTs**, the larger nanotubes easily entangle and form large bundles that are more insoluble and quickly collected in

the precipitate; accordingly, only very small and short CNTs remain in solution. However, all dispersions are not optimal for photophysical investigations because they undergo light scattering and prevent quantitative optical measurements (*vide infra*), particularly by means of transient spectroscopy upon intense laser excitation.

Table 5.1.2 *Particle sizes distribution of the DWCNTs conjugates in DMF and $CHCl_3$ dispersions as evaluated from DLS measurements.*

Sample	Particle Size (nm)	
	DMF dispersion	$CHCl_3$ dispersion
***ox*-DWCNTs**	290[a], 60	[b]
1-DWCNTs	300, 90	730, 300
1@DWCNTs	400, 100	470[a], 160

[a] Due to very limited dispersibility of ***ox-DWCNTs****, the measurements for such materials have been carried out after removing all the floating DWCNTs, so the concentration of dispersed tubes is lower compared to the other samples. [b] Impossible to be measured due to the large size of agglomerates.*

5.1.2 Modeling of the conformational properties of Porphyrin-DWCNTs derivatives

Force field-based simulations using a combined molecular mechanics and molecular dynamics approach have been carried out in order to gain insight on the interactions between the porphyrin molecule and the nanotube framework. For simplicity, Single Walled CNTs (SWCNTs) were considered, mimicking the outer shell of the DWCNTs.

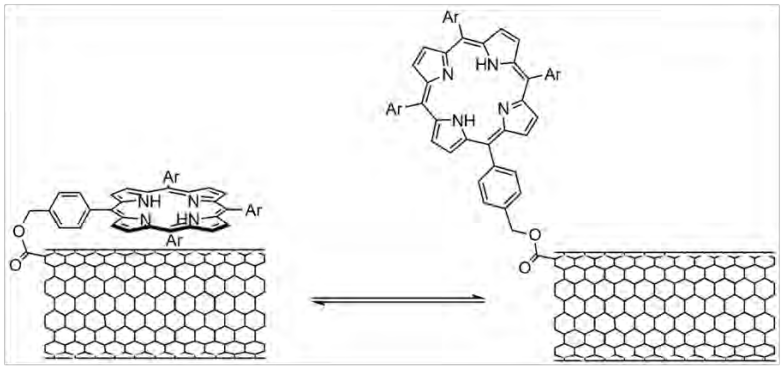

Figure 5.1.4 *Schematic representations of the dynamic equilibrium existing between the "tight" and "loose" conformations of* ***1-DWCNTs****, when* ***1*** *is linked to the tips. The same equilibrium may exist also when the porphyrin fragment is linked to the edge of the tube. Ar stands for 4-(tert-butyl)phenyl.*

As reported earlier for covalently-linked fullerene-porphyrin conjugates,[44-46] several conformational equilibria can occur in solution.[47,48] Likewise, a dynamic equilibrium between "loose" and "tight" porphyrin-CNTs pairs, in which the carbon nanotube and the porphyrin are in

the "face-to-face" conformation in the ground state, can be considered (**Figure 5.1.4**). The "tight" and the "loose" conformation differ in the distance between the porphyrin and the CNTs and in their solvation.[49] The aim of the modeling here presented is thus to determine the most probable conformation of the porphyrin unit on the CNT wall and to quantify the strength of the interactions between the two species.

Two situations were modeled with the porphyrin molecule either simply physisorbed on the CNT surface (*i.e.*, **1@DWCNTs**) or chemically grafted on the CNTs framework *via* a $COOCH_2$ linker (*i.e.*, **1-DWCNTs**). For the covalent conjugate, two different grafting sites were considered: along the wall or at the edge of the open tips. **Figure 5.1.5** shows the top, front and side views for the three structural situations: in (a) the porphyrin is physisorbed, while in (b) and (c) the porphyrin fragment is covalently bound to the wall and at tips, respectively. In structures (a) and (b), the tetrapyrrolic ring is roughly parallel to the nanotube surface: its core is slightly bent, with a mean distance of 0.35 nm from the nanotube. This value is typical of π-stacking and the slight bending of the core allows for optimal π-π interactions. In (c), the porphyrin core is not directly interacting with the nanotube and the molecule remains flat. Note that in all three cases, CH-π interactions are present between the side groups and the nanotube surface.

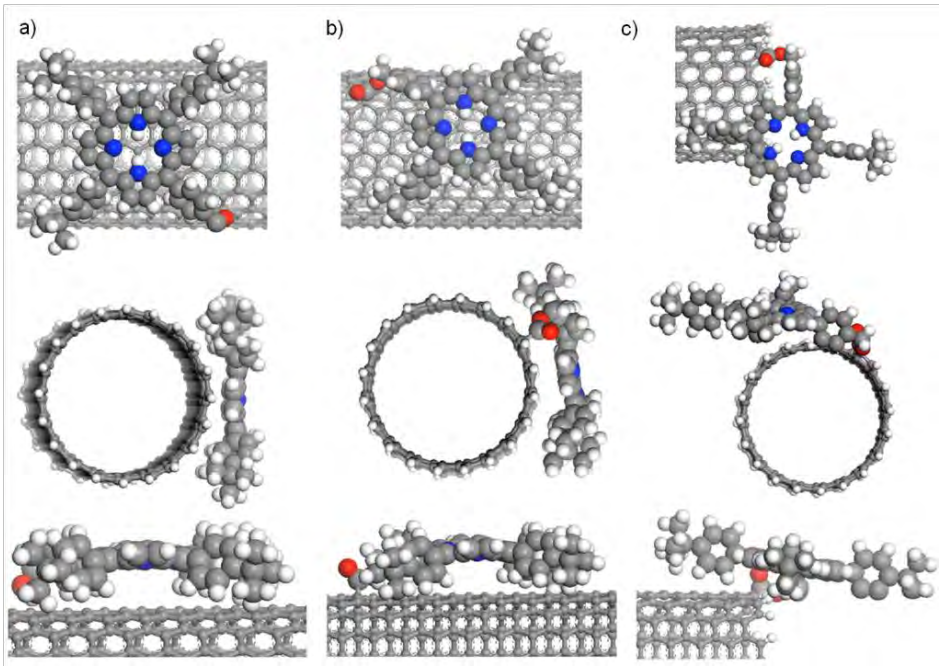

Figure 5.1.5 *Top, front and side views for (a) a porphyrin molecule physisorbed and covalently-bound to the nanotube (b) wall or (c) tips in a "tight" conformation.*

The potential energy for the physisorbed system cannot be strictly compared with the covalent systems, because of the different atomic compositions. Nevertheless some useful information can be obtained. The adsorption energy for a single physisorbed porphyrin molecule

interacting with the CNT wall is about -60 kcal/mol. Consistently, the comparison for the two grafted arrangements shows that system (b) is about 60 kcal/mol more stable than system (c), reflecting larger van der Waals interactions between the porphyrin and the nanotube external wall when the molecule is grafted along the side. Notably, the flexibility of the linker can allow for conformations in which the end-grafted porphyrin is partly adsorbed on the CNT wall (*vide supra*). Since the formation of carboxylic acids is expected to prominently take place at the tube ends, it is also relevant to model the presence of more than one porphyrin molecule covalently attached at the CNT edge. We have thus investigated systems having two porphyrin fragments covalently bound at the nanotube tip: the first porphyrin is attached to a fixed position and the second one is attached at an increasing distance from the first one. The various possibilities are denoted as 1-2, *i.e.*, the two molecules are attached on neighboring carbon atoms, up to 1-9, *i.e.*, where the porphyrins are on opposite sides of the nanotube edge (**Figure 5.1.6**). The two most stable structures have been obtained for positions 1-4 and 1-6. In the 1-4 case, one porphyrin (in red) is adsorbed on the nanotube wall, thanks to the flexibility of the $COOCH_2$-Ph linker. The second porphyrin (in blue) is partially inside the nanotube and the two molecules only weakly interact. In contrast, the porphyrins in the 1-6 system are oriented in such a way that they can directly interact, even though the distance and orientation of the cores are such that π-π interactions cannot take place (only CH-π interactions are present). Nevertheless, the 1-4 system is almost 20 kcal/mol more stable than its 1-6 counterpart; this is likely due to the strong favorable interaction between the 'red' porphyrin molecule and the nanotube in the 1-4 models (**Figure 5.1.6**).

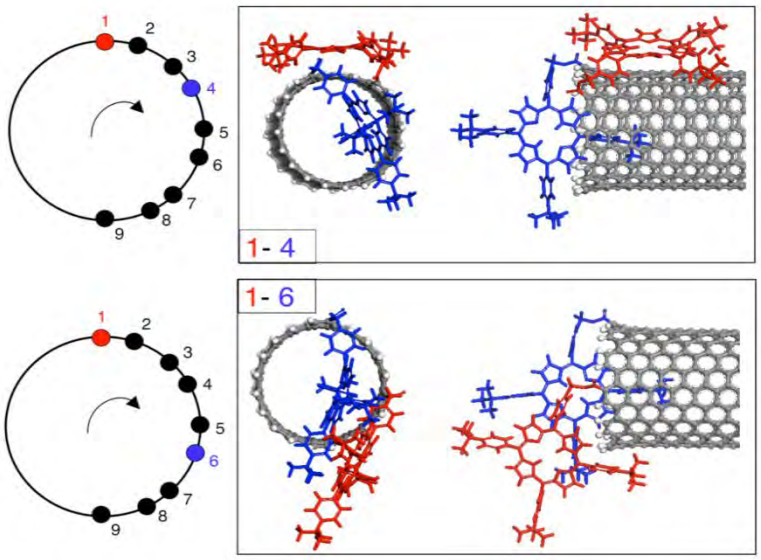

Figure 5.1.6 *Front and side views for the 1-4 and 1-6 systems, in which two porphyrin molecules are attached at the nanotube tips.*

5.1.3 Photophysical properties of porphyrin-DWCNTs derivatives

The photophysical studies of hybrid materials **1-DWCNTs** and **1@DWCNTs**, and reference samples **1** and ***ox*-DWCNTs** were carried out in DMF and $CHCl_3$, due to their proved efficacy in dispersing the carbon nanomaterials. The electronic absorption spectra of all the materials in DMF are shown in **Figure 5.1.7**. Both hybrid materials **1-DWCNTs** and **1@DWCNTs** show porphyrin-centered Soret bands at 419 nm, similar to free molecules **1**, whilst the weaker Q-bands are not discernible due to the overwhelming absorption of ***ox*-DWCNTs** counterpart. Similarly, Q-bands are barely observable in $CHCl_3$ dispersions along with the prominent Soret feature at 421 nm (**Figure 5.1.7**). The different absorption intensities of the Soret band between the two hybrid materials reflect the higher porphyrin loading provided by covalent functionalization compared to the physisorbed **1@DWCNTs** sample. The broadening of the Soret band and a small shoulder around 450 nm suggests weak interporphyrin interactions, probably between those located on the same DWCNT unit (*vide supra*).[49] In addition, as suggested by molecular modeling, several conformations between the carbon nanotube surface and the porphyrin unit in solution, may also result in broadening of the **1**-centered Soret band. Apart from the above changes, no other significant differences have been observed for the hybrid materials.[20,32,50]

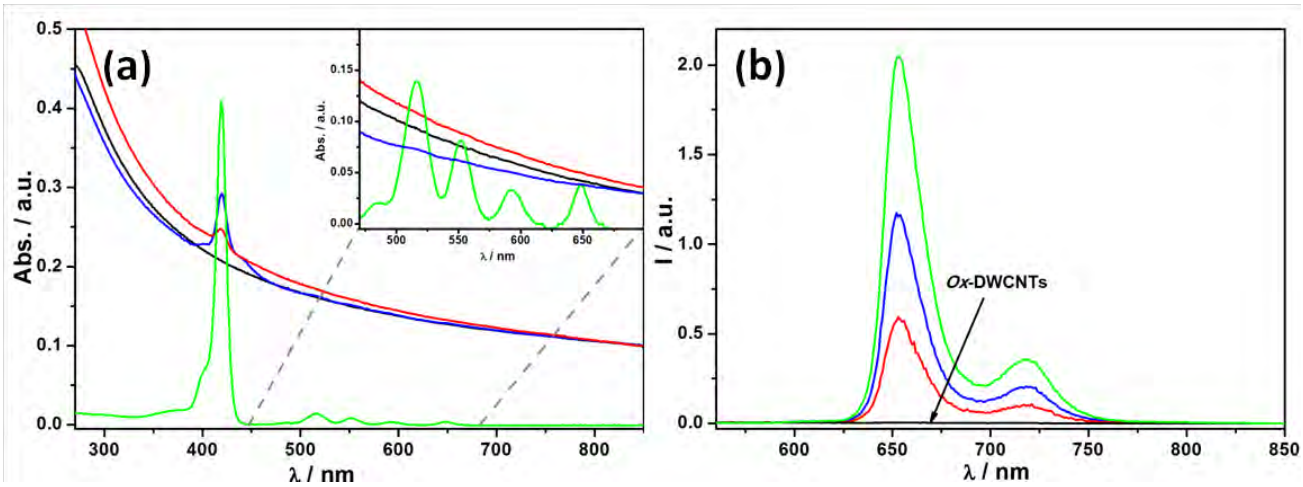

Figure 5.1.7 *(a) Electronic absorption (b) emission spectra of **1** (green), **ox-DWCNTs** (black), **1-DWCNTs** (blue) and **1@DWCNTs** (red) in DMF. Inset: expanded Q-band region of all the materials. Spectra of DWCNTs materials are normalized at 850 nm. Emission spectra are collected upon excitation at 420 nm. Note: the qualitative trend of emission intensities is that observed experimentally (1 > 1-DWCNTs > 1@DWCNTs) but the intensity ratios must not be taken for quantitative comparisons (see text).*

The luminescence spectra of **1**, ***ox*-DWCNTs**, **1-DWCNTs** and **1@DWCNTs** were recorded using solutions with matching absorption at the Soret band maximum (420 nm). Upon excitation, the hybrid materials show a fluorescence profile that is perfectly superimposable to that of free porphyrin **1** in DMF (**Figure 5.1.7**) and $CHCl_3$. The emission intensities of **1-**

DWCNTs and **1@DWCNTs** are found to be lower than that of porphyrin **1** alone, but a quantitative determination cannot be made due to at least four interfering factors (*vide infra*).[17,32,50] Therefore, this observation alone cannot be ultimately indicative of photoinduced energy or electron transfer processes causing quenching of the porphyrin singlet level.[17]

The observed reduction of the porphyrin fluorescence intensity of **1-DWCNTs** and **1@DWCNTs** may be due to factors such as *(i)* light partitioning between **1** and DWCNTs, so that a considerable portion of the incoming photons causes excitation of the carbon nanotube scaffold; *(ii)* excitation and emission light scattering due to the presence of particles in the hybrid dispersions, (*vide supra*); *(iii)* different porphyrin concentration in the hybrid dispersions due to different functionalization methodology; *(iv)* significant presence of quenched "tight"-type conformers in which the porphyrins-centered singlet excited state is deactivated by the DWCNTs. Notably, the singlet excited state lifetime of the porphyrin is not reduced for all samples in both solvents (**Table 5.1.3**). This corroborates *(i)-(iv)* as reasonable explanations for the observed trends in luminescence intensities of **Figure 5.1.7** and underpins the lack of evidence of photoinduced phenomena between porphyrins and DWCNTs. The porphyrin fluorescence decays of **1-DWCNTs** and **1@DWCNTs** are monoexponential, suggesting a uniform physical environment for the emissive centers in the dispersions. The slightly longer porphyrin lifetime value of the hybrid materials compared to free porphyrin can be caused by the reduced vibrational relaxation of the excited states of the porphyrin moieties when anchored on the rigid CNT walls.

To probe the triplet states of the appended porphyrins, experiments on sensitized singlet oxygen luminescence were carried out with **1**, **1-DWCNTs** and **1@DWCNTs** in $CHCl_3$.[51] Upon excitation of the porphyrin singlet bands, the lowest energy singlet state S_1 populates the lowest triplet state (T_1) through intersystem crossing. Owing to the long lifetime of porphyrin T_1, the molecular oxygen present in the solvent deactivates it through energy transfer and forms excited singlet oxygen ($^1O_2$), which emits at 1270 nm.[49] By monitoring the $^1O_2$ near infrared emission intensity, an indirect estimation of the triplet state generated by the porphyrins anchored on DWCNTs is obtained.[48] The $^1O_2$ emission bands from free porphyrin **1** and hybrid materials are shown in **Figure 5.1.8a**. Due to the same reasons indicated for fluorescence spectra, singlet oxygen emission intensities of the hybrid materials are not directly comparable with that of porphyrin **1**.

In addition, porphyrin centered triplet state lifetimes of reference compound and hybrid materials were probed at 470 nm, using nanosecond transient absorption spectroscopy. The resulting decay curves are mono-exponentially fitted and the values are 189 μs and 181 μs for **1**

and **1-DWCNTs**, respectively (**Figure 5.1.8b**).[52] Identical triplet lifetimes confirm the presence of unquenched porphyrin units in the hybrid material.

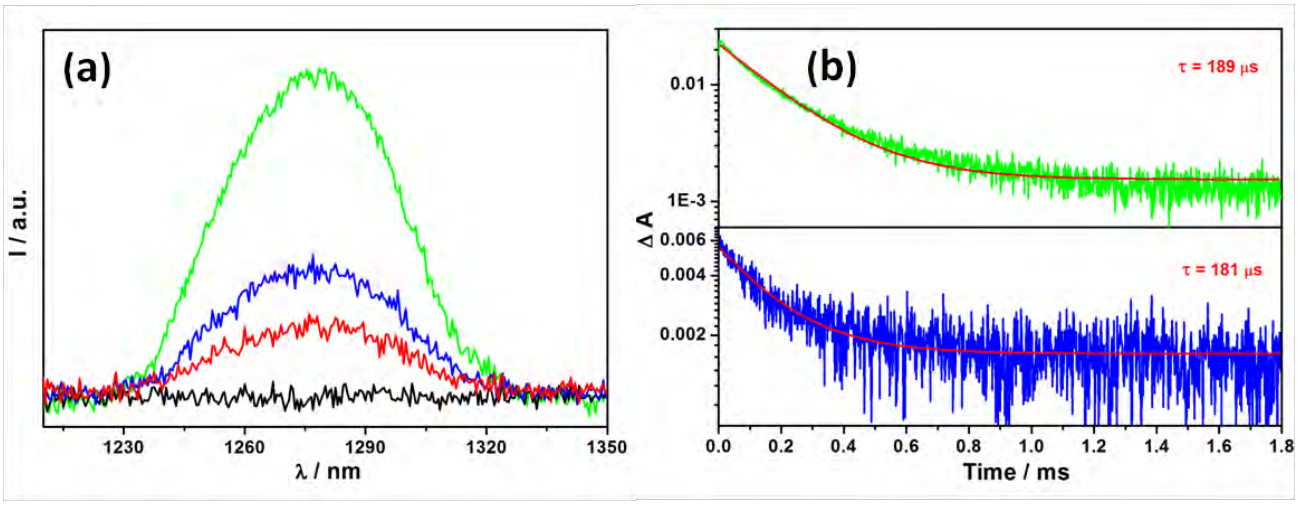

Figure 5.1.8 *(a) Sensitized singlet oxygen emission spectra of 1 (green), ox-DWCNTs (black), 1-DWCNTs (blue) and 1@DWCNTs (red) by exciting at 420 nm in $CHCl_3$; (b) transient absorption decay curves of 1 (green, O. D = 0.3, laser energy = 0.7 mJ/pulse) and 1-DWCNTs (blue, O. D = 0.5, laser energy = 1.5 mJ/pulse), excited at 550 nm and collected at 470 nm.*

As discussed above in the modeling section, molecular modeling suggests the existence of "loose" and "tight" pairs between porphyrin and DWCNTs. Unlike the case of the fullerene systems,[45,48] the photophysical analysis cannot provide direct evidence for such interchromophoric interactions, but anyway do not contradict such model. In fact, if the fluorophore and the quencher are approaching each other up to the shortest distance ("tight" conformation), photo-induced energy/electron transfer rates may become so fast to successfully compete with the intrinsic deactivation of the porphyrin and yield complete quenching of luminescence. In other words, this "tight" situation must lead to a virtually complete reduction of the emission intensity and a vanishingly short lifetime. On the other hand, in the case of "loose" pairs, the attached chromophores should behave as in the absence of quenching interactions and must show the characteristic luminescence properties of **1**. Hence, luminescence data are compatible with the presence of "tight" and "loose" pairs, with the latter being responsible for the residual and kinetically unquenched luminescence signals. This picture of non-interacting porphyrin/DWCNTs arrangements is supported by the observation of singlet oxygen luminescence that further signals the presence of completely unquenched porphyrin moieties in their triplet states. These findings are somewhat surprising since those indicate the absence of intermediate situations, in between "tight" and "loose", where the porphyrin-DWCNTs distance causes dynamic quenching of the porphyrin moieties with reduced singlet lifetimes.

Table 5.1.3 *Singlet lifetime values of porphyrin 1 and hybrid materials in solutions and PMMA matrix.*

Sample	Lifetime (ns)		
	DMF	$CHCl_3$	PMMA[a]
1	10.2	7.8	4.2
1-DWCNTs	10.6	8.9	4.4 (53%) 6.5 (47%)
1@DWCNTs	11.1	9.3	1.4 (50%) 8.1 (50%)
1@(1-DWCNTs)	9.9	-	-

a-the value inside the bracket denotes the relative contribution of the corresponding decay in the overall decay

Finally, DMF dispersions of **1@(1-DWCNTs)** were also investigated. The absorption and emission features of **1@(1-DWCNTs)** exhibit an intensity quite similar to **1**, showing the high loading of porphyrins on DWCNTs (**Figure 5.1.9**). Similarly to **1-DWCNTs** and **1@DWCNTs**, no shift or broadening is observed either in absorption or in emission bands (**Figure 5.1.9)**. Also the lifetime value (τ = 9.9 ns) exactly matches with that of porphyrin **1** alone, suggesting the same situation as observed in $CHCl_3$.

To shed further light on the electronic properties of **1-DWCNT** and **1@DWCNTs** incorporated in polymeric active layers, thin films have been prepared by dispersing the hybrid materials in the pyrene-terminated poly(3-hexylthiophene) polymer, P3HT-Py. The dispersions were spin coated on an indium tin oxide (ITO) glass surface but the overwhelming spectral features of the P3HT-Py matrix hid all the absorption and emission bands of the porphyrin, thus hampering the photophysical characterization of the hybrid materials in this medium. Therefore, in order to investigate the optical properties of the DWCNTs hybrids in a polymer matrix, the transparent and photo-inactive poly(methylmethacrylate) (PMMA) polymer was chosen as the solid-state medium and related thin films were made by drop-casting $CHCl_3$ dispersions containing all the conjugates. In contrast to solution experiments, the spectral features of **1**, **1-DWCNTs** and **1@DWCNTs** recorded in PMMA thin films show the presence of aggregates (**Figure 5.1.10**).

For molecule **1**, the split Soret band and the red-shifted Q-band maximum are indicative of *J*-type "head-to-tail" porphyrin aggregation.[20,53-60] The formation of *J*-aggregates is promoted by the poor porphyrin dispersibility in aliphatic PMMA polymer and by the presence of dipoles induced by polar -OH functionality on the macrocyclic rings. According to Kasha's theory,[61] these large structures substantially modify the pattern of the Soret (splitting) and Q-bands (red-shifted maximum), as indeed observed here.

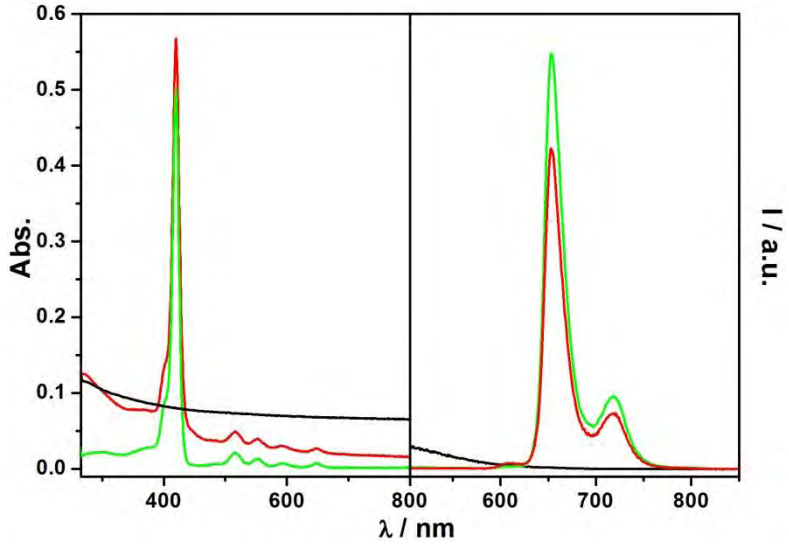

Figure 5.1.9 *Absorption (left) and emission (right, λ_{ex} = 420 nm) spectra of* ***1*** *(green),* ***ox-DWCNTs*** *(black),* ***1@(1-DWCNTs)*** *(red) in DMF.*

Interestingly, the same spectral features of **1** alone are observed in the PMMA dispersion of **1-DWCNTs**, suggesting a similar ordered arrangement of the porphyrin chromophores in the rigid medium. Such *J*-type interactions are perhaps favored by steric effects induced by the presence of the highly-hindered DWCNTs framework, whereas face-to-face intramolecular interactions seem to be prevented, as also confirmed by the absorption spectra obtained from solution (*vide supra*).[62] For samples containing **1@DWCNTs**, owing to the low concentration of porphyrins, the related electronic absorption bands are masked by the strong absorption of DWCNTs. However, luminescence measurements (λ_{exc} = 420 nm) show a weak band clearly attributable to porphyrin fluorescence, thus confirming the presence of the chromophore in the sample (**Figure 5.1.11b**). Upon excitation of **1@DWCNTs** at 445 nm, a broader fluorescence band is detected (**Figure 5.1.11a**), and the related excitation spectrum collected at the emission maximum, showing a split Soret band, where the new feature is higher in energy (395 nm) than the characteristic band at 419 nm.

Compared to **1** and **1-DWCNTs**, these findings suggest a different arrangement of the porphyrin units in **1@DWCNTs**, *i.e.* face-to-face *H*-aggregates, which are not generated in **1-DWCNTs** as discussed above.[60] The allowed in-phase arrangement of transition dipoles in *H*-aggregates results in a higher energy electronic transition which is responsible for the Soret band peak at shorter wavelength. On the other hand, the out-of-phase arrangement of transition dipoles generates a forbidden, low energy, transition to the S_1 state. Upon excitation of **1@DWCNTs**, the high energy S_2 level is populated, which then decays to a weakly emitting S_1 state.[60]

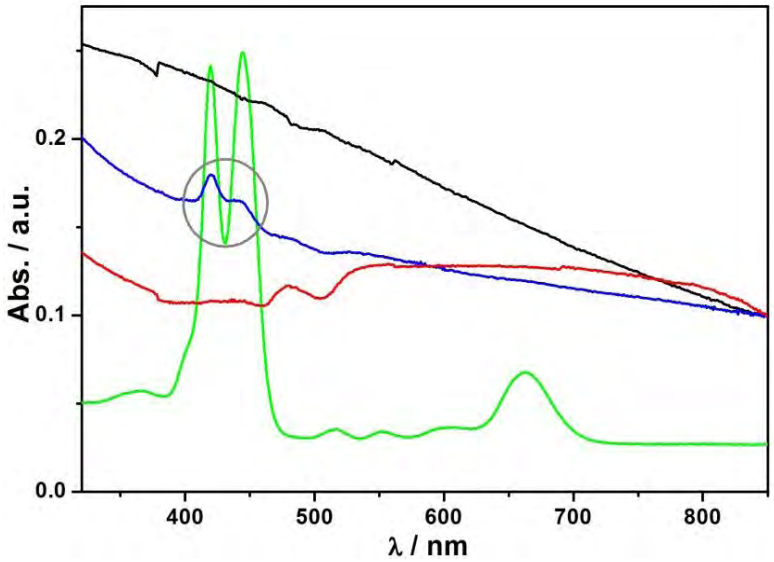

Figure 5.1.10 *Electronic absorption spectra of* ***1*** *(green),* ***ox-DWCNTs*** *(black),* ***1-DWCNTs*** *(blue) and* ***1@DWCNTs*** *(red) in PMMA polymer matrix.*

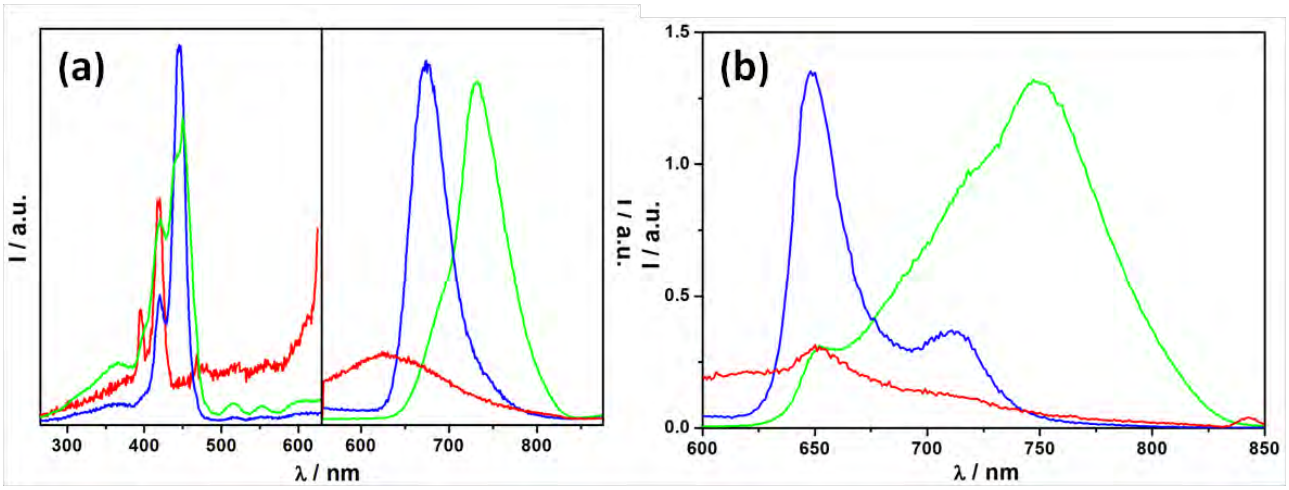

Figure 5.1.11 *(a) Excitation (left) and emission (right,* λ_{em} *= 445 nm) spectra of* ***1*** *(green),* ***1-DWCNTs*** *(blue) and* ***1@DWCNTs*** *(red) in PMMA polymer matrix. The excitation spectrum of each material is collected at its respective emission maximum. (b) Emission spectra of* ***1*** *(green),* ***1-DWCNTs*** *(blue) and* ***1@DWCNTs*** *(red) upon excitation at 420 nm in PMMA matrix.*

In J-aggregates, depending on the strength of interchromophoric interaction, the low energy exciton states shift the emission maxima accordingly, i.e. the stronger the interaction the more red-shifted the band is.The emission spectra of **1** and **1-DWCNTs** exhibit maxima at 732 and 675 nm respectively, indicating stronger interactions in the aggregates of **1** alone than in those of the more sterically congested **1-DWCNTs** (λ_{exc} = 445 nm, **Figure 5.1.11**).[60] Apart from the presence of J and H aggregates, characteristic porphyrin-centered emission bands are still observed in all three materials when exciting the Soret (420 nm) and Q band (515 nm) features (**Figure 5.1.11b**). This shows the presence of free porphyrin units, especially in the case of hybrid

materials, where the porphyrin emission intensity is significantly high. The fluorescence decay profiles of **1-DWCNTs** and **1@DWCNTs**, which are fitted as biexponential, support the above rationale. Both hybrid materials possess a long and a short lifetime with a similar proportion (**Table 5.1.3**). Notably, the short lifetime of **1-DWCNTs** is the same as that of **1**, confirming similar aggregation processes in both materials. The long lifetime stems from non-aggregated porphyrin units as evidenced by the emission spectrum. In **1@DWCNTs**, as mentioned above, the excited S_1 state rapidly decays to the ground state (= 1.4 ns). Similar to the solution phase, the physisorbed porphyrins show a longer lifetime value than that of the free porphryrins. This is attributed to the reduced vibrational relaxation from the lower-lying excited state (**Table 5.1.3**), ultimately confirming their interaction with the DWCNTs framework.

5.1.4 Optoelectronic characterization of Porphyrin-DWCNTs blended polythiophenes-based polymers

The role of the functionalized CNTs frameworks in the polymer blends for photovoltaic applications is subtle as they could behave like versatile, interpenetrating unidimensional hole-extracting materials as well as electron accepting units and conductive networks.[28,63-69] Therefore, in order to evaluate the potential properties of the porphyrin-DWCNTs derivatives as in the active layers for photovoltaic devices, we fabricated several **glass/ITO/PEDOT:PSS/Active Layer/Al** devices with the aim of investigating the interaction of the chemically-modified DWCNTs and of **1@(1-DWCNTs)** with the P3HT-Py polymer matrices by addressing the reproducibility of both morphological and conducting properties of the active layers. Besides small concentrations of the DWCNTs derivative (*ca.* 1%), we also added small amounts of [60]PCBM (< 5%) in order to balance the charge carrier transport to the electrodes. Specifically, 100-nm thin films were prepared by spin-coating a solution (c = 15 mg/ml) of *p*-xylene containing the appropriate amounts of derivatized DWCNTs, [60]PCBM and P3HT-Py. Samples containing **1@DWCNTs** and **1-DWCNTs** led to similar results.

Scanning Near-field Optical Microscopy AFM (AFM-SNOM) studies have been carried out to study the morphology of the thin films containing the active layers from composite dispersions of the porphyrin-based DWCNTs investigated in this work.[70] The results are shown in **Figure 5.1.12b**. The typical topography of the thin films containing **1@(1-DWCNTs**) is presented at micro-scale in the left panel and the SNOM signal (accumulated in the transmission mode) is displayed in the right panel. Both images clearly show a region where the functionalized DWCNTs are debundled and in intimate contact with the P3HT-Py polymer, as also highlighted by the uniform distribution of the tubes within the polymeric layer. At these low-doping levels,

the porphyrin-DWCNTs hybrids do not protrude from the film and their UV-Vis absorption is much smaller than that of the surrounding polymer matrix. In addition, the intrinsic UV-Vis absorption properties of the porphyrin fragments at the working wavelength (*i.e.*, 532 nm) do not seem to noticeably influence the optical contrast imaging of the functionalized DWCNTs and PCBM. On the other hand, the presence of dark spots in the SNOM image is attributed to zones of the layer in which [60]PCBM molecules are aggregated.[73]

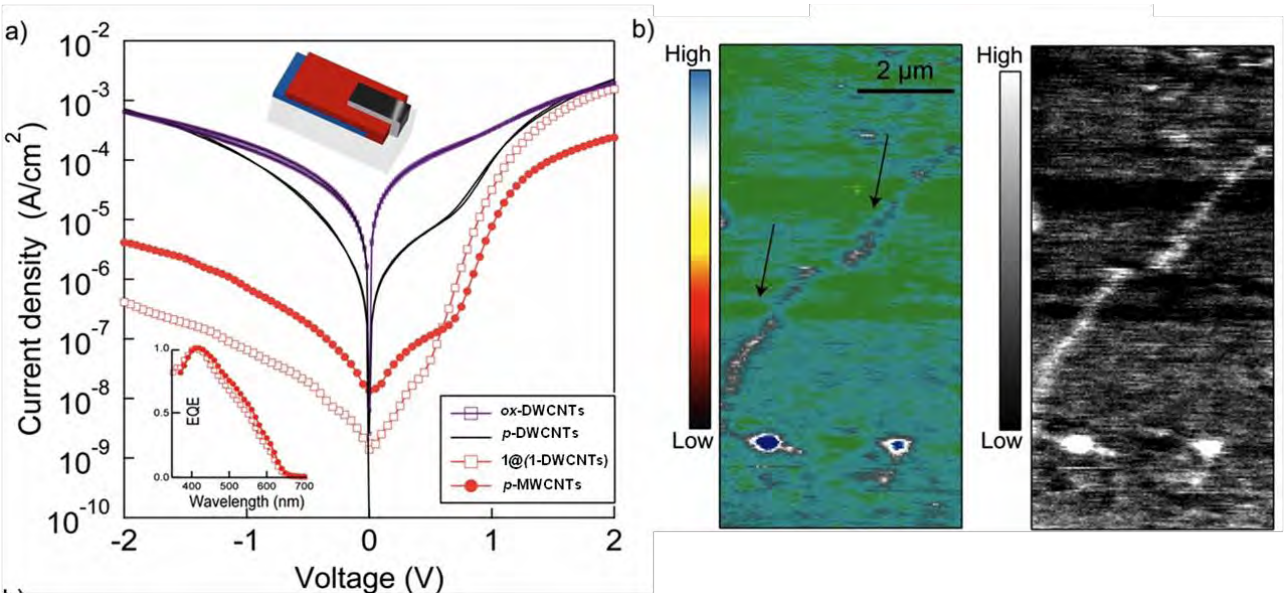

Figure 5.1.12 *a) J-V curves measured in dark, at room temperature, for thin films of P3HT-Py loaded with reference* ***p-MWCNTs*** *and PCBM (filled circles), with* ***p-DWCNTs*** *and PCPM (black curve), with* ***ox-DWCNTs*** *and PCBM (blue curve) and doped with* ***1@(1-DWCNTs)*** *and PCBM (empty squares). The device structure (glass/ITO/PEDOT:PSS/ActiveLayer/Al) is schematically shown. Inset: Normalized EQE wavelength dependencies for fabricated thin films with* ***p-MWCNTs*** *and porphyrin-functionalized DWCNTs; b) coupled AFM topography (left) and SNOM optical contrast (right) micrographs obtained under monochromatic laser radiation (532 nm) for the as-deposited active layers including* ***1@(1-DWCNTs)****. At the bottom of the images, protrusions in the film are observed (several tenths of nanometers above the surface in the AFM panel), which can be associated to* ***1@(1-DWCNTs)*** *surrounded by PCBM and/or porphyrin aggregates in the SNOM transmission image.*

Figure 5.1.12a presents the room-temperature dark current density-voltage (*J-V*) characteristics of typical P3HT-Py films containing the carbon nanohybrid structures**.** The forward bias conditions correspond to positive voltage on the ITO electrode with respect to the Al cathode. The *J-V* dependence is asymmetric, suggesting the presence of a blocking contact (Schottky barrier) at the bottom of the poly(3,4-ethylenedioxythiophene):poly(styrenesulfonate) PEDOT:PSS/active layer thin-film interface. This is responsible for the observed rectification effect as the other upper interface is supposed to behave like an Ohmic contact. At high voltages, the series resistance or the space charge build up deviates the injected current from the exponential behavior limit. Thus, the observed intensification of the forward current in the **1@(1-**

DWCNTs)-based devices suggests a smaller hole-injection barrier compared to those reference devices containing only CNTs materials, such as ***p*-DWCNTs**, ***ox*-DWCNTs** or reference ***p*-MWCNTs**. Our results corroborate state-of-the-art works[65,67,68] and the standard metal-insulator-metal model, where the built-in potential across the organic thin film equals the work function difference between the Al cathode (4.3 eV) and the PEDOT:PSS anode (5.1 eV), providing a distinctive kink structure in the forward bias of the *J-V* plots. The increase in the forward current observed for films containing hybrids **1@(1-DWCNTs)** is accompanied by a better rectification ratio compared to the responses observed by those devices containing ***p*-DWCNTs** and ***ox*-DWCNTs** where a very similar behavior, with minor differences in the low bias regime, has been observed. In order to evaluate the photoactive role of the porphyrin moieties within the active layer, quantum efficiency measurements (defined as the percentage of photons hitting the photoreactive surface that will produce an electron hole pair) have been performed. In particular, an experimentally accessible value is the external quantum efficiency or incident photon to current efficiency (EQE), which is defined as the number of photogenerated charge carriers over the number of incident monochromatic photons. In this respect, the line shape of the EQE profile (in arb. units), normalized at 420 nm, is displayed in the inset of **Figure 5.1.12** and closely follows the absorption band of the polymer blend. No differences have been detected between active layers containing the porphyrin-functionalized hybrid or reference CNTs, thus indicating a negligible effect of the porphyrin moieties.

5.1.5 Summary

This work focused on the preparation and physical characterization of diverse porphyrin-derived DWCNTs conjugates. In particular, COOH-derived DWCNTs, produced by means of a three-step oxidative protocol, were covalently linked and physically adsorbed to a porphyrin molecule producing three derivatives, **1-DWCNTs**, **1@(1-DWCNTs)** and **1@DWCNTs**. The structural properties of all porphyrin-DWCNTs conjugates were fully investigated *via* Thermogravimetric Analysis (TGA), Energy Dispersive X-ray Spectroscopy (EDX), X-Ray Photoelectron Spectroscopy (XPS), Transmission Electron Microscopy (TEM), Atomic Force Microscopy (AFM) and Dynamic Light Scattering (DLS) experiments. The photophysical characterization of porphyrin-CNTs derivatives were investigated through steady state and time resolved absorption and emission measurements, both in solution and in the solid state. Eventually, no convincing proofs were observed for electron transfer interactions between porphyrin donor and DWCNT acceptor moieties. The UV-Vis absorption profiles taken in PMMA matrix unambiguously displays electronic transitions fingerprinting *J*- and *H*- type aggregates, where porphyrin molecules inter-

molecularly interact in head-to-tail and face-to-face fashion, respectively. Multilayered-type devices were also engineered with the aim of investigating the interaction of the porphyrin-derived DWCNTs with polymer poly(3-hexylthiophene)-pyrene (P3HT) derivatives containing small amounts of [60]PCBM. Studies of asymmetric current density-voltage (*J-V*) with the investigated **1@(1-DWCNTs)** hybrid displayed a strong rectification effect corroborating state-of-the-art devices.

5.2 Porphyrin-Fullerenes conjugated system

Fullerene, as similar to CNTs, shows exceptional properties such as conductivity, crystalinity and mechanical strength. In particular, their solubility in organic solvents and trouble-free processability rendered better realization of C_{60} applications in photovoltaic cells. Among the numerous fullerene-based photoactive molecular devices reported so far, systems combining fullerene accepting moieties with porphyrin donors have generated a great deal of attention.[71,72] Spectacular covalent and non-covalent fullerene-porphyrin conjugates have been already prepared and systematic studies of their electronic properties revealed interesting photoinduced processes.[71,72] Importantly, accelerated charge separation and decelerated charge recombination has been evidenced in a fullerene-based acceptor-donor system when compared to the equivalent benzoquinone-based system.[73] This has been interpreted by the smaller reorganization energy (λ) of C_{60} when compared with those of small acceptors.[73] The efficient photogeneration of long lived charge-separated states by photoinduced electron transfer in fullerene-porphyrin systems is particularly interesting for solar energy conversion. Indeed, photovoltaic devices prepared from such hybrid compounds have shown promising energy conversion efficiencies.[38,74,75] On the other hand, strong attractive fullerene-porphyrin interactions have been evidenced for several covalent and non-covalent C_{60}-porphyrin derivatives,[76,77] as well as in the solid state structures of porphyrin/fullerene co-crystals.[78] The establishment of such intramolecular π-stacking interactions between the two chromophores has been demonstrated spectroscopically both in the ground and in the excited state. In particular, charge transfer (CT) excited state levels in the near-infrared (NIR) region have been evidenced, which are typically the funnel of the excitation energy initially addressed to upper electronic states localized on each chromophore.

In this chapter, we report a C_{60}-porphyrin conjugate prepared using a fullerene-azide building block and a porphyrin derivative bearing alkyne units. The electrochemical and photophysical characterization of the hybrid compound are discussed in detail.

5.2.1 Synthesis of Porphyrin-Fulerene conjugated system

The preparation of the fullerene-azide building block is depicted in **Scheme 5.2.1.** This compound was obtained by taking advantage of the regioselective reaction developed in the group of Diederich,[79] which led to macrocyclic bis-adducts of C_{60} by a cyclization reaction at the fullerene sphere with a bis-malonate derivative in a double Bingel cyclopropanation.[80]

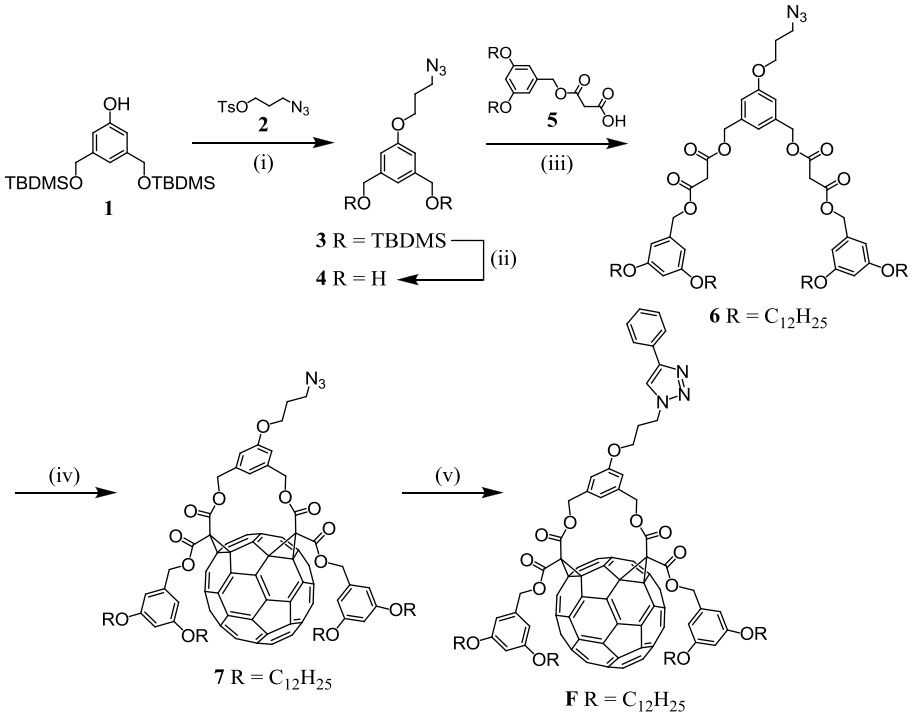

Scheme 5.2.1 *Reagents and conditions: (i) K_2CO_3, LiBr, DMF, 80°C, 96 h (33%); (ii) TBAF, THF, 0°C, 3 h (73%); (iii) DCC, DMAP, HOBt, CH_2Cl_2, 0°C to r.t., 72 h (65%); (iv) C_{60}, DBU, I_2, PhMe, r.t., 12 h (56%); (v) phenylacetylene, $CuSO_4.5H_2O$, sodium ascorbate, CH_2Cl_2/H_2O, r.t., 16 h (73%).*

The ^{1}H NMR spectrum of **7** reveals the characteristic features of C_s symmetrical 1,3-phenylenebis(methylene)-tethered fullerene *cis-2* bis-adducts.[81] Effectively, two AB quartets are observed for the two sets of diastereotopic benzylic CH_2 groups (H-A/B and H-C/D) and an AX_2 system is revealed for the aromatic protons of the 1,3,5-trisubstituted bridging phenyl ring (H-3/4). The ^{13}C NMR spectrum of **7** is also in full accordance with the proposed molecular structure. In particular, four of the resonances seen between □ = 134 and 148 ppm for the different fullerene sp^2 C atoms show half intensity (□ = 134.6, 138.0, 147.5 and 147.6). Actually, the latter observation is an unambiguous proof for the C_s symmetry[81] of compound **7**. Effectively, for such a C_{60} derivative, there are 26 pairs of equivalent sp^2 fullerene C atoms and four unique ones. Additionally, the orange-red color and the UV/Vis spectrum of **7** are fully consistent with those of previously reported analogous *cis-2* bis-adducts.[82] Indeed, the absorption spectra of C_{60} bis-adducts are characteristic for each of the regioisomers.[79,83] It is also well-established that the 1,3-

phenylenebis(methylene)-tethered bis-malonates produce regioselectively the C_s symmetrical *cis-2* addition pattern at C_{60}.[79,81,82] It is also worth noting that fullerene azide derivative **7** is a quite stable compound under normal laboratory conditions. A sample was stored in the fridge for several months without any detectable decomposition. The latter observation is quite unusual for fullerene-azide derivatives for which intermolecular cycloaddition reactions between the C_{60} and the azide groups led generally to fast decomposition.[84] The remarkable stability of compound **7** may be the result of the encapsulation of the fullerene sphere in its cyclic addend surrounded by two 3,5-didodecylbenzyl ester moieties thus preventing the reaction of the azide group with the C_{60} core. Treatment of compound **7** with phenylacetylene in the presence of $CuSO_4.5H_2O$ and sodium ascorbate in a mixture of CH_2Cl_2/H_2O (1/1) gave the clicked model compound **F** in 73% yield. As previously observed for click reactions with fullerene-based building blocks, azide cycloaddition on the C_{60} core does not significantly compete with the alkyne-azide click reaction leading to the 1,2,3-triazole derivatives. Compound **F** is highly soluble in common organic solvent and was thus easily characterized. The structure of compound **F** was confirmed by its ^1H and ^{13}C NMR spectra as well as by mass spectrometry. Inspection of the ^1H NMR spectrum clearly indicates the disappearance of the CH_2-azide (H-7) signal at δ = 3.55 ppm. Importantly, the ^1H NMR spectrum of **F** shows the typical singlet of the 1,2,3-triazole unit (H-8) at δ = 7.80 ppm as well as the signal corresponding to the CH_2-triazole protons (H-7) at δ = 4.65 ppm.

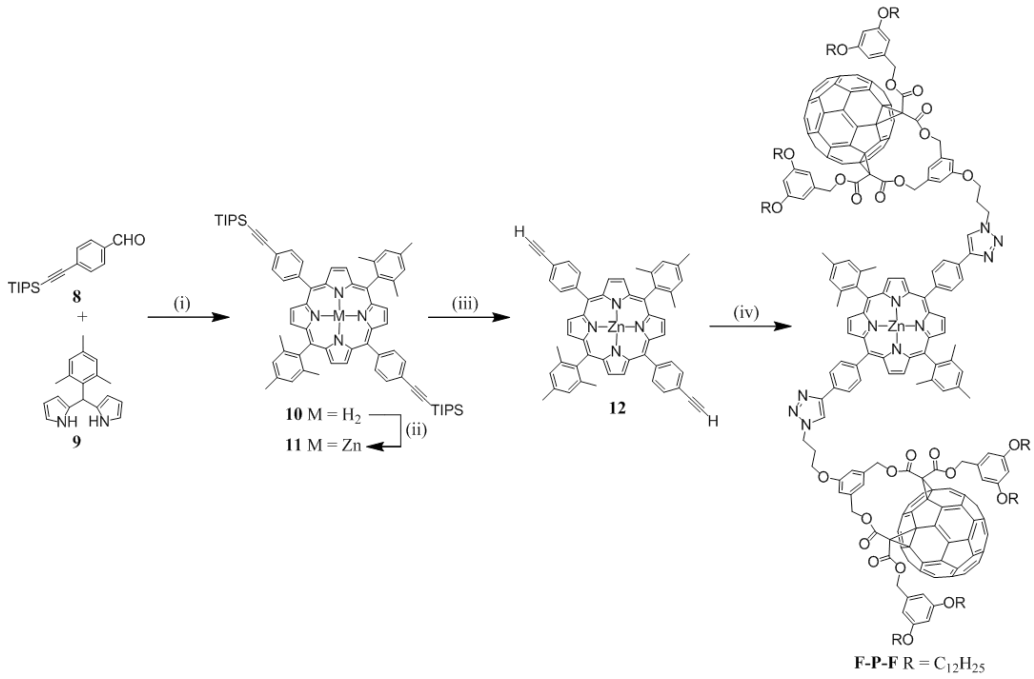

Scheme 5.2.2 *Reagents and conditions: (i) $BF_3.Et_2O$, $CHCl_3$, r.t., 16 h, then p-chloranil, Δ, 2 h (23%); (ii) $Zn(OAc)_2$, MeOH/$CHCl_3$, Δ, 2 h (95%); (iii) TBAF, THF, 0°C, 2 h (94%); (iv) 7, $CuSO_4.5H_2O$, sodium ascorbate, CH_2Cl_2/H_2O, r.t., 1 h (64%).*

The synthesis of the porphyrin building block bearing two clickable terminal alkyne units (**12**) is depicted in **Scheme 5.2.2**. Compound **8**[85] and dipyrromethane **9**[86] were prepared according to previously reported methods. Porphyrin **10** was obtained by using the reaction conditions developed in the group of Lindsey.[87] The condensation of **8** and **9** was performed in $CHCl_3$ (commercial $CHCl_3$ containing 0.75% ethanol as stabilizer) at room temperature in the presence of $BF_3.Et_2O$. After 16 hours, *p*-chloranil (tetrachlorobenzoquinone) was added to irreversibly convert the porphyrinogen to the porphyrin. The desired tetraphenylporphyrin **10** was subsequently isolated in 23% yield. Metalation of **10** with $Zn(OAc)_2$ and treatment of the resulting **11** with TBAF gave compound **12**.

The conformation adopted by compound **F-P-F** is an important issue for a better understanding of the photophysical properties. Indeed, the flexible linkers between the central porphyrin moiety and the two peripheral fullerene subunits may allow for either a fully extended or a folded conformation. The calculated structure of compound **F-P-F** depicted in **Figure 5.2.1** reveals that π-stacking interactions between the fullerene moieties and the central porphyrinic core take place in a folded conformation.

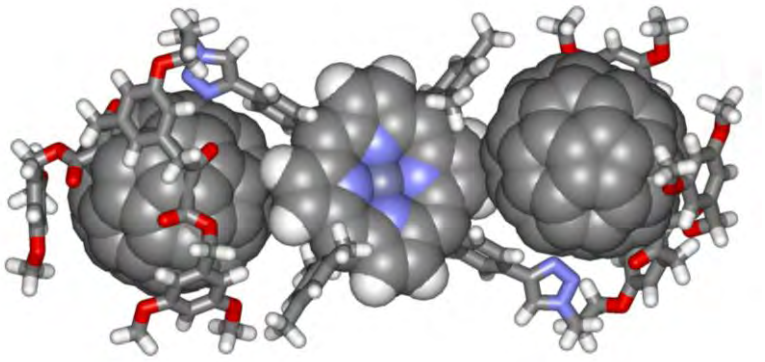

Figure 5.2.1 *Calculated structure of* ***F-P-F*** *(molecular modeling performed with Spartan at the PM3 level, the dodecyl chains have been replaced by methyl groups in the calculations).*

Such attractive interactions between fullerenes and porphyrins have been already observed for several covalent and non-covalent C_{60}-porphyrin conjugates[76,77] and may contribute to stabilize the folded conformation in the case of **F-P-F**. This view is indeed supported by the 2D NOESY spectrum of **F-P-F** recorded in $CDCl_3$ at room temperature. Effectively, correlation peaks are observed between the 1,2,3-triazole proton (H-8) and both CH_2-5 and CH_2-7 groups of the propylene. The latter observation clearly reveals that CH_2-5 is spatially close to proton H-8. This is obviously possible only if compound **F-P-F** adopts a folded conformation. In the calculated structure, the distance between proton H-8 and its closest neighbor in the CH_2-5 unit is 3.29 Å for one 1,2,3-triazole ring and 4.36 Å for the other one in perfect agreement with the observed NOE

effects. Further correlation peaks observed between the protons of the mesityl groups (CH_3 and H-a) and some of the CH_2 moieties of the dodecyl chains are also consistent with a folded conformation. However, compound **F-P-F** being not a rigid molecule, this conclusion refers not to a fixed structure but to an energetically preferred conformation in this particular solvent ($CDCl_3$) resulting from attractive intramolecular fullerene-porphyrin interactions. It can be noted that the occurrence of such interactions are further supported by (i) the slight red-shift observed for the Soret band in the absorption spectrum of **F-P-F** when compared to model porphyrin **P**, and (ii) the observation of a NIR charge transfer emission upon photoexcitation in toluene (*vide infra*).

5.2.2 Electrochemical studies

The electrochemical properties of **F-P-F** were determined by cyclic voltammetry (CV) and Osteryoung Square Wave Voltammetry (OSWV). For the sake of comparison, electrochemical measurements have also been carried out with **F**, **12** and **P**. All the experiments were performed at room temperature in CH_2Cl_2 solutions containing tetra-*n*-butylammonium tetrafluoroborate (0.1 M) as supporting electrolyte and ferrocene (Fc) as internal reference, with a Pt wire as the working electrode and a saturated calomel electrode (SCE) as a reference. Potential data for all of the compounds are collected in **Table 5.2.1**. As a typical example, the cyclic voltammogram showing the first oxidation as well as the first reduction of **F-P-F** is depicted in **Figure 5.2.2**.

In the cathodic region, model compound **F** shows the classical behavior observed for fullerene *cis-2* bis-adducts.[88] In addition to the observation of the three successive reductions of the fullerene unit, reduction peaks of electrogenerated products formed after the second reduction are also observed at -1.15 and -1.57 V *vs.* SCE. This specific behaviour of cyclopropanated fullerenes is most probably due to a bond breaking in the cyclopropane ring, known as the retro-Bingel reaction.[83,89] In the anodic region, model compound **F** shows two irreversible peaks which can be likely attributed to the oxidation of the dialkyloxyphenyl and/or 4-phenyl-1,2,3-triazol units.[90] Model compounds **12** and **P** display the characteristic electrochemical behaviour of Zn(II)-porphyrin derivatives with two quasi-reversible porphyrin-centered one-electron transfer processes in both the cathodic and the anodic regions. The voltammograms recorded for hybrid compound **F-P-F** show the characteristic electrochemical features of both constitutive units, *ie.* fullerene and Zn(II)-porphyrin.

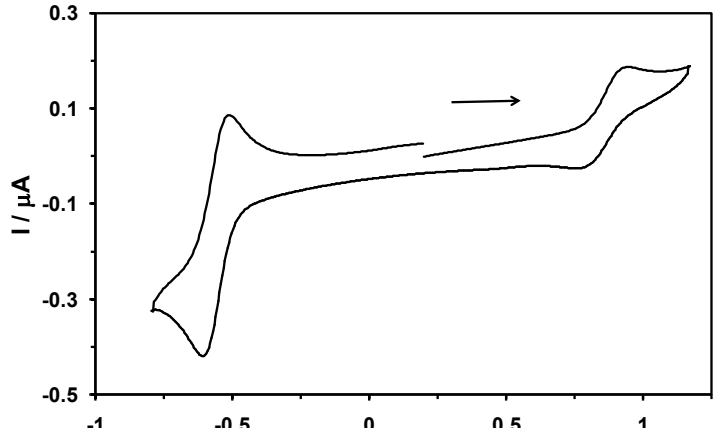

Figure 5.2.2 *Cyclic Voltammogram of compound* ***F-P-F*** *on a Pt electrode at v = 0.1 Vs^{-1} in CH_2Cl_2 + 0.1 M n-Bu_4NBF_4.*

Table 5.2.1 *Electrochemical data of* ***F***, ***P***, ***12*** *and* ***F-P-F*** *determined by OSWV on a Pt working electrode in CH_2Cl_2 + 0.1 M nBu_4NBF_4 at room temperature in the presence of ferrocene used as internal reference.*[a,b]

	Oxidation			Reduction				
	E_3	E_2	E_1	E_1	E_2	E_3	E_4	E_5
F		+1.97	+1.69	-0.55	-0.87	-1.15[c]	-1.35	-1.57[c]
12		+1.19	+0.91	-1.31	-1.71			
P		+1.20	+0.86	-1.40	-1.62			
F-P-F	+1.76	+1.26	+0.88	-0.56	-0.86	-1.15[c]	-1.33	-1.56[c]

[a] *OSWVs were obtained using a sweep width of 20 mV, a frequency of 10 Hz, and a step potential of 5 mV.*
[b] *Values in V vs. SCE (Fc^+/Fc is observed at +0.55 ± 0.01 V vs. SCE).*
[c] *Waves corresponding to an electrogenerated species obtained after the second fullerene-centered reduction step.*

The comparison of the redox potentials of **F-P-F** with the corresponding model compounds clearly shows that the three first reduction waves correspond to fullerene-centered processes, while the two first oxidation processes are centered on the porphyrin core. The fourth reduction process probably contains contributions from both C_{60} and porphyrin moieties. Finally, the fifth peak corresponds most likely to a fullerene-centered reduction. As shown in **Figure 5.2.2**, the two fullerene subunits behave as independent redox centers and the relative intensity of the first fullerene-reduction relative to the first porphyrin-based oxidation is in the expected 2:1 ratio. Comparison of the redox potentials values of **F-P-F** with those of the corresponding model compounds **F** and **P** reveals only a minor influence of the fullerene subunits on the porphyrin moiety and *vice versa*. This observation however does not indicate the absence of intramolecular

fullerene-porphyrin interactions (*vide supra*). Effectively, redox potentials of fullerene-donor conjugates are generally very weakly affected by intramolecular π-π interactions even in cyclic systems in which the two components are forced to be at the van der Waals contact.[91]

5.2.3 Photophysical studies

5.2.3.1 Ground state absorption and luminescence properties

The electronic absorption spectra of model compounds **F** and **P**, and fullerene-porphyrin conjugate **F-P-F** in toluene are shown in **Figure 5.2.3**a. Below 390 nm, the fullerene absorption is stronger than that of the porphyrin, whereas in the visible spectral region an opposite pattern is observed. The spectrum of **P** is quite similar to that of Zn(II) *meso*-tetraphenylporphyrin (ZnTPP).[92] This is an expected result since the side group on the *meso*-phenyl rings does not affect much the delocalization of the porphyrin π-systems. The maximum of the Soret band, corresponding to the transition to the second singlet excited state, is located at 424 nm (ε = 521 000 M^{-1} cm^{-1}) in toluene.

In the UV region, the absorption spectrum of **F-P-F** exhibits minor differences when compared with the sum of the spectra of the corresponding model compounds. In contrast, significant differences can be observed in the Vis region. In particular, a slight red-shift (λ_{max} = 426 nm) as well as an intensity decrease of the Soret band (ε = 434 000 M^{-1} $cm^{-}1$) are observed. This may suggest some interactions between at least one of two fullerenes with the porphyrin macrocycle. This kind of behavior has been typically found in systems with a face-to-face porphyrin-fullerene interchromophoric arrangement.[93] Compared to the algebraic sum of the components, **F-P-F** also exhibits a concentration-independent weak tail of the absorption profile above 650 nm, which is a further clue for ground state charge transfer interaction between the two chromophores, in line with previous reports (**Figure 5.2.3a**).[45] The most relevant luminescence data for all the investigated compounds are reported in **Table 5.2.2**, where the emission maxima refer to the spectra corrected for the detector response.

In toluene solution at room temperature, **P** exhibits a fluorescence band (λ_{max} = 645 nm, τ_S = 2.1 ns, Φ_{fl} = 2.4 %); at 77 K both fluorescence and phosphorescence are detected (**Table 5.2.2, Figure 5.2.3b**). The porphyrin fluorescence intensity of **F-P-F** is quenched by about 75% when compared to **P** at 298 K (**Table 5.2.2**), and the lifetime is accordingly reduced from 2.1 to 1.0 ns, corresponding to a quenching rate constant of 5.2 x 10^8 s^{-1}. The quenching process can be attributed to singlet energy transfer to the fullerene moiety, in line with literature reports for

analogous multichromophoric fullerene-porphyrin systems in apolar media;[75] this hypothesis will be verified in the next sections.

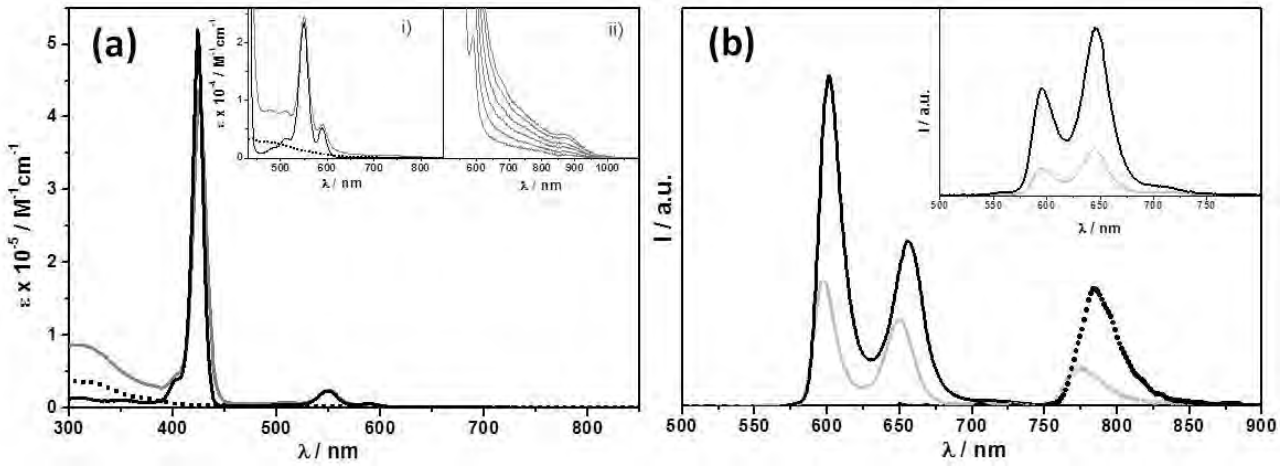

Figure 5.2.3 *(a) Absorption spectra of* ***F-P-F*** *(grey),* ***F*** *(dotted black), and* ***P*** *(black) in toluene solution at 298 K; insets i) zoom of Q band region and ii) absorption spectra of* ***F-P-F*** *in NIR region at various concentrations ([**F-P-F**] = 7.4 - 46 μM). (b) Corrected emission spectra of* ***F-P-F*** *(fluorescence: grey, phosphorescence: dotted grey) and* ***P*** *(fluorescence: black, phosphorescence: dotted black) in toluene solution at 77 K. Inset: fluorescence at 298 K.*

Table 5.2.2 *Luminescence data in toluene and benzonitrile*

Compounds	Toluene					Benzonitrile				
	298 K			77 K		298 K			77 K	
	λ_{max} [a] (nm)	τ (ns)	Φ_{em} (%)	λ_{max} [a] (nm)	λ_{max} [b] (nm)	λ_{max} [a] (nm)	τ (ns)	Φ_{em} (%)	λ_{max} [a] (nm)	λ_{max} [b] (nm)
F	700	1.6	~0.01			700	1.5	~0.01		
P	645	2.1	2.4	602	784	606	1.9	2.9	607	800
F-P-F	645	1.0	0.60	597	775	609	1.1	1.0	607	-[c]

[a] *Fluorescence: from corrected emission spectra;* [b] *Phosphorescence;* [c] *Not detected*

In **F-P-F** the porphyrin quenching turns out to be relatively slow compared to previously investigated similar arrays due to the long through bong distance between the energy donor and acceptor, assuming an extended conformation. Also a weak phosphorescence signal (quenched by about 65%) is still observable for **F-P-F** (λ_{max} = 786 nm, τ_T = 20 ms) at 77 K. The typical weak fluorescence band is observed for the bismethanofullerene reference compound **F** (λ_{max} = 700 nm, τ_S = 1.6 ns). This band cannot be observed in **F-P-F** because of the spectral overlapping with the residual porphyrin emission, still much more intense, even when excitation is addressed mainly to

the fullerene moiety (λ_{exc} = 380 nm). In benzonitrile solution at room temperature, the porphyrin fluorescence is quenched to a similar extent as in toluene, both in intensity and lifetime (**Table 5.2.2**), also suggesting a relatively slow quenching process, as found in toluene. Interestingly, the porphyrin phosphorescence at low temperature in this solvent could not be detected for **F-P-F**.

5.2.3.2 Singlet oxygen sensitization and NIR emission

In order to trace the formation of porphyrin and/or fullerene triplets,[94] we measured the sensitized singlet oxygen ($^1O_2$*) luminescence at 1270 nm in toluene. Setting *meso*-tetraphenylporphyrin (TPP) as standard, which displays a singlet oxygen sensitization yield (Φ_Δ) equal to 0.70[34] in toluene solution, we measured values of 0.70 for **P**, 0.60 for **F** and 0.45 for **F-P-F**. The formation of singlet oxygen in **F-P-F** is in line with the finding of extensive formation of fullerene triplet in toluene by transient absorption spectroscopy (*vide infra*). By contrast, no sensitized $^1O_2$* luminescence is detected in benzonitrile solution by exciting **F-P-F (Figure 5.2.4)**. This suggests that different photoinduced processes occur in the multicomponent array in the two solvents, as it will be evidenced by transient absorption studies.

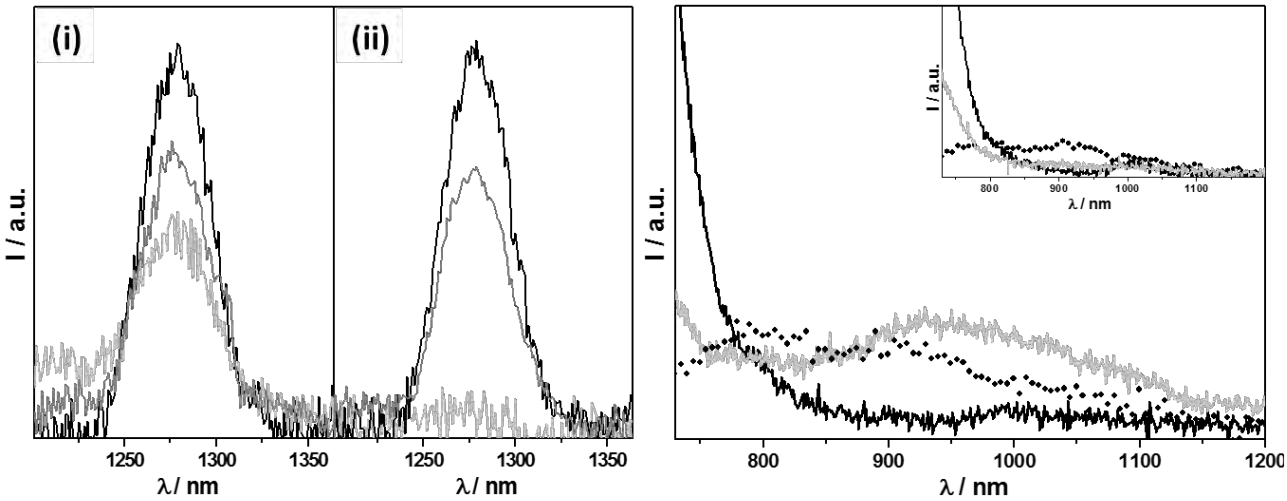

Figure 5.2.4 *Left: Corrected singlet oxygen luminescence spectra of air-equilibrated solution containing* ***P*** *(black),* ***F*** *(gray) and* ***F-P-F*** *(light gray). i) toluene: λ_{exc} = 550 nm, A = 0.300. ii) benzonitrile: λ_{exc} = 560 nm, A = 0.300. Right: Emission spectra in the near infrared spectral region at 298 K in toluene of* ***F-P-F*** *(grey),* ***F*** *(dotted black) and* ***P*** *(black) upon excitation at 550 nm, A = 0.300. Inset: in benzonitrile.*

Interestingly, **F-P-F** exhibits a weak and broad emission band centered at ca. 950 nm in toluene solution (**Figure 5.2.4**); its faint intensity prevented the determination of the lifetime. In analogy with previous findings in face-to-face porphyrin-fullerene systems[45,93] this band is attributed to an emitting charge transfer state that can be generated by a minority of **F-P-F** systems, in the frame of a dynamic equilibrium, in which the two chromophores are in a close

edge-to-face conformation. The excitation spectrum of **F-P-F** taken at 950 nm showed the typical spectral features of a porphyrin moiety, and particularly the diagnostic Soret band at ca. 420 nm and Q bands at 550 nm. This rules out that the observed NIR band is due to exciplex emission and suggests that the porphyrin excited states are partly deactivated to a low-lying CT level. The fact that the absorption tail above 650 nm (ε = 375 $M^{-1}cm^{-1}$) is weaker than those previously observed[45,93] suggests that only a minor fraction of molecules are involved in the edge-to-face interactions, contrary to what happened in face-to-face systems where molecules engaged in CT interactions are the large majority.[45] In benzonitrile solution, under steady state irradiation at the porphyrin Q bands, no NIR emission such as that in **Figure 5.2.4** is detected for **F-P-F**. This is not surprising since CT luminescence has never been observed previously for face-to-face systems in this solvent, due to the energy gap law (lower CT energy, faster nonradiative deactivation rates) or to the fact that the charge recombination (CR) process of the porphyrin-fullerene pairs is highly exergonic and lies in the Marcus inverted region.[93] Under this regime, CR processes are expected to be faster in more polar media (i.e. benzonitrile *vs.* toluene), owing to a decrease of the activation energy for charge recombination.[44]

In summary, **F-P-F** shows clear evidence of interchromophoric excited state interactions. The porphyrin centered fluorescence is quenched, while a new CT emission band in the near infrared spectral region is recorded in toluene solution. However, the main deactivation pathway in apolar toluene leads to the formation of the fullerene triplet, which most likely occurs through porphyrin⟶fullerene singlet energy transfer, followed by regular intersystem crossing within the carbon sphere, as observed in many fullerene dyads.[94]

5.2.3.3 Transient absorption spectroscopy

The nanosecond transient absorption spectrum of **P** shows the typical zinc porphyrin triplet absorption spectra (λ_{max} = 460 nm); its lifetime is 177 and 130 μs in deoxygenated benzonitrile and toluene solutions, respectively. The nanosecond transient absorption spectrum of **F** in benzonitrile shows the characteristic triplet-triplet absorption band (λ_{max} = 720 nm).[95-97] A first order decay with lifetime of 24 μs is found, which is non-radiative $T_1 \longrightarrow S_0$ deactivation process of **F.**

The shape of the nanosecond transient absorption spectrum of **F-P-F** in benzonitrile (**Figure 5.2.4**) is very different from that of its model compounds. Immediately after excitation of **F-P-F** with 560 nm laser pulse, where the porphyrin component is selectively excited with a ratio of about 10:1 with respect to fullerene, the bleaching of the ground state porphyrin Q-bands at 550

and 600 nm and an intense absorption of the porphyrin triplet at 470 nm are recorded. With an increase of delay time, spectral changes in the absorptions at ca. 650 and 1005 nm arise and decay simultaneously with τ = 0.48 μs (**Figure 5.2.4**). We assign the absorption band around 650 to zinc porphyrin radical cation ($ZnP^{\cdot+}$)[98] and that around 1005 nm to the bismethanofullerene radical anion ($C_{60}^{\cdot-}$),[99,100] respectively. The identical lifetimes, within the experimental uncertainty, indicate that the same species is monitored, namely the charge separated state. The rise time of the charge separated state is about 20 ns, which rules out a role of the singlet levels as reacting species and indicates that the ion pair is formed by the fullerene triplet. This is fully reasonable on the basis of the electrochemical data, which indicate that the energy of the charge separated state is 1.44 eV in CH_2Cl_2, and must be somewhat lower in more polar benzonitrile, which is compatible with triplet energy of bismethanofullerenes of 1.40 eV.[94] Indeed the porphyrin centred triplet state is detected at around 480 nm in **F-P-F**, which decays with $\tau \sim 30$ ns; this suggests some residual electron transfer from the porphyrin centered triplet state, populated via intersystem crossing. The absence of formation of long-lived triplet species either in the porphyrin or the fullerene chromophores is verified by the absence of sensitized singlet oxygen luminescence at 1270 nm in air equilibrated benzonitrile solution as well as by the lack of phosphorescence at 77 K (*vide supra*).

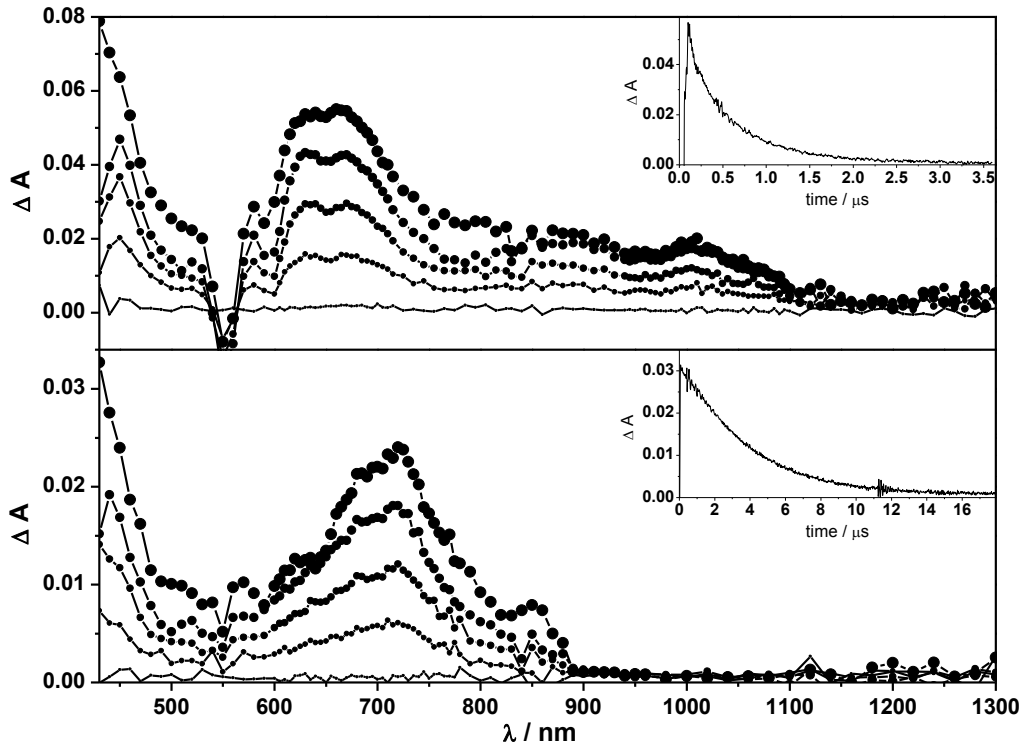

Figure 5.2.5 *Top: transient absorption spectra of* ***F-P-F*** *in oxygen-free benzonitrile. Depicted spectral traces are at 0.1, 0.16, 0.34, 0.70, 2.5 μs (from bigger to smaller circles) after the laser pulse. Inset: absorption decay at 650 nm.* λ_{exc} *= 560 nm. Energy: 1.0 mJ per pulse. Bottom: transient absorption spectra of* ***F-P-F*** *in oxygen-free*

toluene, 5 x 10^{-5} M. Depicted spectral traces are at 0.1, 1.2, 2.8, 5.3, 16 μs (from bigger to smaller circles) after the laser pulse. Inset: absorption decay at 720 nm. λ_{exc} = 560 nm. Energy: 2.0 mJ per pulse.

For **F-P-F** in toluene, no charge separated state is detected in the nanosecond regime (**Figure 5.2.5**). In a timescale below our experimental resolution, i.e. less than 10 ns, the growth of the fullerene triplet is detected at 720 nm, upon excitation of the porphyrin moiety. This dynamics is compatible with the quenching of the porphyrin singlet detected via fluorescence spectroscopy (k = 5.2 x 10^8 s^{-1}, see above). The fact that (i) the quenched porphyrin singlet lifetimes are identical in toluene and benzonitrile, despite a completely different excited state reactivity and (ii) singlet levels do not feed electron transfer in benzonitrile are robust clues for porphyrin→fullerene singlet energy transfer in both media as the primary photoinduced event.

The fullerene triplet lifetime is 3.8 and 0.34 μs in deoxygenated and air-equilibrated solution, respectively. Interestingly, the fullerene triplet lifetime of **F-P-F** (3.8 μs) is significantly reduced relative to that of the model fullerene **F** (20 μs) in oxygen-free solution. This suggests that a dynamic quenching of the long lived fullerene triplet states in **F-P-F** occurs, with a rate constant of 2.1 x 10^5 s^{-1}. This could be a consequence of a dynamic equilibrium that, on the microsecond time scale, would allow the deactivation of the fullerene triplet states in **F-P-F** with an extended conformation (majority) to the lower-lying CT species (minority).[45] To further strengthen the hypothesis of such a dynamic equilibrium between compact and extended conformations, it can be noted that the Φ_Δ value of **F-P-F** (0.45) is slightly smaller than that of **F** (0.60), again suggesting the presence of a minority of CT states that are known to be incapable of sensitizing the formation of $^1O_2$*.[44]

The photoinduced intramolecular processes evidenced for **F-P-F** in both solvents (toluene and benzonitrile) can be summarized as follows. In toluene, no long lived charge separated state could be detected by nanosecond transient absorption spectroscopy. On the other hand, efficient singlet energy transfer from the porphyrin to the fullerene excited states followed by population of the fullerene triplet level is evidenced by time resolved absorption and luminescence experiments. The triplet state character of the observed excited state was further confirmed by the singlet oxygen sensitization measurements. Moreover, a porphyrin-fullerene charge transfer interactions was evidenced by a broad and weak emission band at around 940 nm. This kind of interaction can only be set up through very tight porphyrin/fullerene pair configurations, which, in the present case can be only face-to-edge and not face-to-face as observed previously.[93] This species is present only as a minor fraction, in the frame of a dynamic equilibrium. The quenching of the fullerene centered triplet state in **F-P-F** in oxygen free solution is also a good indication of this hypothesis. In benzonitrile, no emission in the NIR region could be detected, but

photoinduced electron transfer was unambiguously evidenced, since the free-radical ions $P^{\bullet+}$ and $F^{\bullet-}$ were identified by flash spectroscopy.

5.2.4 Summary

In this part of the chapter, we have reported a stable C_{60} derivative bearing an azide functional group allowing its further functionalization by reaction with terminal alkynes under the copper mediated Huisgen 1,3-dipolar cycloaddition conditions. This building block has been used for the preparation of fullerene-porphyrin conjugate **F-P-F** by reaction with a Zn(II)-porphyrin bearing two terminal alkyne units. Molecular modeling and 2D NOESY experiments on the resulting hybrid system have revealed a folded conformation stabilized by intramolecular π-stacking interactions between the fullerene moieties and the central porphyrinic core. The electrochemical properties of hybrid compound **F-P-F** have been investigated. Whereas the first reduction is centered on the C_{60} unit, the oxidation is centered on the porphyrin moiety. Photophysical studies revealed strong excited state interactions between the different components in **F-P-F**. Indeed, intramolecular photoinduced processes have been evidenced by steady-state fluorescence spectroscopy and time-resolved absorption and luminescence techniques. In a polar solvent such as benzonitrile, **F-P-F** undergoes an efficient photoinduced electron transfer from both fullerene and porphyrin triplet levels. The resulting charge separated state is relatively long lived (τ = 0.48 μs). In contrast, intramolecular energy transfer has been evidenced in apolar toluene. Interestingly, a conformational equilibrium allowing an intramolecular porphyrin-fullerene π-π interaction is responsible for the dynamic quenching of the fullerene centered triplet state that populates a CT state from which a NIR emission could be detected.

5.3 References

1. N. Armaroli and V. Balzani, *Energ. Environ. Sci.*, **2011**, *4*, 3193-3222.
2. M. Granstrom, K. Petritsch, A. C. Arias, A. Lux, M. R. Andersson and R. H. Friend, *Nature*, **1998**, *395*, 257-260.
3. J. J. M. Halls, C. A. Walsh, N. C. Greenham, E. A. Marseglia, R. H. Friend, S. C. Moratti and A. B. Holmes, *Nature*, **1995**, *376*, 498-500.
4. J.-L. Bredas and J. R. Durrant, *Acc. Chem. Res.*, **2009**, *42*, 1689-1690.
5. Solarmer Energy, Inc., http://www.solarmer.com/.
6. G. C. Bazan, J. Peet, J. Y. Kim, N. E. Coates, W. L. Ma, D. Moses and A. J. Heeger, *Nat. Mater.*, **2007**, *6*, 497-500.

7. C. N. Hoth, P. Schilinsky, S. A. Choulis and C. J. Brabec, *Nano Lett.*, **2008**, *8*, 2806-2813.
8. K. Vandewal, K. Tvingstedt, A. Gadisa, O. Inganas and J. V. Manca, *Nat. Mater.*, **2009**, *8*, 904-909.
9. R. H. Baughman, A. A. Zakhidov and W. A. de Heer, *Science*, **2002**, *297*, 787-792.
10. T. W. Ebbesen, H. J. Lezec, H. Hiura, J. W. Bennett, H. F. Ghaemi and T. Thio, *Nature*, **1996**, *382*, 54-56.
11. A. A. Mamedov, N. A. Kotov, M. Prato, D. M. Guldi, J. P. Wicksted and A. Hirsch, *Nat. Mater.*, **2002**, *1*, 257-257.
12. C. Q. Sun, H. L. Bai, B. K. Tay, S. Li and E. Y. Jiang, *J. Phys. Chem. B*, **2003**, *107*, 7544-7546.
13. D. M. Guldi, G. M. A. Rahman, V. Sgobba and C. Ehli, *Chem. Soc. Rev.*, **2006**, *35*, 471-487.
14. R. C. Haddon, *Acc. Chem. Res.*, **2002**, *35*, 997-997.
15. V. Sgobba and D. M. Guldi, *Chem. Soc. Rev.*, **2009**, *38*, 165-184.
16. M. A. Green, K. Emery, Y. Hishikawa and W. Warta, *Prog. Photovolt: Res. Appl.*, **2011**, *19*, 84-92.
17. D. Baskaran, J. W. Mays, X. P. Zhang and M. S. Bratcher, *J. Am. Chem. Soc.*, **2005**, *127*, 6916-6917.
18. S. Campidelli, C. Sooambar, E. L. Diz, C. Ehli, D. M. Guldi and M. Prato, *J. Am. Chem. Soc.*, **2006**, *128*, 12544-12552.
19. J. Jin, Z. P. Dong, J. G. He, R. Li and J. T. Ma, *Nanoscale Res. Lett.*, **2009**, *4*, 578-583.
20. H. Li, R. B. Martin, B. A. Harruff, R. A. Carino, L. F. Allard and Y. P. Sun, *Adv. Mater.*, **2004**, *16*, 896-900.
21. Z. B. Liu, J. G. Tian, Z. Guo, D. M. Ren, T. Du, J. Y. Zheng and Y. S. Chen, *Adv. Mater.*, **2008**, *20*, 511-515.
22. T. Palacin, H. Le Khanh, B. Jousselme, P. Jegou, A. Filoramo, C. Ehli, D. M. Guldi and S. Campidelli, *J. Am. Chem. Soc.*, **2009**, *131*, 15394-15402.
23. J. Y. Chen and C. P. Collier, *J. Phys. Chem. B*, **2005**, *109*, 7605-7609.
24. F. Y. Cheng, S. Zhang, A. Adronov, L. Echegoyen and F. Diederich, *Chem.-Eur. J.*, **2006**, *12*, 6062-6070.
25. K. S. Chichak, A. Star, M. V. R. Altoe and J. F. Stoddart, *Small*, **2005**, *1*, 452-461.
26. R. Chitta, A. S. D. Sandanayaka, A. L. Schumacher, L. D'Souza, Y. Araki, O. Ito and F. D'Souza, *J. Phys. Chem. C*, **2007**, *111*, 6947-6955.
27. C. Ehli, G. M. A. Rahman, N. Jux, D. Balbinot, D. M. Guldi, F. Paolucci, M. Marcaccio, D. Paolucci, M. Melle-Franco, F. Zerbetto, S. Campidelli and M. Prato, *J. Am. Chem. Soc.*, **2006**, *128*, 11222-11231.
28. D. M. Guldi, G. M. A. Rahman, M. Prato, N. Jux, S. H. Qin and W. Ford, *Angew. Chem. Int. Ed.*, **2005**, *44*, 2015-2018.
29. T. Hasobe, S. Fukuzumi and P. V. Kamat, *J. Am. Chem. Soc.*, **2005**, *127*, 11884-11885.
30. H. P. Li, B. Zhou, Y. Lin, L. R. Gu, W. Wang, K. A. S. Fernando, S. Kumar, L. F. Allard and Y. P. Sun, *J. Am. Chem. Soc.*, **2004**, *126*, 1014-1015.
31. H. Murakami, T. Nomura and N. Nakashima, *Chem. Phys. Lett.*, **2003**, *378*, 481-485.
32. G. M. A. Rahman, D. M. Guldi, S. Campidelli and M. Prato, *J. Mater. Chem.*, **2006**, *16*, 62-65.

33. J. K. Sprafke, S. D. Stranks, J. H. Warner, R. J. Nicholas and H. L. Anderson, *Angew. Chem. Int. Ed.*, **2011**, *50*, 2313-2316.
34. J. L. Delgado, M. A. Herranz and N. Martin, *J. Mater. Chem.*, **2008**, *18*, 1417-1426.
35. A. Hirsch, *Angew. Chem. Int. Ed.*, **2002**, *41*, 1853-1859.
36. P. Singh, S. Campidelli, S. Giordani, D. Bonifazi, A. Bianco and M. Prato, *Chem. Soc. Rev.*, **2009**, *38*, 2214-2230.
37. D. Tasis, N. Tagmatarchis, A. Bianco and M. Prato, *Chem. Rev.*, **2006**, *106*, 1105-1136.
38. H. Imahori and S. Fukuzumi, *Adv. Funct. Mater.*, **2004**, *14*, 525-536.
39. D. M. Guldi, *J. Phys. Chem. B*, **2005**, *109*, 11432-11441.
40. D. M. Guldi, G. M. A. Rahman, F. Zerbetto and M. Prato, *Acc. Chem. Res.*, **2005**, *38*, 871-878.
41. T. Hasobe, *Phys. Chem. Chem. Phys.*, **2010**, *12*, 44-57.
42. T. Hasobe, S. Fukuzumi and P. V. Kamat, *J. Phys. Chem. B*, **2006**, *110*, 25477-25484.
43. H. Imahori and T. Umeyama, *J. Phys. Chem. C*, **2009**, *113*, 9029-9039.
44. N. Armaroli, G. Accorsi, F. Y. Song, A. Palkar, L. Echegoyen, D. Bonifazi and F. Diederich, *ChemPhysChem*, **2005**, *6*, 732-743.
45. N. Armaroli, G. Marconi, L. Echegoyen, J.-P. Bourgeois and F. Diederich, *Chem.-Eur. J.*, **2000**, *6*, 1629-1645.
46. D. Bonifazi, H. Spillmann, A. Kiebele, M. de Wild, P. Seiler, F. Cheng, H.-J. Güntherodt, T. Jung and F. Diederich, *Angew. Chem. Int. Ed.*, **2004**, *43*, 4759-4763.
47. M. A. Fazio, A. Durandin, N. V. Tkachenko, M. Niemi, H. Lemmetyinen and D. I. Schuster, *Chem.-Eur. J.*, **2009**, *15*, 7698-7705.
48. J. Iehl, M. Vartanian, M. Holler, J.-F. Nierengarten, B. Delavaux-Nicot, J.-M. Strub, A. Van Dorsselaer, Y. Wu, J. Mohanraj, K. Yoosaf and N. Armaroli, *J. Mater. Chem.*, **2011**, *21*, 1562-1573.
49. N. Armaroli, *Fullerenes: From Synthesis to Optoelectronic Properties*, (Eds.: D. M. Guldi, N. Martin), Kluwer Academic, Dordrecht, 2002.
50. K. H. Le Ho, L. Rivier, B. Jousselme, P. Jegou, A. Filoramo and S. Campidelli, *Chem. Commun.*, **2010**, *46*, 8731-8733.
51. This experiment is not possible in DMF, due to insufficient dissolced oxygen content and low diffesion constant
52. The transient decay measuement was not carried out on 1@DWCNT due to poor loading of porphyrins in it.
53. D. L. Akins, H.-R. Zhu and C. Guo, *J. Phys. Chem.*, **1996**, *100*, 5420-5425.
54. Y. Arai and H. Segawa, *Chem. Commun.*, **2010**, *46*, 4279-4281.
55. M. A. Castriciano, A. Romeo, V. Villari, N. Micali and L. M. Scolaro, *J. Phys. Chem. B*, **2003**, *107*, 8765-8771.
56. A. Huijser, B. M. J. M. Suijkerbuijk, R. J. M. Klein Gebbink, T. J. Savenije and Siebbeles, *J. Am. Chem. Soc.*, **2008**, *130*, 2485-2492.
57. X. Li, D. Li, W. Zeng, G. Zou and Z. Chen, *J. Phys. Chem. B*, **2007**, *111*, 1502-1506.

58. G. E. O'Keefe, J. J. M. Halls, C. A. Walsh, G. J. Denton, R. H. Friend and H. L. Anderson, *Chem. Phys. Lett.*, **1997**, *276*, 78-83.
59. J. M. Ribo, J. Crusats, J.-A. Farrera and M. L. Valero, *Chem. Commun.*, **1994**, 681-682.
60. S. Verma, A. Ghosh, A. Das and H. N. Ghosh, *J. Phys. Chem. B*, **2011**, *114*, 8327-8334.
61. M. Kasha, H. R. Rawls and M. A. El-Bayoumi, *Pure Appl. Chem.*, **1965**, *11*, 371 - 392.
62. π-π interactions between porphyrin and DWCNTs are insignificant due to high carboxylic acid functionalities on CNTs surface
63. H. Ago, K. Petritsch, M. S. P. Shaffer, A. H. Windle and R. H. Friend, *Adv. Mater.*, **1999**, *11*, 1281-1285.
64. N. M. Dissanayake and Z. Zhong, *Nano Lett.*, **2011**, *11*, 286-290.
65. E. Kymakis and G. A. J. Amaratunga, *Appl. Phys. Lett.*, **2002**, *80*, 112-114.
66. S. Mitra, C. Li, Y. H. Chen, Y. B. Wang, Z. Iqbal and M. Chhowalla, *J. Mater. Chem.*, **2007**, *17*, 2406-2411.
67. A. F. Nogueira, B. S. Lomba, M. A. Soto-Oviedo, C. R. D. Correia, P. Corio, C. A. Furtado and I. A. Hummelgen, *J. Phys. Chem. C*, **2007**, *111*, 18431-18438.
68. B. Pradhan, S. K. Batabyal and A. J. Pal, *Appl. Phys. Lett.*, **2006**, *88*, 093106-093109.
69. M.-C. Wu, Y.-Y. Lin, S. Chen, H.-C. Liao, Y.-J. Wu, C.-W. Chen, Y.-F. Chen and W.-F. Su, *Chem. Phys. Lett.*, **2009**, *468*, 64-68.
70. E. Klimov, W. Li, X. Yang, G. G. Hoffmann and J. Loos, *Macromolecules*, **2006**, *39*, 4493-4496.
71. R. Chitta and F. D'Souza, *J. Mater. Chem.*, **2008**, *18*, 1440-1471.
72. D. Gust, T. A. Moore and A. L. Moore, *Acc. Chem. Res.*, **2001**, *34*, 40-48.
73. H. Imahori, K. Hagiwara, T. Akiyama, M. Aoki, S. Taniguchi, T. Okada, M. Shirakawa and Y. Sakata, *Chem. Phys. Lett.*, **1996**, *263*, 545-550.
74. S. Fukuzumi and T. Kojima, *J. Mater. Chem.*, **2008**, *18*, 1427-1439.
75. H. Imahori, *J. Phys. Chem. B*, **2004**, *108*, 6130-6143.
76. D. I. Schuster, P. D. Jarowski, A. N. Kirschner and S. R. Wilson, *J. Mater. Chem.*, **2002**, *12*, 2041-2047.
77. N. Solladie, M. E. Walther, M. Gross, T. M. F. Duarte, C. Bourgogne and J. F. Nierengarten, *Chem. Commun.*, **2003**, 2412-2413.
78. P. D. W. Boyd and C. A. Reed, *Acc. Chem. Res.*, **2005**, *38*, 235-242.
79. J. F. Nierengarten, V. Gramlich, F. Cardullo and F. Diederich, *Angew. Chem. Int. Ed. Engl.*, **1996**, *35*, 2101-2103.
80. C. Bingel, *Chem. Ber.*, **1993**, *126*, 1957-1959.
81. S. Zhang, Y. Rio, F. Cardinali, C. Bourgogne, J. L. Gallani and J. F. Nierengarten, *J. Org. Chem.*, **2003**, *68*, 9787-9797.
82. Y. Rio, G. Enderlin, C. Bourgogne, J. F. Nierengarten, J. P. Gisselbrecht, M. Gross, G. Accorsi and N. Armaroli, *Inorg. Chem.*, **2003**, *42*, 8783-8793.

83. F. Cardullo, P. Seiler, L. Isaacs, J. F. Nierengarten, R. F. Haldimann, F. Diederich, T. MordasiniDenti, W. Thiel, C. Boudon, J. P. Gisselbrecht and M. Gross, *Helv. Chim. Acta*, **1997**, *80*, 343-371.
84. R. P. de Freitas, J. Iehl, B. Delavaux-Nicot and J. F. Nierengarten, *Tetrahedron*, **2008**, *64*, 11409-11419.
85. J. F. Nierengarten, S. Zhang, A. Gegout, M. Urbani, N. Armaroli, G. Marconi and Y. Rio, *J. Org. Chem.*, **2005**, *70*, 7550-7557.
86. B. J. Littler, Y. Ciringh and J. S. Lindsey, *J. Org. Chem.*, **1999**, *64*, 2864-2872.
87. J. S. Lindsey and R. W. Wagner, *J. Org. Chem.*, **1989**, *54*, 828-836.
88. M. Holler, F. Cardinali, H. Mamlouk, J. F. Nierengarten, J. P. Gisselbrecht, M. Gross, Y. Rio, F. Barigelletti and N. Armaroli, *Tetrahedron*, **2006**, *62*, 2060-2073.
89. B. Knight, N. Martin, T. Ohno, E. Orti, C. Rovira, J. Veciana, J. VidalGancedo, P. Viruela, R. Viruela and F. Wudl, *J. Am. Chem. Soc.*, **1997**, *119*, 9871-9882.
90. N. Armaroli, G. Accorsi, Y. Rio, P. Ceroni, V. Vicinelli, R. Welter, T. Gu, M. Saddik, M. Holler and J. F. Nierengarten, *New J. Chem.*, **2004**, *28*, 1627-1637.
91. J. P. Bourgeois, F. Diederich, L. Echegoyen and J. F. Nierengarten, *Helv. Chim. Acta*, **1998**, *81*, 1835-1844.
92. N. Armaroli, F. Diederich, L. Echegoyen, T. Habicher, L. Flamigni, G. Marconi and J. F. Nierengarten, *New J. Chem.*, **1999**, *23*, 77-83.
93. G. Accorsi and N. Armaroli, *J. Phys. Chem. C*, **2010**, *114*, 1385-1403.
94. M. Gutierrez-Nava, G. Accorsi, P. Masson, N. Armaroli and J. F. Nierengarten, *Chem.-Eur. J.*, **2004**, *10*, 5076-5086.
95. N. M. Dimitrijevic and P. V. Kamat, *J. Phys. Chem.*, **1992**, *96*, 4811-4814.
96. T. W. Ebbesen, K. Tanigaki and S. Kuroshima, *Chem. Phys. Lett.*, **1991**, *181*, 501-504.
97. D. K. Palit, H. N. Ghosh, H. Pal, A. V. Sapre, J. P. Mittal, R. Seshadri and C. N. R. Rao, *Chem. Phys. Lett.*, **1992**, *198*, 113-117.
98. A. N. Macpherson, P. A. Liddell, S. Lin, L. Noss, G. R. Seely, J. M. Degraziano, A. L. Moore, T. A. Moore and D. Gust, *J. Am. Chem. Soc.*, **1995**, *117*, 7202-7212.
99. D. Dubois, K. M. Kadish, S. Flanagan, R. E. Haufler, L. P. F. Chibante and L. J. Wilson, *J. Am. Chem. Soc.*, **1991**, *113*, 4364-4366.
100. M. A. Greaney and S. M. Gorun, *J. Phys. Chem.*, **1991**, *95*, 7142-7144.

Chapter 6

Experimental section

6.1 Instrumentation

6.1.1 Steady state absorption and fluorescence measurements

Absorption spectra were recorded with a Perkin-Elmer l950 UV/Vis/NIR spectrophotometer. Molar absorption values (ε) were calculated by applying the Lambert–Beer law to the absorbance spectra (A_{max} < 0.7) of the compounds. For steady-state photoluminescence measurements, the samples were placed in a fluorimetric 1-cm path cuvettes and, when necessary, purged from oxygen by bubbling with argon. Uncorrected emission spectra were obtained with an Edinburgh FLS920 spectrometer (continuous 450 W Xe lamp) equipped with Hamamatsu R928 photomultiplier tube (185–850 nm). Steady-state NIR luminescence spectra were obtained with the same spectrophotometer fitted with Hamamatsu R5509-72 supercooled photomultiplier tube (400-1700 nm) at 193 K and a TM300 emission monochromator with NIR grating blazed at 1000 nm. Corrected spectra were obtained via a calibration curve supplied with the instrument. To record the 77K luminescence spectra, the samples were put in glass tubes (2 mm diameter) and inserted in a cold finger quartz dewar, filled with liquid nitrogen. Experimental uncertainties are estimated to be ± 2 nm and ± 5 nm for absorption and emission peaks respectively.

Luminescence quantum yields of emitting solutions were determined from the corrected emission spectra, according to the approach described by Demas and Crosby[1] using either $[Ru(bipy)_3Cl_2]$ (Φ_{em} = 0.028 in air-equilibrated water solution) or Quinine sulphate (Φ_{em} = 0.546 in air-equilibrated 1 N H_2S0_4 acid water solution) as standard. The quantum yield values are indecisive up to ± 20% in solution, due to the experimental uncertainties.

Solid state absolute quantum yields were measured using $BaSO_4$ coated integrating sphere, fitted with an Edinburgh FLS920 spectrophotometer. For this measurement, potassium bromide (KBr) discs containing the respective samples were used. The uncorrected emission spectra were processed using home-made software program, according to the procedure reported by de Mello et al.[2]

6.1.2 Time resolved emission measurements

Emission lifetimes on the nanosecond time scale were determined with a IBH single photon counting spectrometer equipped with a series of nanoled (IBH) excitation sources (lex = 278, 331, 373, 465 nm). The detector was a red-sensitive (185-850 nm) Horiba Jobin Yvon (TBX-PS) photomultiplier tube. Analysis of the luminescence decay profiles against time was accomplished with the Decay Analysis Software DAS6 provided by the manufacturer.

The luminophores having lifetime in the microsecond-millisecond time scale were measured using a Perkin-Elmer LS50B spectrofluorometer equipped with a pulsed xenon lamp with variable repetition rate and elaborated with standard software fittting procedures.

6.1.3 Temperature dependant investigations

The temperature of the samples was varied with HAAKE F3-C digital heated/refrigerated water bath (HAak Mess-Technick Gmbh u. Co., Germany) which can be manually connected to cuvette holder and, externally controlled.

6.1.4 Transient absorption measurements

Transient absorption spectra in the nanosecond–microsecond time domain were obtained by using the nanosecond flash photolysis apparatus Proteus by Ultrafast Systems LLC. The excitation source was a tunable laser system made by a optical parametric oscillator (Continuum Surelite OPO PLUS) pumped by the second harmonic (532 or 355 nm) of a Continuum Surelite II Nd:YAG laser with 5 ns pulse duration at 0.1–10 mJ/pulse. Light signals were passed through a Chromex/Bruker 500IS monochromator (equipped with two gratings blazed at 600 or 1200 nm), and collected on a high-speed Silicon (DET210) or InGaAs (DET410) Thorlabs detector in the VIS (400–800 nm) and NIR (800–1700 nm) regions, respectively. The signal was then amplified by means of a variable gain wideband voltage amplifier (Femto DHPVA-200) interfaced with a Tektronix TDS 3032B digital oscilloscope connected to a PC having the acquisition software Proteus. The probe light source was a 150 W CW Xe Arc lamp Spectra Physics 69907. Triplet lifetimes were obtained by averaging 64 or 132 different decays recorded around the maximum of the absorption peak (e.g. 720 nm). The samples were placed in fluorimetric 1 cm path cuvettes and, when necessary, purged from oxygen by bubbling argon for at least 15- 20 min.

6.2 Specific Techniques

Chapter 5

Preparation of porphyrin-DWCNT conjugates solutions: Approximately 0.5 mg of **1-DWCNTs**, **1@DWCNTs** and **1-(1@DWCNTs)** were dispersed separately in 3 ml of DMF or $CHCl_3$ solvent, by mildly sonicating for 5 min. 1 ml solution from each dispersions were filtered through cotton to avoid visible floating materials, and the resulting filtrate was diluted to 2 ml with DMF or chloroform solvent. The obtained optically transparent solutions were used for the DLS and photophysical measurements.

PMMA Matrix: Approximately 1 weight% (wt%) of each DWCNTs derivative (0.5 wt% of porphyrin, to avoid concentration dependent aggregation) was dispersed in 3 ml of PMMA/$CHCl_3$ solution and sonicated for 10 min. This solution was drop-casted on clean optical glass plates and left over night to dry $CHCl_3$. The resulting transparent thin films were used for the photophysical studies.

P3HT-Py Matrix: Approximately 1 wt% of each DWCNTs derivative and porphyrin, 5 wt% of PCBM, 94 wt% of P3HT-Py (Mn: 11 K g/mol, PDI 1.2) were dissolved / dispersed in *o*-dichlorobenzene (20 mg/ml) by sonication for 90 min and left for overnight stirring. Approximately 200 ml of each solution were then spin coated (700 rpm/s, 1000 rpm, 90 sec) on clean ITO/glass surfaces. Further, the spin coated glasses are allowed to dry naturally and then used for the photophysical studies.

6.3 References

1. G. A. Crosby and J. N. Demas, *J. Phys. Chem.*, **1971**, *75*, 991-1024.
2. J. C. de Mello, H. F. Wittmann and R. H. Friend, *Adv. Mater.*, **1997**, *9*, 230-232.

List of Publications

A. Listkowski, M. Pietraszkiewicz, G. Accorsi, **J. Mohanraj,** "*Solid state photoluminescence of novel lanthanide complexes based on 4-benzoylpyrazolone Schiff base*" ***Synth. Met.***, 2010, *160*, 2377.

J. Iehl, M. Vartanian, M. Holler, J.-F. Nierengarten, B. D. -Nicot, J. –M. Strub, A. Van Dorsselaer, Y. Wu, **J. Mohanraj**, K. Yoosaf and N. Armaroli,"*Photoinduced electron transfer in a clicked fullerene–porphyrin conjugate*" ***J. Mat. Chem.***, 2011, *21*, 1562.

D. M. Lyons, **J. Mohanraj**, G. Accorsi, N. Armaroli, P. D. W. Boyd, "*A supramolecular porphyrin-ferrocene-fullerene triad*" ***New J. Chem.***, 2011, *35*, 652.

L. Maggini, H. Traboulsi, K. Yoosaf, **J. Mohanraj**, J. Wouters, O. Pietraszkiewicz, M. Pietraszkiewicz, N. Armaroli, D. Bonifazi, "*Electrostatically-driven assembly of MWCNTs with a europium(III) complex*" ***Chem. Commun.***, 2011, *47*, 1625.

L. Maggini, **J. Mohanraj**, H. Traboulsi, A. Parisini, G. Accorsi, N. Armaroli, D. Bonifazi, "*A Luminescent Host–Guest Hybrid between a Eu(III) Complex and MWCNTs*" ***Chem. Eur. J.***, 2011, *17*, 8533.

S. Shakhatreh, **J. Mohanraj**, A. Czapik, D. Tzimopoulos, S. Kotoulas, M. Gdaniec, P.D. Akrivos, "*Synthesis and structural characterization of heteroleptic Cu(I) perchlorate complexes with diimines derived from pyridinyliminobenzoic acids*" ***J. Mol. Struct.***, 2011, *1002*, 51.

A. Llanes-Palas, K. Yoosaf, H. Traboulsi, **J. Mohanraj**, T. Seldrum, J. Dumont, A. Minoia, R. Lazzaroni, N. Armaroli, D. Bonifazi, "*Modular engineering of H-bonded supramolecular polymers for reversible functionalization of carbon nanotubes*" ***J. Am. Chem. Soc***., 2011, *133*, 15412.

D. Tzimopoulos, A. Czapik, S. Kotoulas, **J. Mohanraj**, M. Gdaniec, P.D. Akrivos,"*Synthesis and structural characterization of heteroleptic Cu(I) complexes with α-diimines derived from pyridinyliminobenzoic acids*" ***J. Coord. Chem.,*** 2012, *65*, 393.

C. Aurisicchio, R. Marega, V. Corvaglia, **J. Mohanraj**, R. Delamare, D. A. Serban-Vlad, C. Kusko, C. A. Dutu, A. Minoia, G. Deshayes, O. Coulembier, S. Melinte, P. Dubois, R. Lazzaroni, N. Armaroli, D. Bonifazi, "*CNTs in Optoelectronic Devices: New structural and photophysical insights for Porphyrin-DWCNTs Hybrid Materials*" ***Adv. Funct. Mater.***, 2012, 10.1002/adfm.201102632

Selected Oral Presentations

- **J. Mohanraj**, N. Armaroli, L. Maggini, H. Traboulsi, A. Parisini, G. Accorsi, D. Bonifazi

  "*A Luminescent Host-Guest Hybrid of a Eu(III) complex and MWCNTs*"

  220th ECS and Electrochemical Energy Summit, Boston, MA (USA), OCTOBER 9-14, 2011.

- **J. Mohanraj**, K. Yoosaf, N. Armaroli, A. Llanes-Palas, H. Traboulsi, T. Seldrum, J. Dumont, A. Minoia, R. Lazzaroni, D. Bonifazi

  "*Reversible Solubilization of Carbon Nanotubes through Supramolecular Hydrogen Bonding*"

  VI International Krutyn Summer School, Krutyn (Poland) June 15-21, 2010.

Poster Presentation

- **J. Mohanraj**, K. Yoosaf, N. Armaroli, A. Llanes-Palas, H. Traboulsi, T. Seldrum, J. Dumont, A. Minoia, R. Lazzaroni, D. Bonifazi

  "*Reversible Solubilization of Carbon Nanotubes through Supramolecular Hydrogen Bonding*"

  XXIII IUPAC Symposium on Photochemistry, Ferrara (Italy) July 11-16, 2010.